ABSTRACT

Title of Thesis:	USING A BURNING RATE EMULATOR (BRE) TO EMULATE CONDENSED FUELS AND STUDY POOL FIRE BEHAVIOR IN 1G
	Eric Thomas Auth Master of Science, 2019
Thesis Directed By:	Dr. Peter Sunderland, Professor Department of Fire Protection Engineering

The Burning Rate Emulator (BRE) is a device constructed to emulate condensed fuels using gaseous fuel mixtures by matching heat of combustion, heat of gasification, smoke point, and surface temperature. The burner's heat flux gauges are calibrated for local heat flux measurements and the copper top-plate calorimeter is calibrated for measuring net heat flux to the surface, which allows for determination of an effective heat of gasification to compare to condensed fuels. Seven condensed fuels with known properties are burned and emulated using methane, ethylene, and propylene gas diluted with nitrogen. Propane gas is used to study the general pool fire characteristics displayed by gaseous flames on the BRE. Flame anchoring, flammability regions, flame height, and convective heat transfer are analyzed. Based on a radial heat flux distribution, the readings from the heat flux sensors agree with the calorimeter when applied to a flame. Example flame images are shown.

USING A BURNING RATE EMULATOR (BRE) TO EMULATE CONDENSED FUELS AND STUDY POOL FIRE BEHAVIOR IN 1G

by

Eric Thomas Auth

Thesis submitted to the Faculty of the Graduate School of the
University of Maryland, College Park, in partial fulfillment
of the requirements for the degree of
Master of Science
2019

Advisory Committee:
Peter Sunderland, Professor, Chair/Advisor
James Quintiere, Professor Emeritus
Arnaud Trouve, Professor

Acknowledgements

First and foremost, I would like to thank my advisors for providing input and guidance on a weekly, and often more frequent, basis. I cannot imagine a more knowledgeable and dedicated group of experts in the field of fire science than Dr.'s Peter Sunderland, Jim Quintiere, John de Ris, and Howard Baum. I am honored to have been able to learn from them over the past year. Their ideas were influential and provided a means to achieve the completion of this work. I hope that I can take with me some of their enthusiastic attitudes and desire to continually improve no matter the circumstances.

Secondly, I would like to extend my gratitude to all student members of the BRE team, past and present. To Parham and Chuanbo, for providing thoughtful discussions and assistance in the lab whenever asked. To Akshit, for teaching me how to use the burner's measurement devices which allowed me to kickstart my research. And to all the BRE students before me who contributed to the development of the devices and procedures through which I conducted my research, I thank you.

Next, I would like to thank all FPE students, faculty, and staff whom I had the pleasure of interacting with over the past year. Particularly I am grateful for the students in Dr. Sunderland's group who were always willing to share their lab space and experience, Fernando for always being available to provide advice in the lab, and Dr. Stas' students for answering many of my questions. I would also like to give special thanks to Dr. Trouve for serving on my thesis committee.

Finally, I would like to acknowledge all friends and family who showed countless support over the last year. To my roommates and friends, for ensuring that

one of the busiest years of my life was also one of the most fun. To my parents, who I could never properly thank for all they have provided me. They have never ceased to contribute invaluable love, support and direction. To my siblings, for also supporting me, providing entertainment, and taking my mind off work. Lastly, to Connie for always making time for me and inspiring me to work as hard as you do.

Table of Contents

List of Tables

List of Figures

List of Symbols

Symbols

A	surface area
B	Spalding B number
C	calibration constant for heat flux sensor
c_p	specific heat
c_g	specific heat of gas
D	burner diameter
D_0	flame diffusion coefficient
e	thermal effusivity of semi-infinite burner back
E	heat flux gauge voltage
g	gravitational constant
h	convective heat transfer coefficient
Δh_c	heat of combustion
k	thermal conductivity
L	heat of gasification
L_{SP}	smoke point
$\dot{m}$	mass loss rate
$\dot{m}$"	mass flux
$(mc)Cu$	heat capacity of copper top plate (slug) calorimeter
MW	molecular weight
Nu	Nusselt number
p	pressure

Pr	Prandtl number
$\dot{q}''$	heat flux
$\dot{Q}$	energy release rate
Q	volumetric flow rate
Q^*	Froude number based on energy release rate
r	stoichiometric oxygen to fuel ratio
R	radial position on burner surface
R^*	location of burner "offset" sensor
Ra	Rayleigh number
S	ratio of volume of air to volume of fuel gas for complete combustion
t	time
T	temperature
ΔT	temperature difference
x	length dimension
X	mole (volume) fraction
Y	mass fraction
z_f	flame height

Greek Symbols

α	absorptivity, thermal diffusivity
β	thermal expansion coefficient
δ	material thickness, flame standoff distance
λ	dimensionless mass loss rate
ν	kinematic viscosity

ϵ	emissivity
ρ	density
σ	Stefan-Boltzmann constant

Subscripts

abs	absorbed
avg	average
b	semi-infinite back of burner
c	center, convective
cal	calorimeter
conv	convective
Cu	copper calorimeter surface (without holes)
Cu + holes	copper calorimeter surface (with holes)
e	effective, external
eff	effective
f	fuel, flame
fl	flame
g	gaseous fuel
h	holes
i	incident
int	integral
L	length dimension
mix	gaseous mixture
NA	non-anchored flame

N_2	nitrogen
o	offset, semi-infinite back of burner
O_2	oxygen
r	respective
rad	radiation
rod	heat sensor rod
rr	re-radiation
s	surface
sens	sensor
std	standard
sur	surface
tot	total
∞	ambient

Chapter 1: Introduction

1.1 Motivation

As technology continues to evolve, space exploration becomes increasingly feasible. As expected, safety is of the utmost concern when it comes to sending satellites, vehicles, and especially human beings into space. Roughly twenty years ago (February 1997), a fire occurred on the Russian spacecraft Mir [1]. This incident brought the issue of fire safety in microgravity to the forefront [2]. Many of the phenomena related to fire on earth are either not present or altered in microgravity. One important difference is buoyancy, which drives natural convection in flames on earth but has a much-reduced effect in microgravity [2]. Accordingly, compared to earth fires, relatively little is known about microgravity combustion/burning.

NASA has funded fire research since the 1980's [2] and is currently sponsoring five Advanced Combustion via Microgravity Experiments (ACME) programs to study combustion technology [3]. Of these, the Burning Rate Emulator (BRE) project is focused on fire safety, while the others are focused on combustion efficiency. NASA uses a pass-fail flame spread test (Test 1) in normal gravity conditions to determine the flammability of materials [4]. It is indicated that this is likely insufficient for microgravity purposes [5]. The BRE burner was created to emulate condensed fuels by matching certain fuel properties (heat of combustion, smoke point, heat of gasification, and surface temperature). The BRE project aims to study the flammability of condensed fuel flames in microgravity via emulation.

1.2 Literature Review

1.2.1 Emulation

Initial studies using gaseous fuels to emulate pool fires were performed in the 1960's by Corlett [6], [7], [8]. De Ris et al. performed both related and separate research on emulation in the 70's [9], [10]. These studies proved that condensed fuel burning could be simulated by gas and laid the foundation for the current research. One focus of the research by de Ris was heat of gasification, which is a key part of both current emulation theory and the research performed during this study. Another essential element of the BRE is the ability to use a porous copper plate as a calorimeter.

1.2.2 Calorimetry

Evaluating the heat of gasification requires a determination of the heat flux at the burning surface. The two favored methods for determining heat flux are heat flux gauges and energy balance methods, also known as calorimetry [11]. Slug calorimeters measure heat transfer by assuming one-dimensional conduction to a cylindrical "slug" which has known thermal properties [12]. Due to radial variation of heat flux from a flame on the burning surface, a slug calorimeter is better suited to determine average heat flux than gauges, which are better for local heat flux measurements [11]. Both heat flux gauges and a calorimeter are present on the BRE burner, however this study focuses on the development and application of the calorimeter for the BRE.

1.2.3 BRE Development and History

Previous studies relating to the BRE have been conducted at the University of Maryland (UMD). The instruments, procedures, and findings from these studies were crucial for setting the stage for the current research. Bustamante initially studied angular effects on methanol/methane emulation [13].

There have been three series of BRE burners designed to measure relevant heat flux data from gaseous flames. The first series, denoted BRE 1, was developed by Bustamante [13]. BRE 1 had a perforated brass surface and relied solely on heat flux sensors at the burner surface for measurement. The 50 mm BRE 1 burner was used to successfully emulate four condensed fuels in 2014, which can be seen in Figure 1-1 [14], [15].

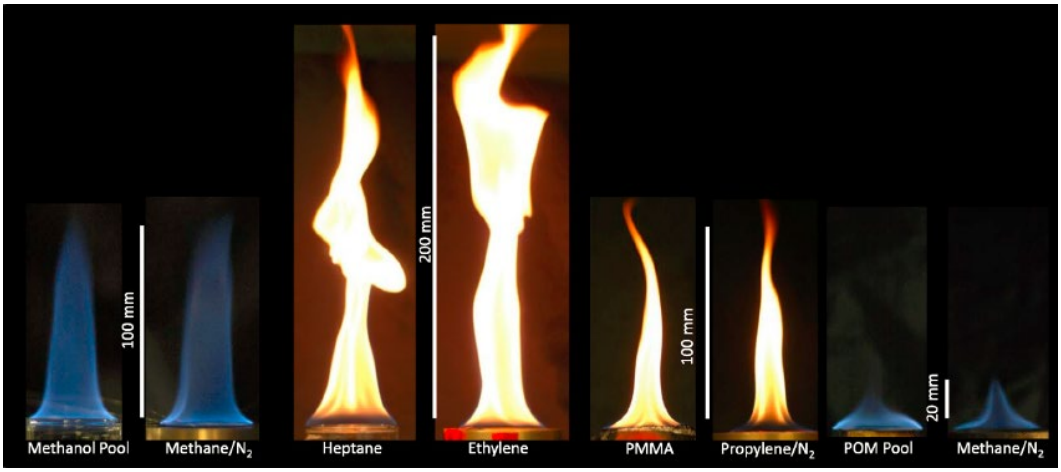

Figure 1-1. Previous emulation using the 50 mm BRE 1 [14].

The second series, BRE 2, introduced a copper burner surface with embedded thermocouples. Kim designed the BRE 2 and measured thermal degradation of high absorptivity paints for application to the surface [16]. A schematic is provided in Figure 1-2. The copper surface allowed for a calorimetry analysis to be applied, leading to a more thorough determination of the net heat flux to the surface [11]. Both BRE 2 burners were used in a set of drop tower tests performed at NASA Glenn's Zero Gravity

Research Facility in 2016 [17]. A combination of the BRE 1 and BRE 2 burners was also used to study ignition and extinction using different fuel gases [18], [19].

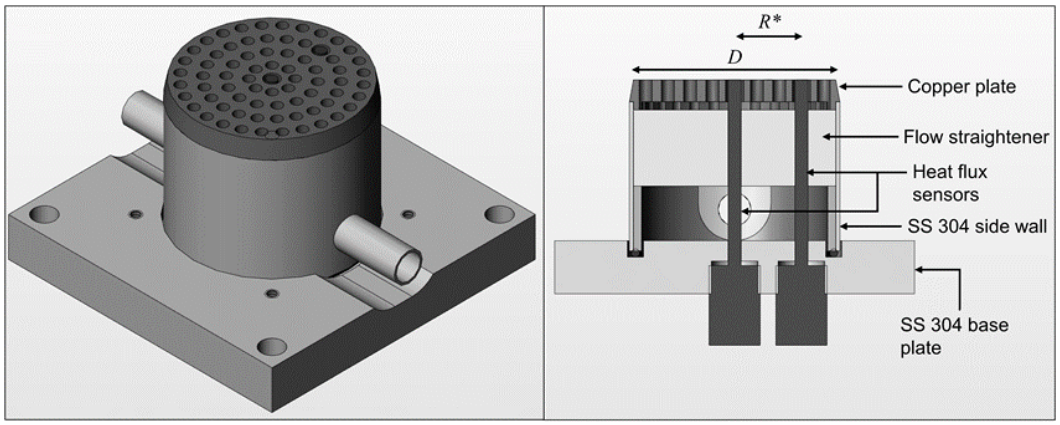

Figure 1-2. BRE 2 burner schematic [17].

The BRE 3 burners have a similar design to the BRE 2, and as of February 2019 have begun testing on board the International Space Station (ISS) to study microgravity flames. A second round of testing is set to begin in the fall of 2019. An image of an ethylene flame on the 25 mm BRE 3 burner on the ISS is shown in Figure 1-3. The 25 mm BRE 2 burner was used for the following research. The BRE 2 burners each have two embedded Medtherm Schmidt-Boelter heat flux sensors that are used to measure heat flux to the burner surface. Each heat flux sensor also includes a thermocouple for temperature measurement. The BRE burners have two separate thermocouples used to measure the temperature of the copper plate that serves as the burner surface. One of each heat flux sensor/thermocouple is located at the center of the burner surface (R = 0), and the other is nearer to the edge ($R = R^*$). These sensors are typically denoted center and offset, respectively. For the 25 mm BRE 2 burner, R^* = 8.25 mm.

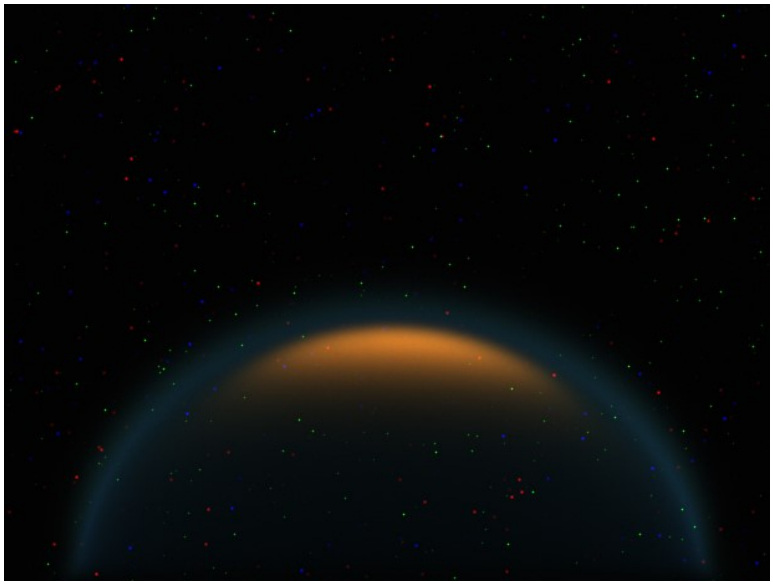

Figure 1-3. Ethylene flame in microgravity.

1.3 Preview of Research

This work serves to improve the science of condensed fuel emulation with two different studies performed in 1g. Chapter 2 contains the preparation of the burner for flame. This includes surface repainting, heat flux gauge calibration, and copper calorimeter calibration. Improvements were made to the calorimeter calibration process and the evaluation of the obtained calibration parameters. Chapter 3 presents the first study, which focuses on emulation of specific condensed fuels, similar to the research using the BRE 1 that is presented in Figure 1-1. This includes the setup for burning condensed fuels as well as gas through the burner. It also explains the determination of gas mixture emulation properties such as heat of gasification and flame height. This study further proves the ability to emulate condensed fuels by expanding the collection of condensed fuels that have been successfully emulated. Chapter 4 presents the second study, which examines a series of tests with propane/nitrogen mixtures. These tests

show a region of flammability consistent with pool fires. The results of these tests were analyzed for flame base area, flame height, radial heat flux distribution, and convective heat flux. They were also used to construct flammability diagrams. Where possible, results such as flame height were compared to experimental data and theory from the literature. Chapter 5 ties the findings together through a set of conclusions and recommendations for future research.

Chapter 2: Burning Rate Emulator Calibration

2.1 Surface Preparation

After previous usage the surface of the BRE 2 burners had become insufficient for obtaining accurate data. Some areas of the surface had missing paint, as well as others with soot buildup from flame experiments. The calorimeter analysis relies on uniform paint across the surface of the burner, and therefore it was desirable to repaint the BRE 2 burners. The following procedure was performed for both the 25 mm and 50 mm BRE 2 burners. The next paragraph details the process of removing existing paint from the burner and heat sensor surfaces.

The first step was to remove the heat flux gauges from the burner. This can be done easily as the sensors are screwed into the threaded bottom of the stainless-steel plate that serves as the base of the burners. Acetone solution was used to remove the previous coat of paint from the heat flux gauges, with before and after images shown

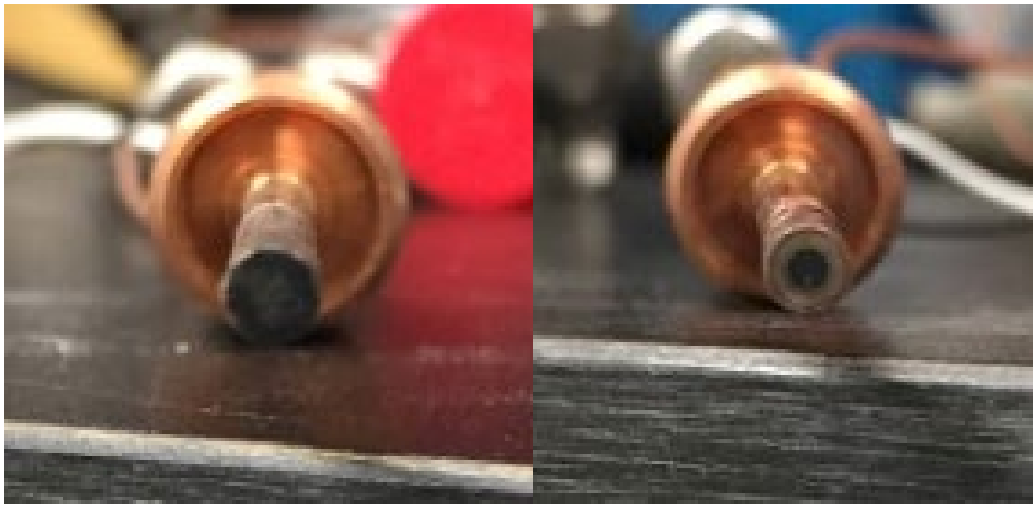

Figure 2-1. Heat flux gauges for the 50 mm BRE 2 burner with previous coat of paint (left) and after removing paint with acetone solution (right).

in Figure 2-1. A squeeze bottle was used to apply Acetone to a clean rag which was used to carefully wipe the existing coat off the heat flux gauge surface. For the 50 mm burner only, thermocouples and the tape holding them in place were removed from the top of the burner, visible in Figure 2-2. For the 25 mm burner, the thermocouples are set in place on the underside of the copper plate, and therefore did not need to be removed for the painting process. Very fine sandpaper (800+ grit) was then used to carefully remove the paint from the copper surface. Sanding was performed with the burner surface facing the ground, so that detached paint or sandpaper would not fall into the burner. The next paragraph describes the steps taken to ensure a uniform paint finish on the burner surface.

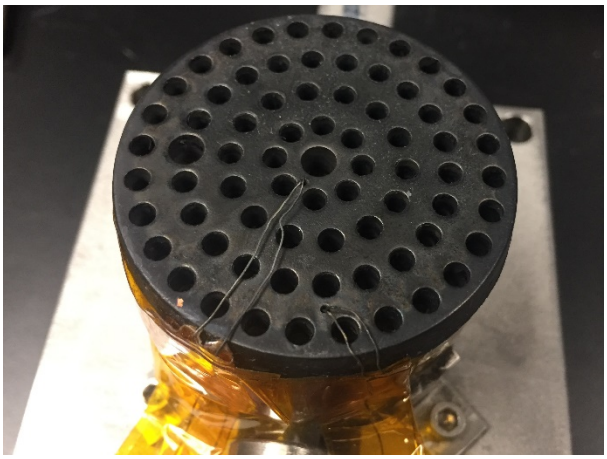

Figure 2-2. 50 mm BRE 2 burner with thermocouples.

Prior to painting, the base of the burner was fully covered to ensure paint was applied only to the burner surface. Tape was used to cover the interface between the lower edge of the copper plate and the back of the burner. A paper covering attached to the tape was used to entirely cover the rest of the burner. Paper rolls were wrapped around short wire fragments to match the thickness of the heat sensor holes, and then

inserted into the holes to prevent paint from entering these holes. The 25 mm BRE 2 burner is shown in Figure 2-3 just before being painted.

Figure 2-3. 25 mm BRE 2 burner prepared for new coat of paint.

The burners were painted with one coat of Rustoleum High Heat Primer and two coats of Rustoleum High Heat Paint, allowing 30 minutes in between for each coat to dry. Before the last coat of paint, the heat flux gauges were reinserted, to produce a thin layer of paint on the heat flux gauge surface. Paint was applied from the can at a 45% angle to the burner surface (to prevent paint from traveling into the burner), about 25 cm from the surface vertically, with a slow sweeping motion. After allowing the paint to dry for 24 hours, a radiant propane heater was used to heat treat the paint. The paint was treated for 30 minutes at 120 °C (248 °F), and the process repeated three times, allowing 30 minutes for the paint to cool in between. Temperatures were monitored using the heat sensor and burner thermocouples. The 120 °C temperature was chosen to follow NASA's recommendation that the sensors do not exceed 316 °C

(600 °F) [3]. Figure 2-4 and Figure 2-5 show the heat-treating process and the 25-mm burner after painting and heat-treating, respectively.

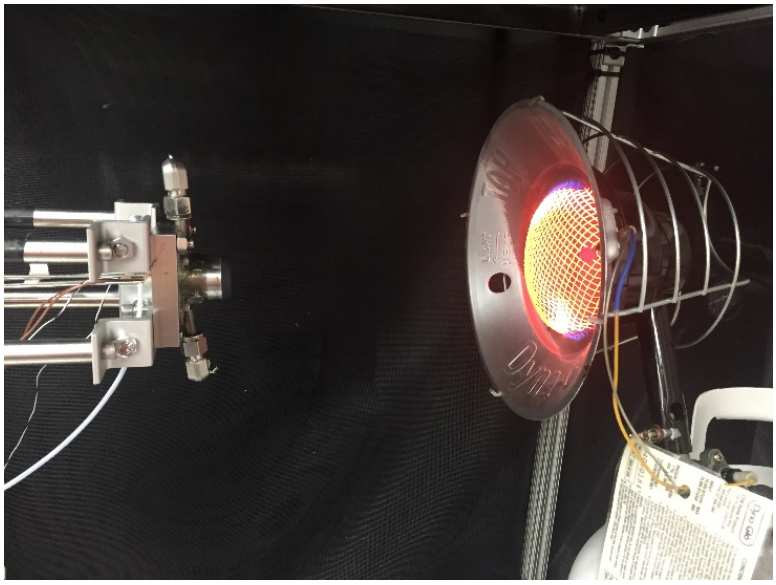

Figure 2-4. 25 mm BRE 2 heat-treating with radiant heater.

Uniformly painting the burner and sensors with the same paint ensures that these surfaces have the same absorptivity (α) and emissivity (ϵ). Rustoleum High Heat Paint has an absorptivity of 0.91 and an emissivity of 1 and was shown to be more

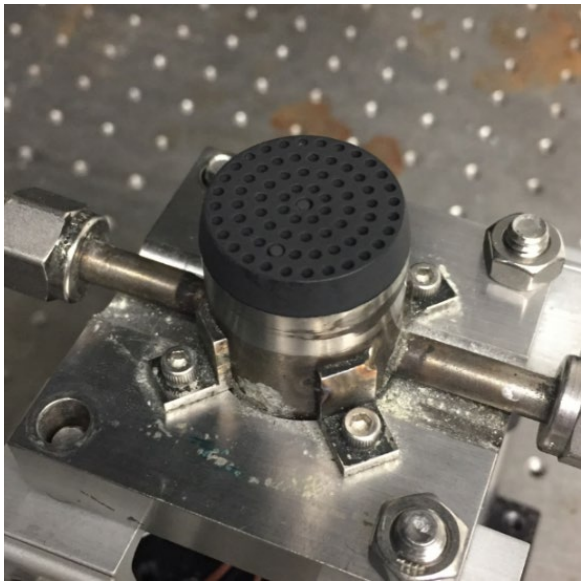

Figure 2-5. 25 mm BRE 2 burner with new paint job.

thermally durable than other high emissivity paints [16]. Having uniformity of these surface properties simplifies the heat transfer between the sensor and burner surfaces, which is helpful for accurate calibration of the heat flux gauges and calorimeter [14].

2.2 Heat Flux Gauge Calibration

To obtain meaningful heat flux values from the recorded voltages, each sensor was first calibrated against the Medtherm SN 180254 transfer standard (traceable to NIST). This heat sensor is painted with Nextel Suede paint, which has an absorptivity of α = 0.98 [16]. Additional equipment used for the calibration consists of a radiant propane heater, a water reservoir and pump, and two DATAQ data acquisition systems. The calibrated transfer-standard heat sensor is water cooled using the pump and water reservoir to moderate surface temperature. The burner-embedded heat sensors are not water-cooled for consistency with drop tower and spaceflight experiments, where water-cooling is not an option.

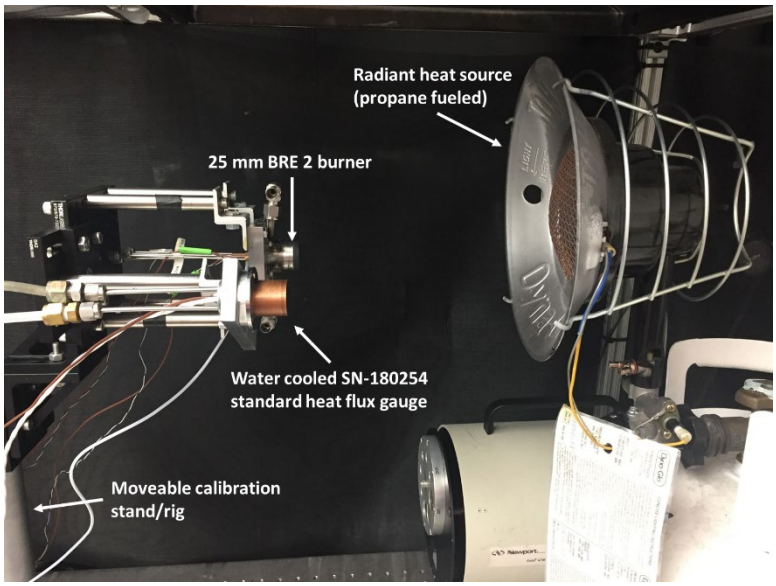

Figure 2-6. Burner heat flux gauge calibration setup.

For this calibration, the BRE and the transfer standard are placed side by side, each facing the radiant propane heater. The heater, burner, and standard are all aligned to the same vertical position, and the burner and standard are separated horizontally by about 15 cm. An image of the setup can be viewed in Figure 2-6.

During calibration, the rig is moved horizontally so that each heat flux meter (burner center, burner edge, and standard) is directly in line with the center of the radiant heat source and is held in this position for 30-60 seconds. A drawing of the three positions is included in Figure 2-7. This process is performed four times, moving the calibration rig closer to the heat source in between each step to increase the heat flux to the sensors. In between these increases in heat flux, the radiant heater is blocked by an insulating panel. This helps to identify each "step" in the calibration when analyzing the data.

Ambient temperature measurements are made using a separate thermocouple through a DATAQ D245 data acquisition system. All other measurements are recorded through a DATAQ D2008 data acquisition system. This includes standard and burner heat flux and sensor temperature as well as copper surface thermocouples. All heat flux sensors involved are Schmidt-Boelter type gauges. For BRE 2 burners, heat sensor

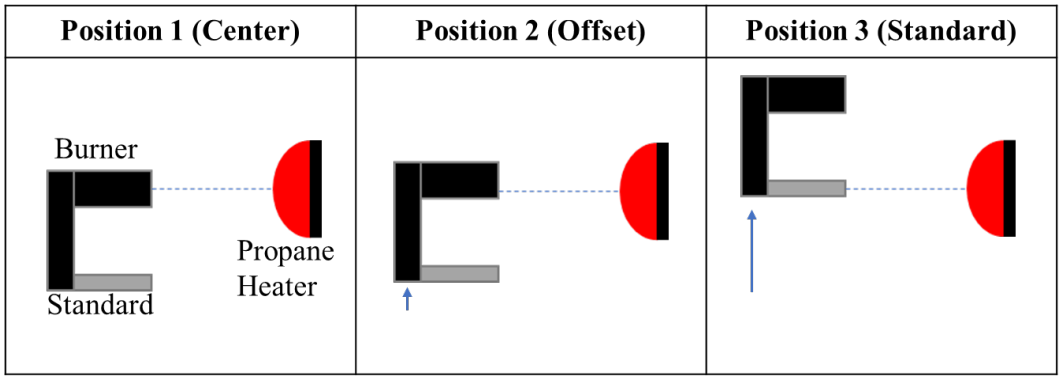

Figure 2-7. Diagram of calibration sensor positions. Arrows signify rig movement

temperatures are measured using type T thermocouples, and copper temperature is measured using type K thermocouples. For BRE 3 burners, all thermocouples for temperature measurement are type K. The SN 180254 transfer standard uses a type T thermocouple. Data measurements are made at a frequency of 2 Hz.

For this calibration, a subscript of 1 refers to the standard sensor, and 2 refers to the sensor being calibrated. The goal of this calibration is to find C_2 calibration constants for the embedded sensors that are used to convert voltage outputs from each sensor into meaningful heat flux data. By measuring the heat flux with the transfer standard, for which C_1 is already known, C_2 can be obtained for each embedded sensor. The absorbed heat flux is given as

$$\dot{q}"_{abs} = \alpha\dot{q}"_i - \epsilon\sigma\left({T_S}^4 - {T_\infty}^4\right) - h(T_S - T_\infty) = CE \tag{2.1}$$

where $\alpha\dot{q}"_i$ represents the absorbed portion of the incident heat flux, the second two terms account for re-radiative and convective losses, C is the sensor calibration constant and E is the received voltage in mV. The heat transfer coefficient h is estimated by using a Nusselt number correlation for natural convection on a vertical plate [20].

$$h = Nu(k/D) \tag{2.2}$$

$$Nu = 0.68 + \frac{0.670{Ra_L}^{\frac{1}{4}}}{\left[1 + \ (0.492/Pr)^{\frac{9}{16}}\right]^{\frac{4}{9}}} \tag{2.3}$$

An expression for the incident heat flux to the standard heat flux gauge can be found by rearranging Equation 2.1.

$$\dot{q}''_{i,1} = \frac{\left[C_1E_1 + \epsilon_1\sigma\left(T_{s,1}^4 - T_\infty^4\right) + h_1\left(T_{s,1} - T_\infty\right)\right]}{\alpha_1} \tag{2.4}$$

The incident heat flux produced by the radiant heat source is the same to each sensor (when each is centered), and absorptivity (α) is known for each sensor, so absorbed heat flux values for the embedded sensors can be found.

$$\dot{q}''_{i,2} = \dot{q}''_{i,1} \tag{2.5}$$

$$\dot{q}''_{abs,2} = \alpha_2 \dot{q}''_{i,2} - \epsilon_2 \sigma\left(T_{s,2}^4 - T_\infty^4\right) - h_2\left(T_{s,2} - T_{Cu}\right) = C_2 E_2 \tag{2.6}$$

Since the embedded sensors are surrounded by the copper surface, convective heat is lost to the surface rather than the surroundings. Substituting the incident heat flux from the standard gauge into Equation 2.4, an absorbed heat flux to each embedded sensor is calculated. These values are then compared to the voltage outputs at each "step" to obtain a calibration constant for each sensor. This is achieved by plotting absorbed heat flux vs. voltage at each step and calculating the slope of the line (which equals C_2). Heat sensor calibration plots are provided in Figure 2-8.

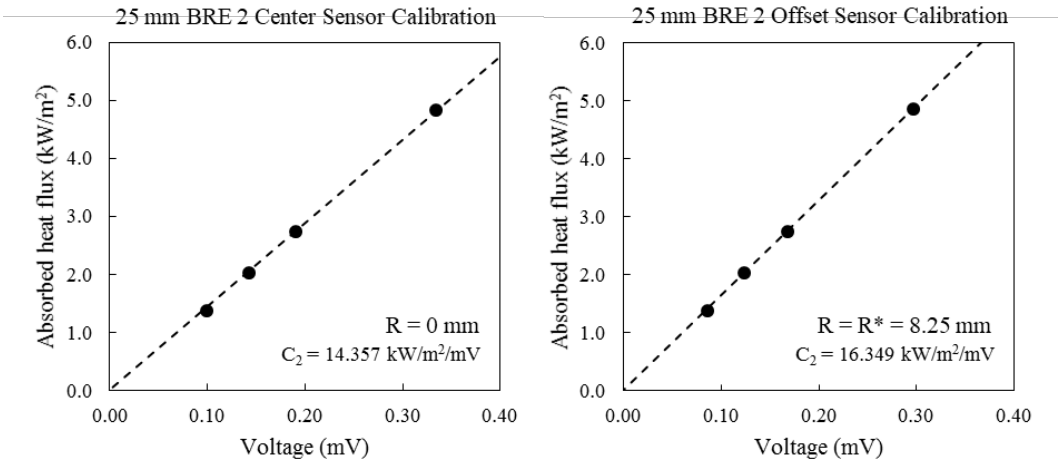

Figure 2-8. Calibration charts for 25 mm BRE 2 sensors.

Calibration constants for BRE 2 sensors are reported and compared to the initial calibrations performed by Medtherm in Table 2-1. UMD constants are within 5% of Medtherm constants. Full calibration charts are provided in Appendix A.

Table 2-1. Calibration constants for 25 mm BRE 2 sensors.

Burner	Sensor	Radial Position (mm)	UMD Calibration Constant ($kW/m^2/mV$)	Medtherm Calibration Constant ($kW/m^2/mV$)
BRE 2 (25 mm)	Center	R=0	14.36	14.77
	Offset	R=R*=8.25	16.35	17.09

2.3 Copper Calorimeter Calibration

As previously mentioned, the burner surface can be used as a calorimeter for better determination of net heat flux across the surface. In order to achieve this, the calorimeter must be calibrated as well. During this process, the previously calibrated embedded heat sensors are used as a reference to calibrate the copper calorimeter. Additional equipment used for the calibration consists of a propane heater, a radiation shield, and a DATAQ data acquisition system.

Figure 2-9. DATAQ DI-2008 data acquisition system.

2.3.1 Calorimeter Calibration Apparatus

For this calibration, the burner is again oriented horizontally, facing the radiant propane heater. A flat radiation shield made of low-density material and covered with aluminum foil is placed just behind the copper plate. The radiation shield is shown on the burner in Figure 2-10. This prevents the back of the burner from being directly heated by the propane heater, which is important to preserve the validity of the calorimeter analysis. The heater and burner are aligned to the same vertical position, and the burner is positioned so that the center of the burner and the center of the heater are aligned (Position 1 in Figure 2-7). Like the heat sensor calibration, the heat flux is varied in steps in order to determine calibration constants. During calibration, the burner is moved closer to the heater twice, and then moved back to the original position in two steps. The burner is held at each location for approximately 90 seconds and moved quickly in between steps to create "jumps" in the heat flux received at the surface. Raw data is exported to an excel file for analysis, where it is processed and inserted into the calorimeter model.

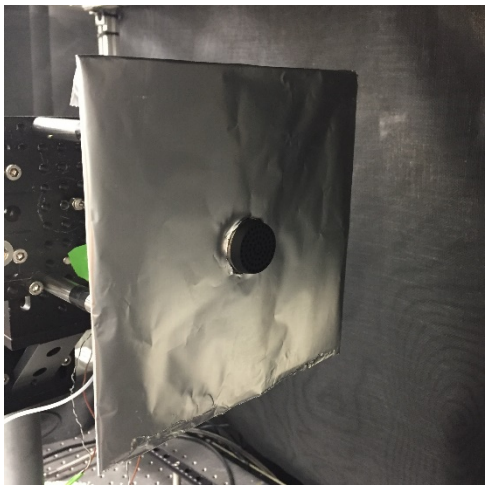

Figure 2-10. Radiation shield for 25 mm burner.

2.3.2 Calorimeter Model

A model was developed to determine the heat loss from the copper plate [11]. The model allows for the calculation of the heat flux absorbed by the copper surface based on its temperature [11].

$$\dot{q}"_{abs}A_{Cu+holes} = \alpha\dot{q}"_{i}A_{Cu+holes} = (mc)_{Cu}\frac{dT}{dt} + \varepsilon\sigma A_{Cu+holes}\left(T^4 - T_\infty{}^4\right) + hA_{Cu}(T - T_\infty) + \dot{Q}_g + \dot{Q}_{rod} + \dot{Q}_b \quad (2.7)$$

This model considers the effect of six terms, which are numbered in the order they appear. These are the change in internal energy of the copper plate (term 1), re-radiative and convective loss to the surroundings (terms 2 and 3), heat loss to gas flowing through the burner (term 4), heat loss to the embedded sensor rods (term 5), and heat loss to the back of the burner (term 6). Markan [11] presented a visual representation of the heat transfer involved with the calorimeter, which can be seen in Figure 2-11.

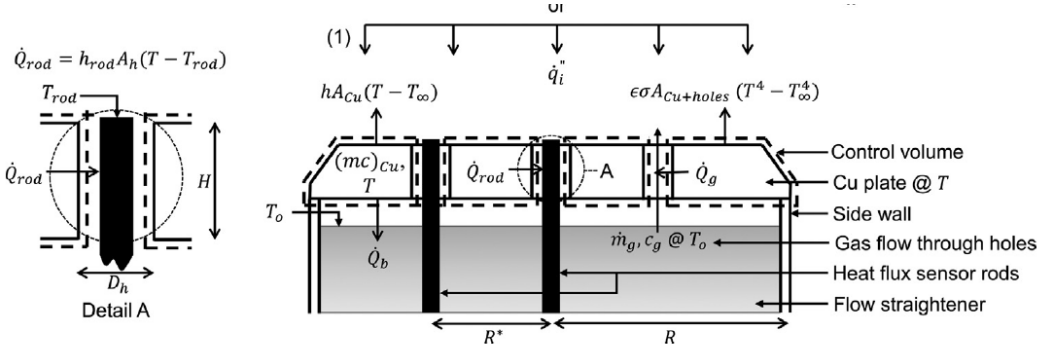

Figure 2-11. Calorimeter energy balance [11].

The calibration is performed by comparing the average absorbed heat flux from the sensors ($\dot{q}"_{abs} = \alpha\dot{q}"_{i}$) to the calorimeter heat flux ($A_{Cu+holes} \times RHS$) using Equation 2.7. Absorbed heat flux to each sensor is calculated by using the equations from 2.2. The common variable between all terms is the copper slug temperature, T,

which is assumed uniform and is taken as the average from the two embedded thermocouples. Full definitions for terms 4-6 are given by

$$\dot{Q}_g = \dot{m}_g c_g (T - T_O) \tag{2.8}$$

$$\dot{Q}_{rod} = h_{rod} A_h (T - T_{rod}) \tag{2.9}$$

$$\dot{Q}_b = h_O A_{Cu+holes} (T - T_O) \tag{2.10}$$

Certain terms are more complicated than others, and therefore deserve a more thorough explanation. A short explanation for the simpler terms follows. For example, term 2 can directly be calculated from the burner output and term 3 can be determined by assuming a heat transfer coefficient for natural convection on a vertical plate (Equations 2 & 3). For calibration, no gas is flowed through the burner and term 4 ($\dot{Q}_g$) is equal to zero. Term 5 ($\dot{Q}_{rod}$) has a minimal effect on the overall heat transfer due to the small area ratio of $A_h/A_{Cu+holes}$ and the fact that the sensor and copper temperatures are very similar throughout the calibration. This leaves terms 1 and term 6, which dominate the calorimetry of the copper plate.

Term 1 is the change in internal energy of the copper calorimeter. This is the energy change that the copper feels directly from the heat source, whereas the rest is lost through the other terms in the energy balance. It makes sense that this is one of the dominating terms because it is the basis of the calorimetry analysis. To determine $\frac{dT}{dt}$, an Excel tool called LINEST is used. This determines the best fit slope of the copper temperature-time curve using the surrounding 19 points (9 seconds) for each time step. The determination of $(mc)_{Cu}$ is a result of the calibration, which is explained later.

Term 6 ($\dot{Q}_b$) is the heat loss to the back of the burner. While simple in principle, there are unknowns that make the determination of this term quite complicated. For the

full procedure, the reader is directed to the original BRE calorimeter paper by Markan *et al.* [11]. In the analysis, the back of the burner is assumed to be semi-infinite. The source expresses the temperature of the semi-infinite back (T_O) with an integral solution [11].

$$T_O = T_\infty + \frac{h_O}{e_b}\left[1.5(T - T_O)\int (T - T_O)dt\right]^{\frac{1}{2}} \quad (2.11)$$

This includes both unknowns of the equation, h_O, the heat transfer coefficient to the back of the burner, and e_b, the thermal effusivity of the back of the burner. Like $(mc)_{Cu}$, these unknowns are burner-specific and must be determined through calibration. Equation 2.11 is solved in excel via a time-stepping method that increments T_O every time step based on the temperature rise of the copper.

Three separate areas are needed to solve Equation 2.7 and calculate the calorimeter heat flux. These are $A_{Cu+holes}$, the area of the copper surface including holes, A_{Cu}, the area of the copper surface minus holes, and A_h, the cylindrical surface area of the holes around the heat sensors. These were determined for each of the BRE 2 and 3 burners and are presented in Table 2-2.

Table 2-2. Areas used for calorimeter model.

Burner	**Diameter**	**$A_{Cu+holes}$**	**A_{Cu}**	**A_h**
	mm	mm^2	mm^2	mm^2
BRE 2	25	491	340	38
BRE 2	50	1963	1360	76
BRE 3	25	491	345	33
BRE 3	50	1963	1310	68

2.3.3 Calibration Evaluation

The goal of the calibration is to determine burner-specific parameters. These are the heat transfer coefficient to the sensor rods (h_{rod}), the heat transfer coefficient to the back of the burner (h_o), and the thermal effusivity of the back of the burner (e_b) [11]. However, a fourth parameter, $(mc)_{Cu}$, was added to the optimization to improve the calibration. While this parameter can be estimated through calculation (~ 7.0 J/K for the 25 mm BRE 2), this value is not perfectly accurate. This may be due to the assumed density of the copper or the addition of a paint layer. The addition of this parameter greatly improved the calorimeter calibration.

The heat transfer coefficient to the sensors, h_{rod}, has very minimal effect on the calibration. This is because of the small value of the area over which the heat transfer from the calorimeter to the sensor rods takes place. Knowing this, an estimated value for h_{rod} was calculated (22 W/m^{2}K) and used for calibration. The full calculation is shown in Appendix A. The other three parameters are determined by entering an initial guess and then performing an optimization method. This is done by minimizing the mean-squared error (*MSE*) between the absorbed heat flux given by the calorimeter model and the average of the two heat sensors.

$$MSE = \sum_{i}^{n} \left(q''_{cal,i} - q''_{sens,i} \right)^2 \tag{2.12}$$

Excel's Solver data analysis tool was used to optimize these parameters in order to achieve the lowest *MSE* for each calibration. A transient plot of a completed calibration presented in Figure 2-12. Matching a step function thoroughly tests the calorimeter and the results prove that the calorimeter is an appropriate tool to measure heat flux. The black line is the average of the two heat sensors, and the blue line is the

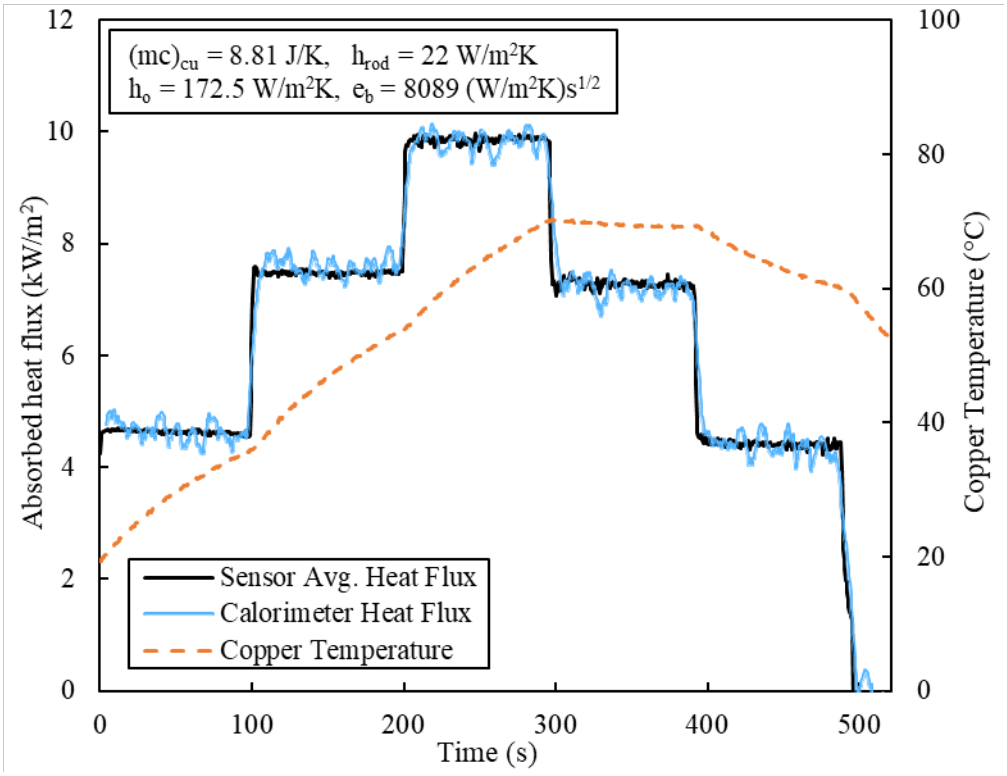

Figure 2-12. Calibration 1 using optimized parameters.

calorimeter heat flux. Four calibrations were performed, with each applying a different combination of heat fluxes from the radiant heater varying from approximately 4-13 kW/m^2. Results of each calibration yielded the burner-specific parameters shown in Table 2-3.

Table 2-3. Calibration parameters for 25 mm BRE 2 calibrations.

BRE2 25 mm	$(mc)_{cu}$ (J/K)	h_{rod} (W/m^{2}K)	h_o (W/m^{2}K)	e_b (W/m^{2}K)s$^{1/2}$	MSE (kW^2/m^4)
Calibration 1	8.81	22	172.5	8089	0.067
Calibration 2	8.90	22	172.8	7316	0.120
Calibration 3	9.15	22	155.2	10102	0.120
Calibration 4	8.92	22	165.8	7273	0.078
Average	*8.95*	*22*	*166.6*	*8195*	*0.096*

These parameters were then averaged (last row of Table 2-3) and reinserted into each calibration. Final plots of each calibration using average burner parameters are shown in Appendix A. The updated *MSE*'s using average parameters are shown in Table 2-4. An evaluation of the calibration is performed by determining the normalized root-mean-square deviation (*NRMSD*), which is also reported in Table 2-4.

$$NRMSD = \frac{RMSE}{\overline{q}''} = \frac{\sqrt{MSE}}{\overline{q}''} \tag{2.13}$$

The root mean-squared error (*RMSE*) gives a sense of how closely the calibration matches up on average to the sensor values (in kW/m^2). The *NRMSD* does the same as a percentage value normalized by the average heat flux from the entire calibration.

Table 2-4. Calibration error evaluation using average parameters.

BRE2 25 mm	**MSE** (kW^2/m^4)	**RMSE** (kW/m^2)	**NRMSD** (%)
Calibration 1	0.076	0.276	4.42
Calibration 2	0.122	0.350	5.36
Calibration 3	0.122	0.349	4.45
Calibration 4	0.106	0.325	5.31
Average	*0.107*	*0.325*	*4.89*

Using the average heat flux value during each calibration to normalize this deviation, the calorimeter was within 5% of the values determined by the heat flux gauges. At this point, both the heat flux sensors and calorimeter have been properly calibrated and the BRE is ready to be used to measure heat flux from a flame.

Chapter 3: Emulation of Condensed Fuels

3.1 Description of Experiments

The first study performed was focused on emulating the properties of a set of specific condensed fuels. This study is similar to the one performed by Zhang *et al.* about five years ago [14]. Previously, the net heat flux was taken by determining an average value over the surface from the local sensors. However, the burner now contains a calorimeter that is much better suited for determining the net heat flux to the burner surface. In turn, this leads to more accurate heat of gasification values that should result in better emulation. The study aims to emulate a slightly larger range of fuels than the original study. First, condensed fuels are burned in a 25 mm dish to measure mass loss rate. A gaseous fuel mixture with the same heat of combustion is then burned at the same rate to perform emulation. The methods and results are presented in the remainder of the chapter.

3.2 Gaseous Fuel Mixtures for Emulation

Condensed fuels can be emulated with a gaseous fuel mixture by matching their heat of combustion, heat of gasification, surface temperature, and smoke point [14]. Matching the surface temperature perfectly was found to be unnecessary due to its low impact on the heat transfer when compared to the flame heat flux [14]. The following experiments focused on the other three parameters. Flame characteristics, such as flame height and color, are also used to judge the accuracy of an emulation. Changing heat of combustion is performed by diluting a pure gaseous fuel with different amounts of

nitrogen. Different fuels can also be emulated by controlling the mass flow of the gas mixture, which affects the heat of gasification.

3.2.1 Fuel Mixture Properties

The following equations determine the necessary properties for properly analyzing different fuel mixtures. An expression for the molecular weight of the mixture is given as

$$MW_{mix} = X_f MW_f + X_{N2} MW_{N2} \tag{3.1}$$

where X_f and X_{N2} are the molar fractions of fuel and nitrogen, and MW_f and MW_{N2} are the molecular weights of fuel and nitrogen. A density can be determined for the mixture at standard temperature and pressure (STP) based on the molecular weight of the mixture.

$$\rho_{mix} = \frac{p_{std} MW_{mix}}{R T_{std}} \tag{3.2}$$

Standard pressure and temperature are 101325 Pa and 298 K, in accordance with the Alicat flow meters and ambient lab conditions. The mass fraction considers the molar fraction as well as the molecular weight ratio between the fuel and the mixture.

$$Y_f = \frac{X_f MW_f}{MW_{mix}} \tag{3.3}$$

An effective specific heat, heat of combustion, and mixture smoke point can also be found based on the mass fraction of fuel. The specific heat is calculated using a weighted average,

$$c_{p,mix} = Y_f c_{p,f} + Y_{N2} c_{p,N2} \tag{3.4}$$

where $c_{p,f}$ and $c_{p,N2}$ are mass-based specific heat values (i.e. kJ/kgK). Note this can also be done using mole-based specific heat values and molar fractions of fuel/nitrogen. The effective heat of combustion is given as

$$\Delta h_{c,e} = Y_f \Delta h_{c,f} \tag{3.5}$$

where $\Delta h_{c,f}$ is the heat of combustion of the fuel in the mixture. An equation for the smoke point of a gaseous mixture comes from [21].

$$L_{SP,mix} = \left(\Sigma\, Y_i / L_{SP,i}\right)^{-1} = \left(Y_f / L_{SP,f} + Y_{N2} / L_{SP,N2}\right)^{-1} \tag{3.6}$$

Table 3-1 shows fuel and nitrogen values used to obtain mixture properties [22], [23], [24]. Densities were calculated using the ideal gas equation at STP (Equation 3.2).

Table 3-1. Properties of gaseous fuels & nitrogen [22], [23], [24].

Gas Properties	**MW** (g/mol)	**ρ_g** (kg/m^3)	**Δh_c** (kJ/g)	**c_p** (kJ/kgK)	**L_{SP}** (mm)
CH_4	16	0.65	49.6	2.23	∞
C_2H_4	28	1.15	41.5	1.56	120
C_3H_6	42	1.72	40.5	1.52	32.8
C_3H_8	44	1.80	43.7	1.67	202
N_2	28	1.15	-	1.04	∞

3.2.2 Fuel Mixture Flow

The readout of the Alicat MC-series flow meters is in SLPM, a volumetric flow. To accurately control the total mass flux of the gas mixture, it is necessary to know the volumetric flows of both fuel and nitrogen. By setting fuel/diluent molar fractions and a desired total mixture volume flow, separate flows for fuel and diluent can be determined.

$$Q_{g,f} = X_f Q_{g,tot} \tag{3.7}$$

$$Q_{g,N2} = X_{N2} Q_{g,tot} \tag{3.8}$$

In these equations Q signifies volumetric flow rate. Then an overall mass flow for the mixture can be calculated using the mixture density.

$$\dot{m}_{g,mix} = \frac{Q_{g,tot}}{\rho_{mix}} \tag{3.9}$$

Equation 3.10 can then be used to determine the total mass flux of the mixture, using

$$\dot{m}''_g = \frac{\dot{m}_g}{A_{sur}} \tag{3.10}$$

$A_{Cu+holes}$ as the surface area. Alternatively, the mass fractions could be used to determine individual mass flows for fuel and nitrogen, and then separately converted to volume flows. Either method yields the same results. Desired flow rates are set into the mass flow meters to obtain the desired total mass flux. Varying heat of combustion (via % diluent) and heat of gasification (via mass flux) gives a range of values representing a spectrum of fuels.

3.2.3 Emulation Potential

To determine which fuels to emulate, an emulation matrix was created. Many common condensed fuels and their properties were inputted into the matrix. These are compared to mixtures of a gaseous fuel mixed with nitrogen. By varying mixture N_2 concentration, each condensed fuel's heat of combustion is matched by that of the gaseous mixture (Equation. 3.5). The resulting mixture smoke point is then calculated using Equation 3.6.

The purpose of the emulation matrix is to assess the ability of a given condensed fuel to be emulated by a given gaseous fuel mixed with nitrogen. The emulation matrix

using ethylene gas is shown in Table 3-2. Properties of the various condensed fuels considered are from multiple sources [23, 24, 25]. With most mixtures able to perfectly match the heat of combustion, the smoke point is used to compare which fuels are better candidates for emulation. The fuel is given an "ok" rating (red) if the mixture's smoke point is within 50% of the condensed fuel, a "good" (yellow) rating if it is within 70%, and a "very good" (green) rating if it is within 85%. Based on the matrix's output using ethylene, methane, and propylene gases, different condensed fuels were burned and then emulated. Methane, propylene, and propane emulation matrices are shown in Appendix B.

Table 3-2. Ethylene/N_2 emulation matrix.

Condensed Fuel Properties					**Emulation Mixture Properties**			
Common Solid and Liquid Fuels					Ethylene			
Formula	Name	Δh_c	L_{SP}	L	Y_{C2H4}	$\Delta h_{c,\,mix}$	$L_{SP,\,mix}$	$\%L_{SP}$
		kJ/g	mm	kJ/g	-	kJ/g	mm	-
Liquids								
CH_3OH	Methanol	19.1	∞	1.005	0.460	19.1	261	NA
C_7H_{16}	*n*-Heptane	41.2	139	0.63	0.993	41.2	121	87%
C_5H_{12}	*n*-Pentane	42.0	163		1.000	41.5	120	74%
C_6H_{14}	*n*-Hexane	41.5	149	0.50	1.000	41.5	120	81%
C_8H_{18}	*n*-Octane	41.0	137	0.98	0.988	41.0	121	89%
C_6H_6	Benzene	27.6	8.79	0.368	0.665	27.6	180	5%
C_2H_5OH	Ethanol	25.6	190	0.776	0.617	25.6	195	98%
CH_3COCH_3	Acetone	27.9	176	0.58	0.672	27.9	178	99%
CH_4O/C_7H_8	Methanol/Toluene	25.7	95	1.034	0.619	25.7	194	49%
Solids								
$C_5H_8O_2$	PMMA	24.2	105	1.6	0.583	24.2	206	51%
CH_2O	POM	14.4	225	2.5	0.347	14.4	346	65%
C_2H_4	Polyethylene (PE)	38.4	45	1.9	0.925	38.4	130	35%
C_3H_6	Polypropylene (PP)	38.6	50	2.0	0.930	38.6	129	39%
C_8H_8	Polystyrene (PS)	27.0	15	1.8	0.651	27.0	184	8%

3.3 Condensed Fuel Burning

From the emulation matrix created, three liquids (ethanol, methanol, and acetone) and four solid plastics (PMMA, PP, PE, and PS) were chosen to attempt to emulate. A

25-mm diameter pan was created out of aluminum foil (δ = 0.024 mm) for burning solid and liquid fuels. The pan has a depth of 6 mm and is insulated on the bottom with a kao wool (or alumino silicate wool) board (δ = 5mm, ρ = 240 kg/m^3) and on the sides with low density insulation (δ = 5mm, ρ = 100 kg/m^3). The insulation is also covered with aluminum foil to prevent liquid fuels from splashing onto the insulation. The pan is placed on a Mettler-Toledo load scale to record mass loss data. Simple Data Logger software is used to control the rate at which the load scale makes measurements. The entire setup was placed on an optical table that is enclosed in a rectangular mesh to reduce air disturbances. For liquid fuels, the load scale is also placed inside of a cylindrical mesh to reduce air disturbances. Due to the difficulty of igniting the solid fuels, the cylindrical mesh was not used for these tests. However, it should be noted

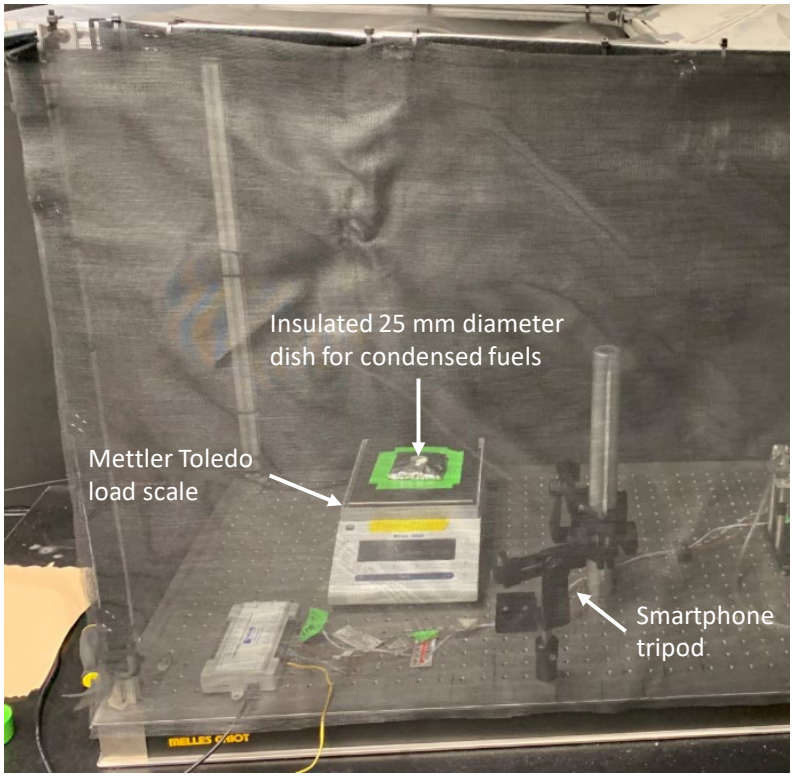

Figure 3-1. Condensed fuel burning apparatus.

that the solid fuel flames were short (<10 cm) and did not seem to be affected much by the air flows present. A smartphone was mounted to a tripod and the height was adjusted so that the lens was flush with the top of the fuel pan. An image of the setup is presented in Figure 3-1.

Fuels were ignited with a butane torch and images were taken approximately every 5 seconds until the fuel ran out. Solid fuels took quite some time to ignite, requiring the butane torch to be moved uniformly around the surface for up to 45

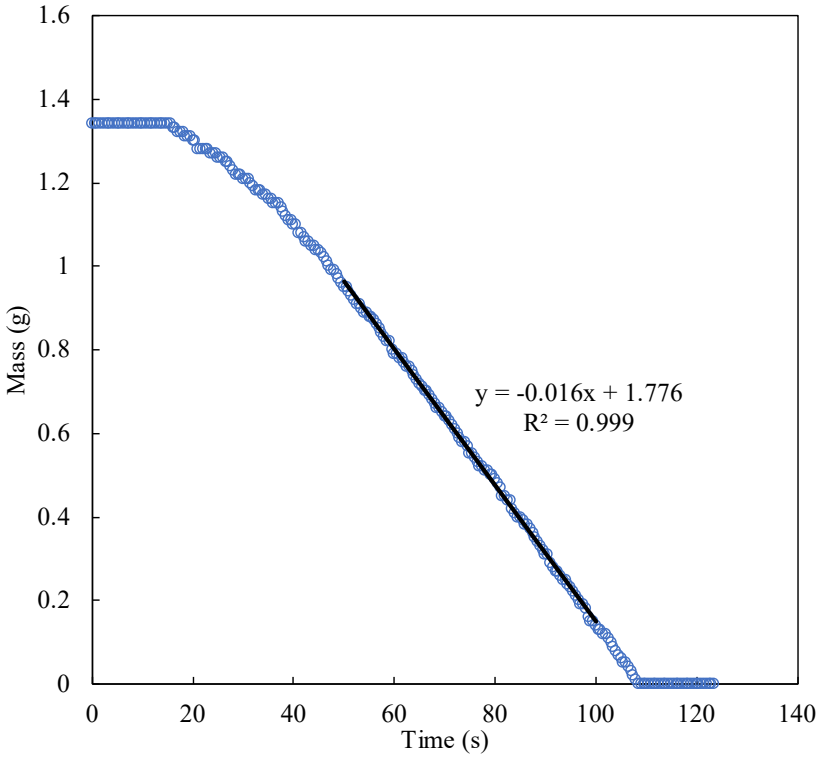

Figure 3-2. Mass loss rate for ethanol.

seconds. After each test, the steady fuel mass loss rate was calculated as the slope of the steady region of the mass vs. time curve from the load scale data. An example plot of the mass loss curve for ethanol is presented in Figure 3-2. Using Equation 3.10, the mass flux from the surface was calculated. This mass flux serves as an initial guess for the mass flux of the fuel mixture to the burner surface.

Flame heights are measured using image analysis performed in Matlab. The script was based off a script from Mathworks [26].The code takes in any amount of flame images, crops them at the pan/burner surface, and converts them to binary. It then uses a user entered value (1-256) to threshold the flame. For the flames in this study, this value ranged from 150-200 to best threshold the flame. Using the known diameter of the pan/burner surface in both cm and pixels (measured in ImageJ), the flame height is calculated for each image. These heights are then averaged for each test to determine the mean flame height, consistent with an 0.5 intermittency flame height. An example

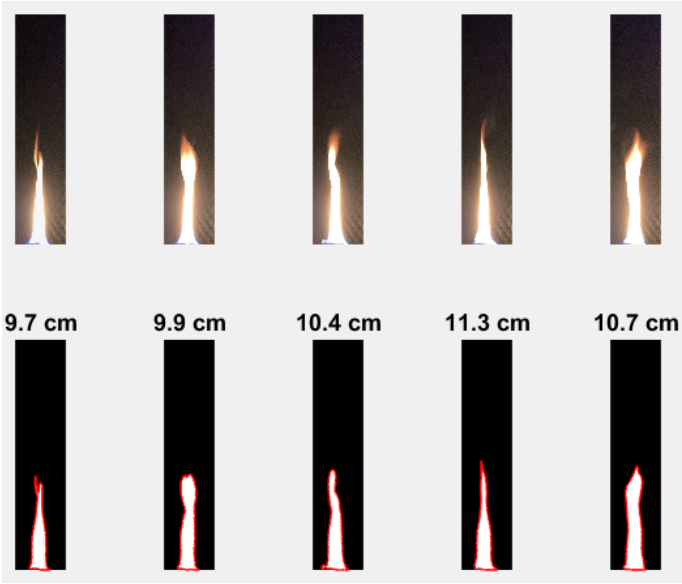

Figure 3-3. Flame bounding example for flame height measurements (PMMA).

of the program being run with some of the PMMA flame images is presented in Figure 3-3. The top row shows raw images cropped around the flame, and the bottom row shows the region bounded by the user-entered value. Measured mass fluxes and flame heights of condensed fuels are reported in Table 3-3. Mass loss rate curves that yield the values in Table 3-3 for condensed fuels other than ethanol are provided in Appendix B.

Table 3-3. Measured condensed fuel properties.

Fuel	$\dot{m}$ (g/s)	$\dot{m}''$ (g/m^{2}s)	z_f (mm)
Ethanol	0.0163	33.2	149
Methanol	0.0093	18.9	48
Acetone	0.0183	37.3	125
PMMA	0.0091	18.5	102
PP	0.0028	5.7	69
HDPE	0.0030	6.1	82
PS	0.0059	12.0	72

3.4 Condensed Fuel Emulation

The emulation matrix was used to determine the best gaseous mixture for emulating each condensed fuel. Those mixtures were then burned at the measured mass flux in order to achieve emulation. This section contains the procedures and methods used as well as a discussion of the results.

3.4.1 Experimental Apparatus

This section describes the setup for the BRE 2 burner used for both emulation and the propane study described in Chapter 4. The burner is mounted vertically on an optical breadboard. The optical breadboard is also enclosed in the rectangular mesh to reduce air disturbances. The top of the mesh is connected to a hood to collect exhaust. To further reduce air disturbances the hood damper was closed, and a cylindrical screen was placed around the burner. The cylindrical screen proved necessary to ensure a quiescent environment and prevent the flame from moving on the surface of the burner. Two small holes were cut in the cylindrical mesh, one to allow a butane torch to reach the burner surface for ignition, and a second to allow a line of sight for the camera. A smartphone was mounted on a tripod so that the lens was at the same height as the

burner surface. Images were taken during experiments for analysis of the flame height and flame base diameter at different flow rates.

Two Alicat MC-series flow meters were used to control fuel and diluent flow to the burner. The settings of these controllers can be changed for different gases, and they have a standard temperature and pressure of 25 °C and 1 atm. For propylene gas, an Omega rotameter was used as propylene is not compatible with the Alicat MC-series. The rotameter calibration is provided in Appendix A. Flexible Swagelok tubing was used to connect gas cylinders to the flow meters as well as the flow meters to the burner. After exiting the flow meters, fuel and diluent flow are connected at a tee to mix. The fuel mixture is then split with a tee near the burner, as it has connections for inflow from both sides. An image of the setup is shown in Figure 3-4.

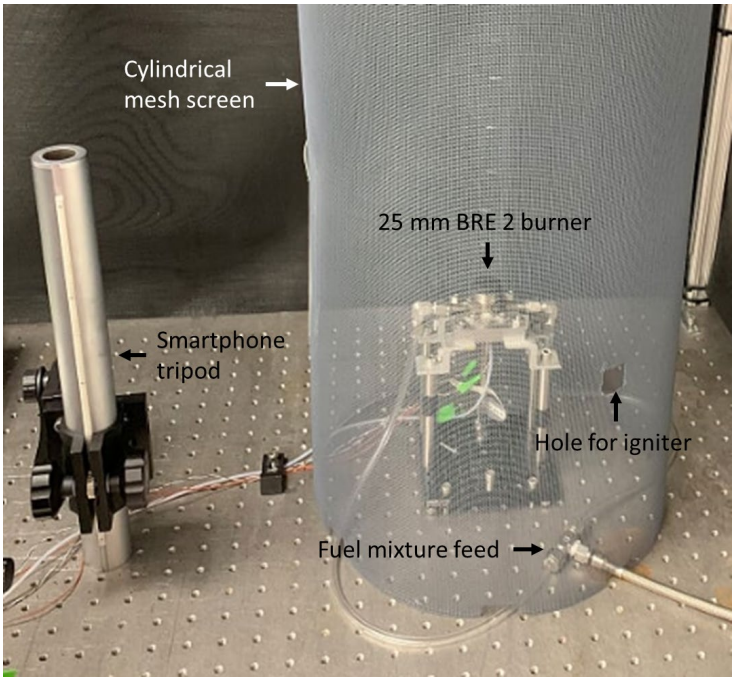

Figure 3-4. 25 mm BRE 2 burner setup for flames.

3.4.2 Emulation with Gaseous Fuel Mixtures

According to the emulation matrix, ethanol can be emulated with a 62% by mass mixture of ethylene and nitrogen. The flow meters operate in 0.001 SLPM increments, so the closest they can accurately produce is a 60% mixture of ethylene. Matching the mass flux as closely as possible, a 60% ethylene flame is run on the burner for 90 seconds. This time is adequate to for a flame to reach steady burning as reflected by the results. Based on the calibration of the 25 mm BRE 2, the calorimeter should accurate for even longer periods of time, although this was unnecessary for the study. Images are taken every 10 seconds and data is read from the burner continuously. These are then analyzed to determine the heat of gasification and flame height to compare to ethanol.

To find the heat of gasification for a gaseous fuel flame, the net heat flux to the surface is first determined. A classical steady burning equation for burning rate is given as

$$\dot{m}''_F = \frac{\dot{q}''_{net}}{L} \tag{3.11}$$

where $\dot{q}''_{net}$ is the net heat flux to the burning surface, and L is the heat of gasification [25]. For pure liquids with a deep fuel level, this is an exact solution. With the ability to control the mass flux (burning rate) of the fuel mixture, determination of net heat flux allows for the calculation of heat of gasification. An equation for $\dot{q}''_{net}$ for flame heating is given as

$$\dot{q}''_{net} = \dot{q}''_{f,r} + \dot{q}''_{f,c} + \dot{q}''_{e} - \varepsilon\sigma\left(T_S^4 - T_\infty^4\right) \tag{3.12}$$

where $\dot{q}''_{f,r}$ is the absorbed flame radiative heat flux, $\dot{q}''_{f,c}$ is the flame convective heat flux, $\dot{q}''_{e}$ is external heat from the environment, and $\varepsilon\sigma\left(T_S^4 - T_\infty^4\right)$ is radiative loss

from the surface (or re-radiation) [25]. In this analysis, the environmental contribution is negligible. The absorbed heat flux, which is determined via the copper calorimeter, is expressed as

$$\dot{q}"_{abs} = \dot{q}"_{f,r} + \dot{q}"_{f,c} \tag{3.13}$$

Combining Equations 3.12 and 3.13 and neglecting external environmental heat flux yields an expression for net heat flux based on absorbed heat flux.

$$\dot{q}"_{net} = \dot{q}"_{abs} - \varepsilon\sigma\left(T_S{}^4 - T_\infty{}^4\right) \tag{3.14}$$

The copper surface of the burner is used as a calorimeter as shown in the previous chapter. Markan [11] presented the heat balance for a porous copper slug calorimeter with a flame,

$$\dot{q}"_{abs}A_{Cu+holes} = (mc)_{Cu}\frac{dT}{dt} + \varepsilon\sigma A_{Cu+holes}\left(T^4 - T_\infty{}^4\right) + \dot{Q}_g + \dot{Q}_{rod} + \dot{Q}_b \tag{3.15}$$

where $(mc)_{Cu}\frac{dT}{dt}$ is an expression for change in internal energy of the burner, $\varepsilon\sigma A_{Cu+holes}\left(T^4 - T_\infty{}^4\right)$ is the re-radiation from the copper surface, $\dot{Q}_g$ is the heat loss to the gas flowing through the burner, $\dot{Q}_{rod}$ is the heat loss to the embedded sensor rods, and $\dot{Q}_b$ is the heat loss from the back of the copper top plate. A full expression for calorimeter net heat flux is given by combining Equations 3.14 and 3.15.

$$\dot{q}"_{net} = (A_{Cu+holes})^{-1}[(mc)_{Cu}\frac{dT}{dt} + \dot{Q}_g + \dot{Q}_{rod} + \dot{Q}_b]$$

Using burner-specific parameters calculated during calibration and temperatures from thermocouples embedded in the burner and sensor surfaces, the calorimeter can be used to calculate $\dot{q}"_{net}$ for a flame, which can in turn be used to determine an effective heat of gasification, L, from Equation 3.11.

The equations used to calculate heat of gasification are applicable during steady burning. Therefore, it is desirable to analyze the steady burning portion of the flame data. This typically corresponded to the last 40-50 seconds of the 90 second flame test. The fact that the flame reaches steady burning within 90 seconds is further justification that this is an adequate length for flame experiments. A transient plot of a typical flame experiment using a gaseous ethylene mixture is presented in Figure 3-5.

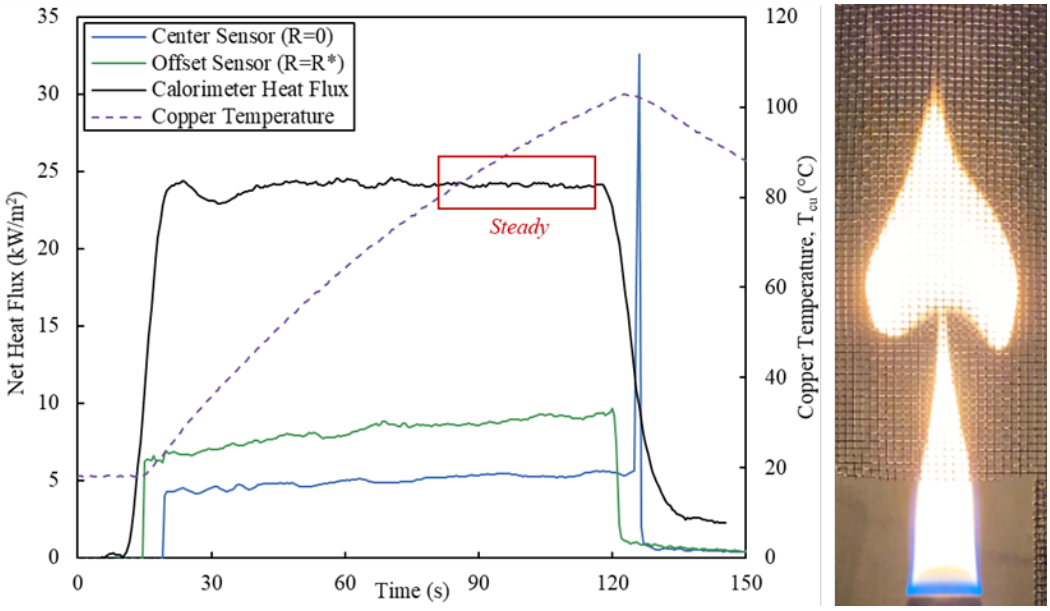

Figure 3-5. (Left) Transient flame data for ethylene mixture at 40 g/m^{2}s.

(Right) Accompanying image of steady flame.

A clear ignition spike is visible during the first 10 seconds of the data and then the calorimeter and sensors adjust while the flame settles on the burner. From the calorimeter curve in Figure 3-5 it is evident that the last ~40 seconds are relatively flat and correspond to steady burning behavior. This is supported by the sensor data, which also seem to settle out in this time period, as well as flame base diameter and flame height, which will be discussed in the next chapter. The steady burning region of each flame is used to determine the net heat flux to the burner for each flame, by averaging

the calorimeter net heat flux (Equation 3.16) over these ~40 seconds. This value is then inserted into Equation 3.11 to determine an effective heat of gasification of the fuel mixture.

Gaseous mixtures with the same heat of combustion and similar smoke point to each condensed fuel are burned at the respective measured mass flux for each condensed fuel. Matching these properties and flowing the proper mass flux should yield an emulation with the same heat of gasification as the condensed fuel. It is difficult to measure a true mass loss rate of a small pool fire due to several factors causing uncertainties. Some of this uncertainty may come in with heat transfer to the aluminum foil pan, which does not have perfectly uniform sides or a perfectly uniform height. Another reason for uncertainty is that the liquid level is slightly dropping throughout the test, so the burning surface is changing and may be affected by flow over the edge of the pan. For some of the solids the results indicate that steady burning may never have quite been reached. From the inputted mass flux, a close heat of gasification and flame height value may be obtained. For example, flowing a 60% (molar) ethylene mixture at 33.2 g/m^2s gave a heat of gasification of 0.72 kJ/g, which is very close to the desired literature value of 0.776 kJ/g for ethanol [25]. This general process was followed for each successfully emulated fuel. Results of performed emulations are summarized in Table 3-4. Images of side by side condensed fuels with their emulations are shown in Figure 3-6 - Figure 3-8.

Table 3-4. Emulation summary.

Fuel		Condensed/Emulated	$\dot{m}''$ g/m^{2}s	Δh_c kJ/g	L_{SP} mm	L kJ/g	z_f mm
Liquids	Ethanol	Pool	33.2	25.6	190	0.776	147
		BRE (X_{C2H4} = 60%)	33.2	24.9	200	0.72	152
	Methanol	Pool	18.9	19.1	∞	1.005	75
		BRE (X_{CH4} = 50%)	18.9	18.0	∞	0.71	101
	Acetone	Pool	37.3	27.9	176	0.58	125
		BRE (X_{C2H4} = 65%)	37.5	27.0	185	0.61	171
Solids	PMMA	Disc	18.5	24.2	105	1.6	102
		BRE (X_{C2H4} = 60%)	18.4	24.9	200	1.44	137
		BRE (X_{C3H6} = 50%)	18.5	24.3	55	1.14	115
	PP	Disc	5.7	38.6	50	2.0	69
		BRE (X_{C3H6} = 90%)	5.6	37.7	35	4.33	55
	HDPE	Disc	6.1	38.4	45	1.9	82
		BRE (X_{C3H6} = 90%)	6.2	37.7	35	3.94	56
	PS	Disc	12.0	27.0	15	1.8	72
		BRE (X_{C3H6} = 55%)	11.9	26.2	51	1.86	106

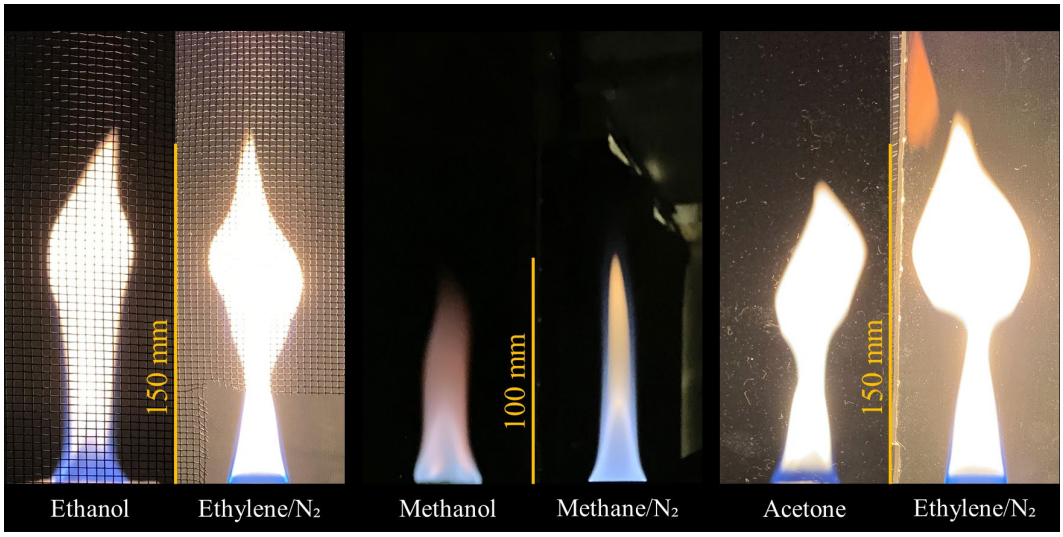

Figure 3-6. Emulation of liquid fuels.

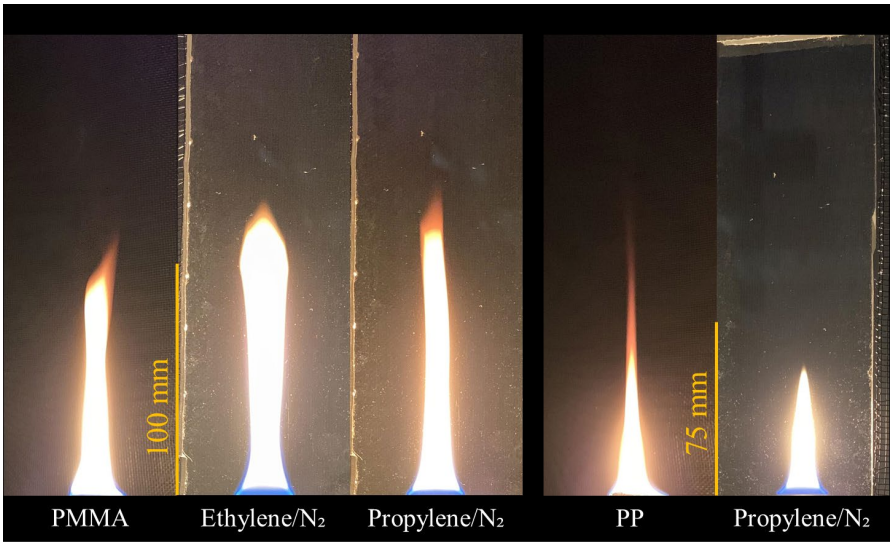

Figure 3-7. Emulation of PMMA (left) and PP (right).

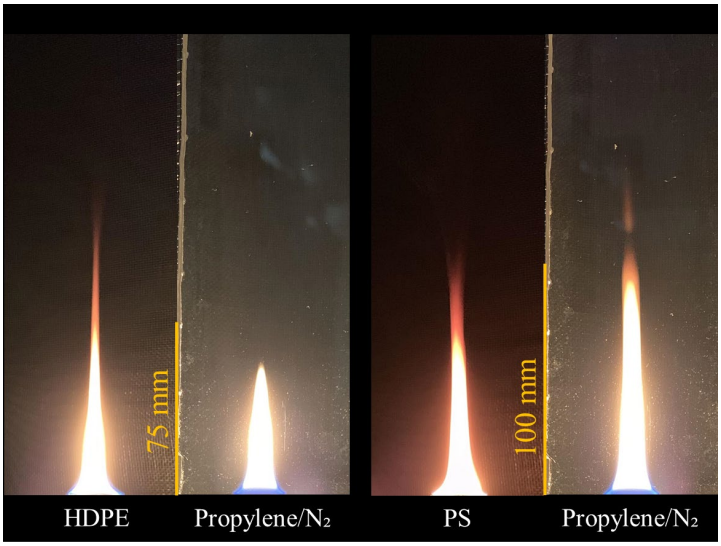

Figure 3-8. Emulation of HDPE (left) and PS (right).

Many of the emulations show clear visual resemblance to their corresponding condensed fuels. There are some discrepancies in flame color and soot production that

can be explained by the fact that not all fuels were good matches with regards to smoke point. The heats of gasification values are also very good matches for ethanol, acetone, and polystyrene. They are slightly worse for methanol and PMMA but are still reasonably close. For both PMMA and methanol emulations, the heat of gasification value of the gaseous mixture is too low, and the flame height is slightly too high. The combination of these indicates that the measured mass flux may be slightly too high. This may be explained by the uncertainties present in the condensed fuel burning apparatus. Decreasing the mass flux by up to 20% of the measured value yields emulations that better match both the flame height and heat of gasification of methanol and PMMA. These values are reported in Table 3-5 and the emulations are shown in Figure 3-9.

Table 3-5. Methanol and PMMA emulations by changing mass flux.

Fuel	Condensed/Emulated	$\dot{m}''$	Δh_c	L_{SP}	L	z_f
		g/m^{2}s	kJ/g	mm	kJ/g	mm
Methanol	Pool	18.9	19.1	∞	1.005	75
	BRE (X_{CH4} = 50%)	14.1	18.0	∞	1.00	80
PMMA	Disc	18.5	24.2	105	1.6	102
	BRE (X_{C2H4} = 60%)	16.4	24.9	200	1.62	115
	BRE (X_{C3H6} = 50%)	13.6	24.3	55	1.60	112

The heat of gasification values obtained by the emulations of PP and HDPE suggest a larger issue (off by a factor of 2). It is possible that these fuels may not have reached truly steady burning during the tests. If this were the case, then these fuels would not have reached their peak steady burning rate during the test. This would affect the net heat flux to the surface and therefore the heat of gasification value. The plastics (other than PMMA) each required a significant amount of time to ignite and after ignition, took even longer to settle to a steady flame height. By this time, much of the

6-mm thick material had already been burned, which could be a reason that truly steady burning was not achieved. To match the *L* value for PP and HDPE, mass fluxes of ~13 g/m^{2}s (X_{C3H6} = 90%) were required, more than double the measured values. In the future, thicker samples could be used to achieve better results. A more proper apparatus for burning condensed fuels is also recommended, with the ability to maintain a constant surface level in relation to the edge of the burning pan. Regardless, the results are promising and serve as further confirmation that specific condensed fuels can be emulated by gaseous fuel mixtures.

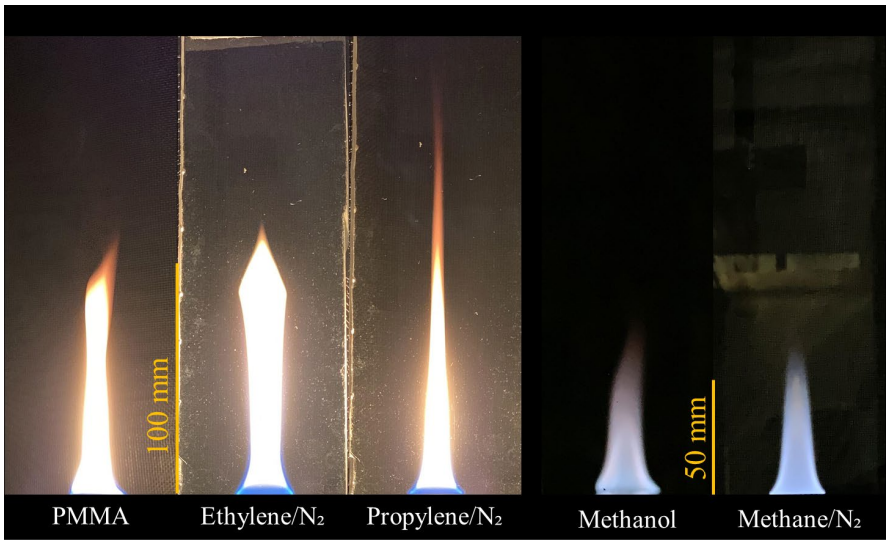

Figure 3-9. Emulation of PMMA (right) and methanol (left).

Chapter 4: Propane Pool Emulation

4.1 Description of Experiments

The purpose of this study is to use the BRE to observe pool fire behavior for a range of different fuels. Propane gas was chosen as it has well known properties and is readily available. However, similar studies could be performed with other fuel gases and would produce similar results. The propane gas is diluted with nitrogen to achieve a wide practical range of effective mixture heats of combustion. Five series of tests were done with different molar fractions of diluent. Each test series was performed with mass flux varying from 1 – 30 g/m^2s, which achieves a range of effective heats of gasification. Properties of the fuel mixtures used are given in Table 4-1. In the chapter, each series is referred to by its heat of combustion. The characteristics of these flames are analyzed and compared to other experimental data and theory from the literature.

Table 4-1. Propane/N_2 mixture properties.

X_{C3H8}	Y_{C3H8}	MW_{mix}	ρ_{mix}	$c_{p,mix}$	$\Delta h_{c,e}$	$L_{SP,mix}$
-	-	g/mol	kg/m^3	kJ/kgK	kJ/g	mm
1.00	1.00	44.0	1.80	1.67	43.7	202
0.80	0.86	40.8	1.67	1.58	37.7	234
0.60	0.70	37.6	1.54	1.48	30.7	288
0.40	0.51	34.4	1.41	1.36	22.4	395
0.20	0.28	31.2	1.28	1.22	12.3	716

4.2 Net Heat Flux

The net heat flux from the flame to the burner surface is the most useful measurement from the BRE for emulation purposes. It allows for the determination of

an effective heat of gasification as explained in 3.4.2. A typical transient plot of burner data from a propane test is shown in Figure 4-1. Again, note that values for both sensors and the calorimeter are steady for approximately the last 40 seconds of the test. An average value over this steady burning period gives the net heat flux data point that is taken for each test.

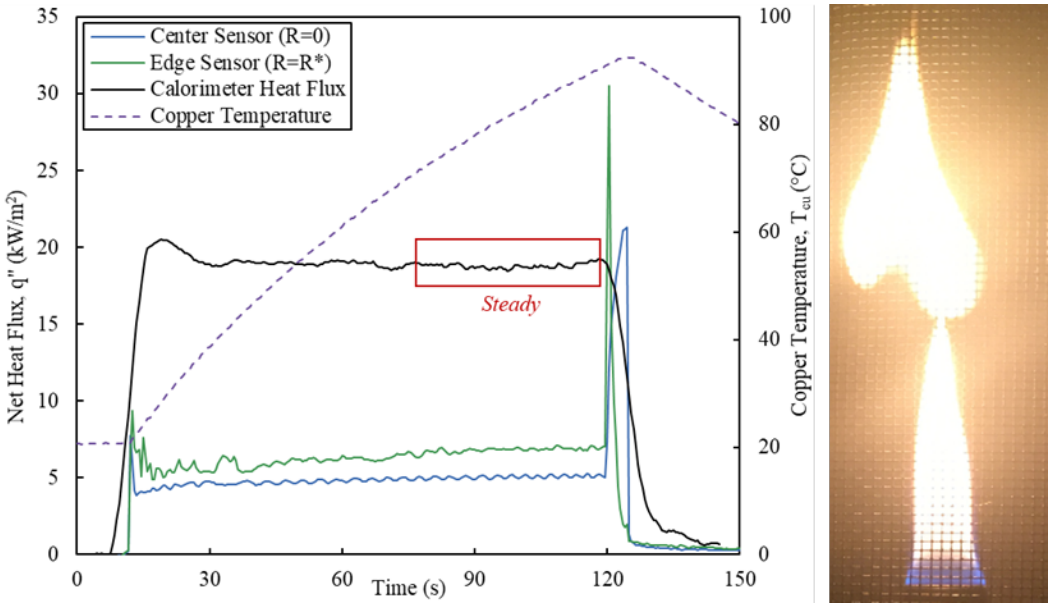

Figure 4-1. (Left) Transient flame data for propane at 20 g/m^{2}s.

(Right) Accompanying image of steady flame.

4.2.1 Series Data

Simulating pool fire behavior with diluted gaseous fuels is not a new idea. A similar study was conducted by Corlett in the 1960's [7]. He varied both fuel gas and diluent and used a 4" diameter burner. However, his results are presented in a fashion that is difficult to translate to modern fire science terms. Regardless, they are comparable (qualitatively) to the results from this study. Corlett's plot of total heat transfer to gas velocity produces the same characteristic shape as the net heat flux vs.

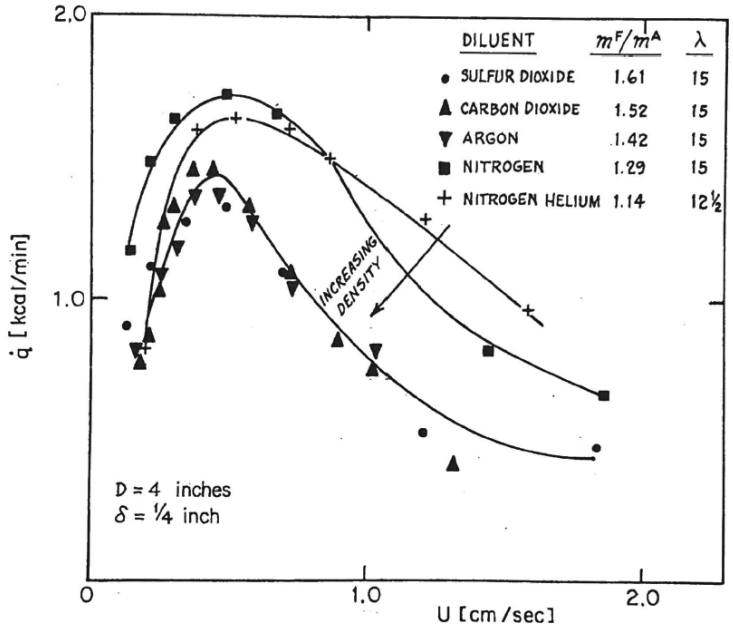

Figure 4-2. Heat transfer vs. velocity data for diluted propane flames, Corlett [6].

mass flux plot that emerges from this study. While the data is presented in a different manner, the relevant axes are related. Corlett's data for diluted propane are shown in Figure 4-2 and those from this study are presented in Figure 4-3.

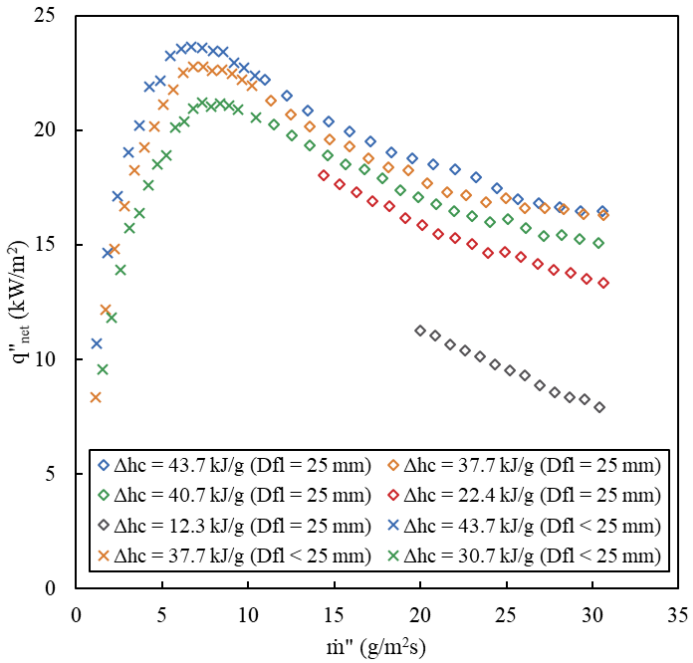

Figure 4-3. Net heat flux vs. mass flux data for diluted propane flames, this study.

Although Corlett used different diluents and axes, the shape of each series' curve is undeniably the same. However, some of the lower mass flow flames do not fill the entire surface of the burner, as shown in Figure 4-4. The effects of this phenomena are discussed thoroughly in the next section.

Figure 4-4. Non-anchored propane flame.

4.2.2 Flame Anchoring

The amount of mass flux needed for the flame to cover the entire surface of the burner has been studied before and was termed the "anchor" point [19]. Plathner remarks that the amount of mass flux needed to anchor a flame to the edge of the burner is much higher than the fire point [19]. Thus, it is possible to have a non-anchored (NA) flame that steadily burns at low mass flows. In Figure 4-3, these non-anchored flames are denoted with an "x" rather than a diamond.

The non-anchored flames create a region where it appears that the heat flux increases with mass flux. It is evident from Corlett's data curves that he observed this behavior as well. However, these heat fluxes are represented incorrectly as the area of

the flame base, A_{fl}, is smaller than the burner area, $A_{Cu+holes}$. In reality, the lower mass flux flames are closer to the burner surface and therefore produce a higher net heat flux over a smaller area. The following attempts to correct the heat flux felt by the burner by using the flame's actual base area.

First, a reasoning is presented for the smaller flames creating a higher heat flux to the surface. A simple expression for conduction over a medium is given as

$$q'' = k\frac{\Delta T}{\delta} \tag{4.1}$$

where k is the thermal conductivity, ΔT is the temperature difference, and δ is distance. For the propane flames studied, conductivity and flame temperature are relatively constant while δ increases with mass flux. Therefore, heat flux at the surface should always decrease proportional to mass flux. This makes sense intuitively as the higher mass fluxes "blow" the flame further from the burner surface. For the anchored flames, this is evident in the second region of the plot in Figure 4-3. This study attempts to correct the region of non-anchored flames using flame base area.

To determine flame base area, a Matlab program like the one used to obtain flame heights was created. This version of the code crops flame images to a small area around the burner and bounds the very bottom of the flame. It uses the known value of the burner diameter in pixels to determine the flame diameter, D_{fl}, in millimeters. Using this method, approximate flame diameters were determined for all non-anchored flames in the first 4 series. Examples of the diameter measurement are shown for the second propane series (Δh_c = 37.7 kJ/g) in Figure 4-5.

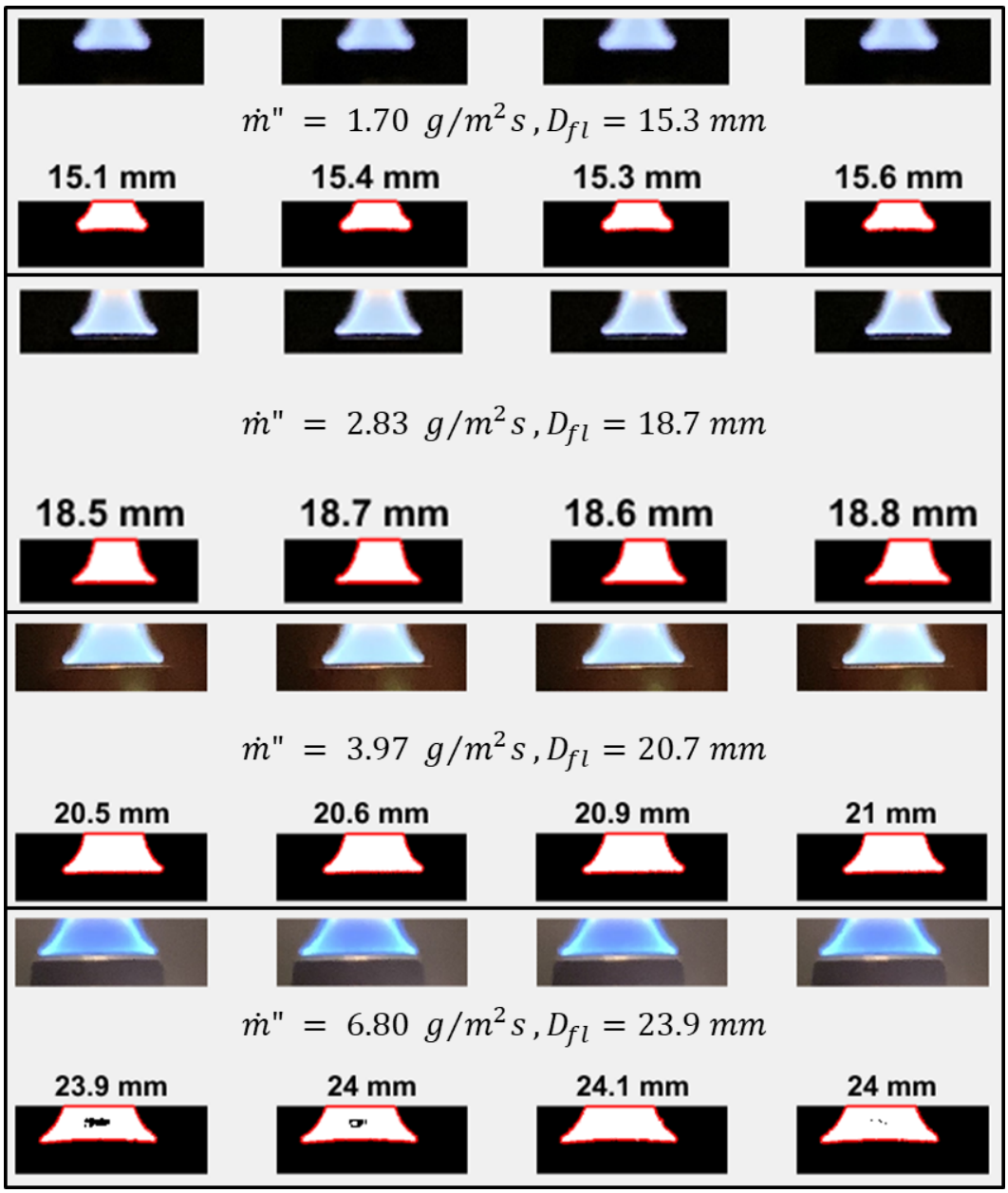

Figure 4-5. Flame diameter determination for non-anchored flames.

The determined flame diameters were used to produce a flame diameter profile for each of the non-anchored flames. These profiles were created for each of the first four series. A polynomial was fit to the profile in order to achieve a smooth curve. The profiles can be seen in Figure 4-6 and Figure 4-7.

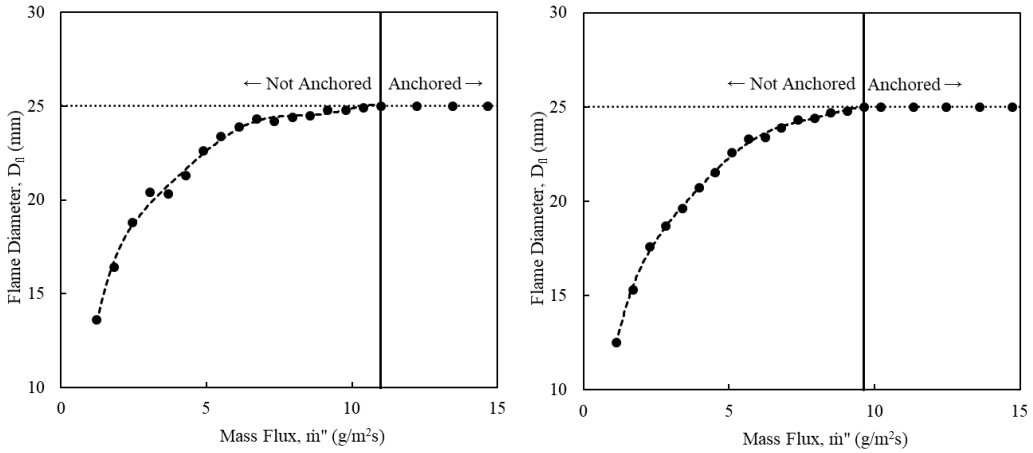

Figure 4-6. Diameters for NA flames. Δh_c = 43.7 kJ/g (left),

Δh_c = 37.7 kJ/g (right).

These flame diameter curves are used to calculate flame base areas, which are used to correct the calorimeter net heat flux to that which is felt from the flame. The first three series indicate a critical mass flux of ~ 10 g/m^{2}s for a propane flame to

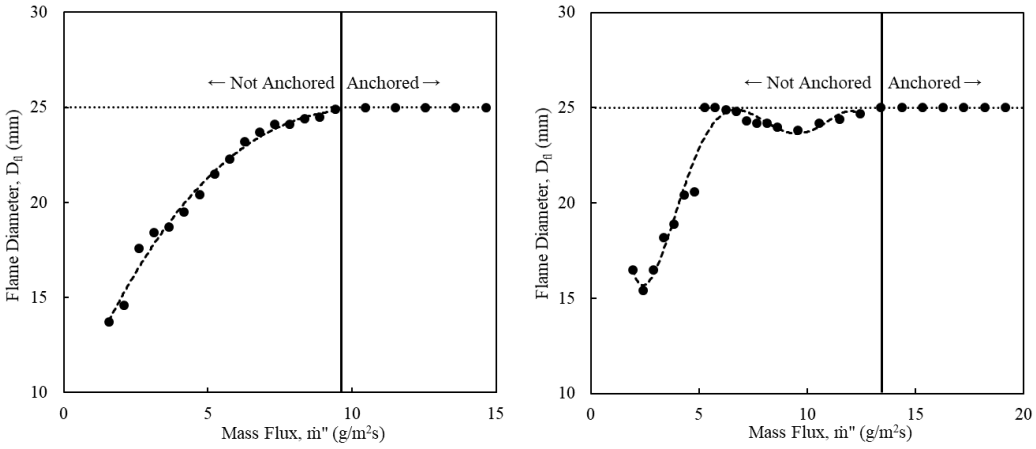

Figure 4-7. Diameters for NA flames. Δh_c = 30.7 kJ/g (left),

Δh_c = 23.4 kJ/g (right).

anchor. Plathner [19] reports that the critical energy flux for propane and methane

flames to anchor is about 400 kW/m^2. Based on this value and dividing by respective Δh_c values, the first three series would be expected to have critical mass fluxes in the range of 9 – 13 g/m^{2}s (increasing with decreasing Δh_c). This range seems to agree with the anchor point determination from this study. Using this value for the fourth series (Δh_c = 23.4 kJ/g), the critical mass flux for the anchor point would be 17 g/m^{2}s, also close to the determined value (14 g/m^{2}s). It is apparent that something else happens with the non-anchored flames in the fourth series (Δh_c = 23.4 kJ/g) in Figure 4-7.

This is a result of extinction behavior that is exhibited by non-anchored flames with higher amounts of dilution. Extinction behavior is most evident in the fifth (most diluted) series (Δh_c = 12.3 kJ/g), which requires a mass flux of 6 g/m^{2}s to even sustain a flame for the full 90 seconds. Non-anchored flames in this series display a repeated flame flickering/fluctuation over the surface of the burner. They rapidly oscillate between a shorter, flatter flame that appears to cover the burner surface and a taller, narrower flame that does not cover the burner surface. It is difficult to capture this with still images, however frames from a video adequately display it in Figure 4-8. These frames are approximately 1 second apart from each other.

Figure 4-8. Non-anchored flame oscillation at 9.6 g/m^{2}s (Δh_c = 12.4 kJ/g).

This behavior occurs in the fourth series as well but is less visually distinct. Due to this behavior and its effect on the flame diameter, non-anchored flames for these two series are considered non-steady and heat flux values are not reported.

For the first three series, an attempt is made to correct heat flux data (Figure 4-3) for the non-anchored flames using the following equation, and the results of its application are shown in Figure 4-9.

$$q"_{net,NA} = \left(\frac{A_{Cu+holes}}{A_{fl}}\right) q"_{net,cal} \tag{4.2}$$

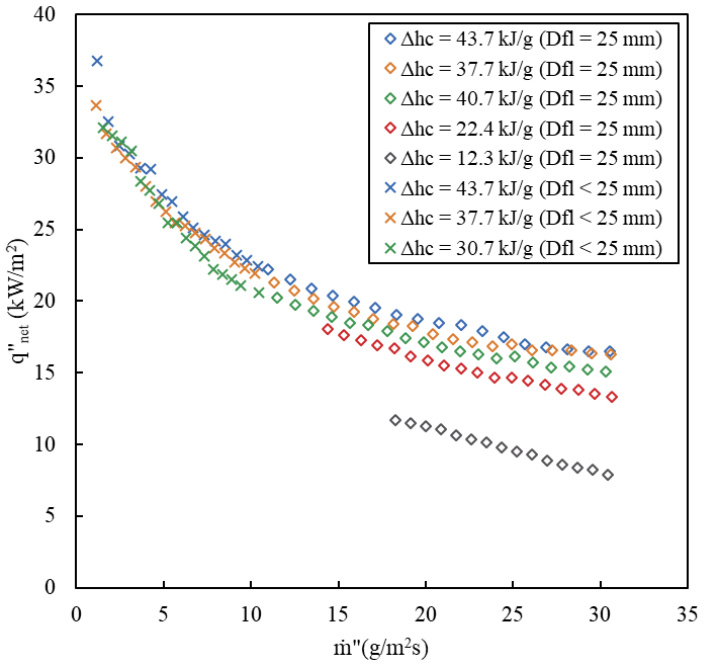

Figure 4-9. Net heat flux with corrected non-anchored points.

The representation of heat flux vs. mass flux presented in Figure 4-9 is more correct than the earlier plot because it displays true flame heat flux over the burning region. However, while non-anchored behavior may be present during the brief ignition and extinction phase for condensed fuels, it is not typical during steady burning [19]. Therefore, they are not suitable for the purpose of comparison to condensed fuel burning. This is supported by the fact that the heat fluxes obtained from these data

points yield nonphysical heats of gasification (7-30 kJ/g). Accordingly, these values are not considered in the following flammability analysis.

4.3 Flammability

The heat flux data for each propane test allows for the calculation of an effective heat of gasification via Equation 3.11. Heat of gasification values obtained from the steady burning region of each anchored flame are shown in Figure 4-10.

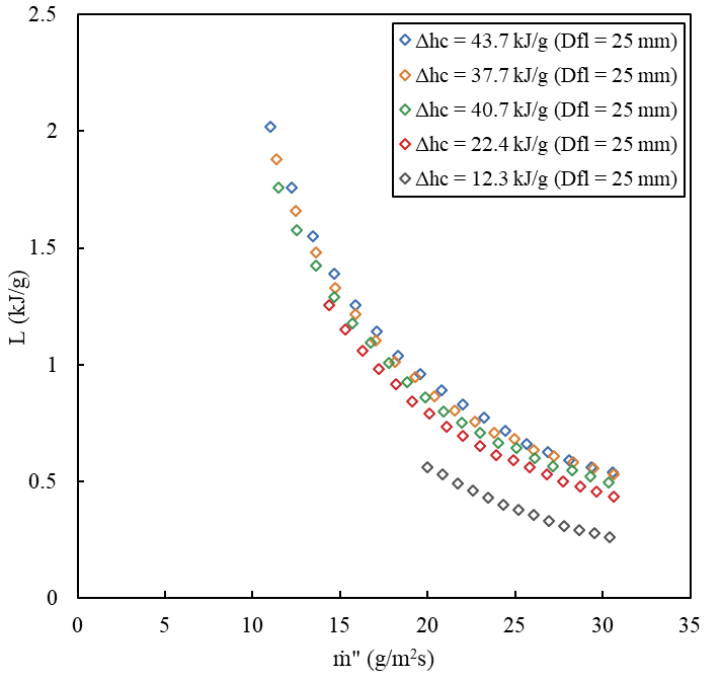

Figure 4-10. Heat of gasification data for propane pools.

These L values allow for the definition of a propane "pool" flammability region. This region is plotted in the realm of heat of gasification and heat of combustion in Figure 4-11. An asymptote past which combustion may not be possible was defined around $\Delta h_c = 5$ kJ/g [19] and is also shown. The upper bound of this region (green line) shows a transition to non-anchored points and further past it, extinction. Below the green line, propane flames should be anchored and flammable. The lower bound (blue

line) defines the heat of gasification values present at 30 g/m^{2}s. Increasing the mass flux past this value would further decrease the obtained L values.

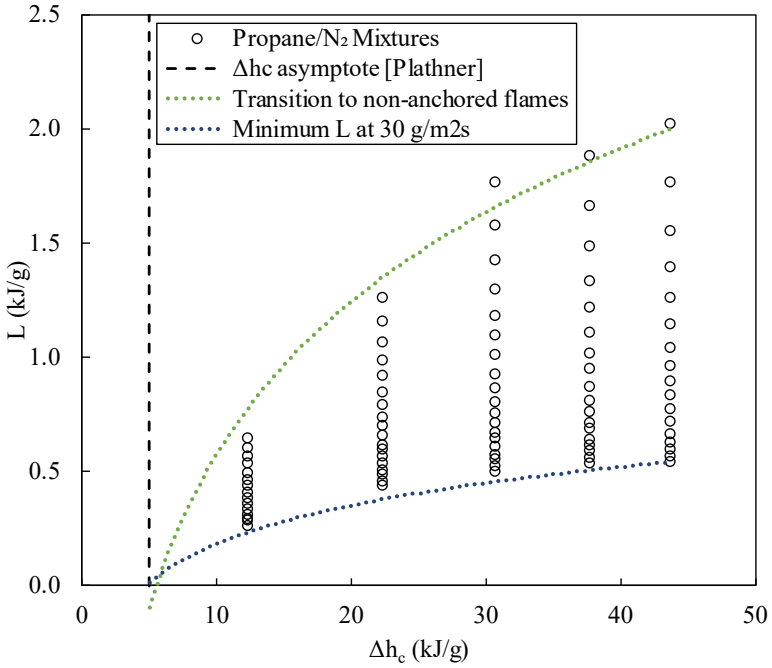

Figure 4-11. Propane pool flammability region.

As one of the four quantities required to emulate condensed fuels, *L* values are also useful to compare these emulated propane pools to physical fuels. Common condensed fuels are plotted alongside the propane flammability region to exhibit the potential of gaseous flame emulation in Figure 4-12. However, these are only two of the four properties needed to successfully emulate a flame. While the surface temperature may not be necessary to obtain a good emulation [14], smoke point is very important as it affects soot production. Therefore, flammability is a function of Δh_c, L_{SP}, and *L*, and a true flammability map would include these 3 axes. Figure 4-13 attempts to offer the reader an understanding of the full flammability map by displaying the relationship between smoke point and heat of gasification for some common gaseous fuels.

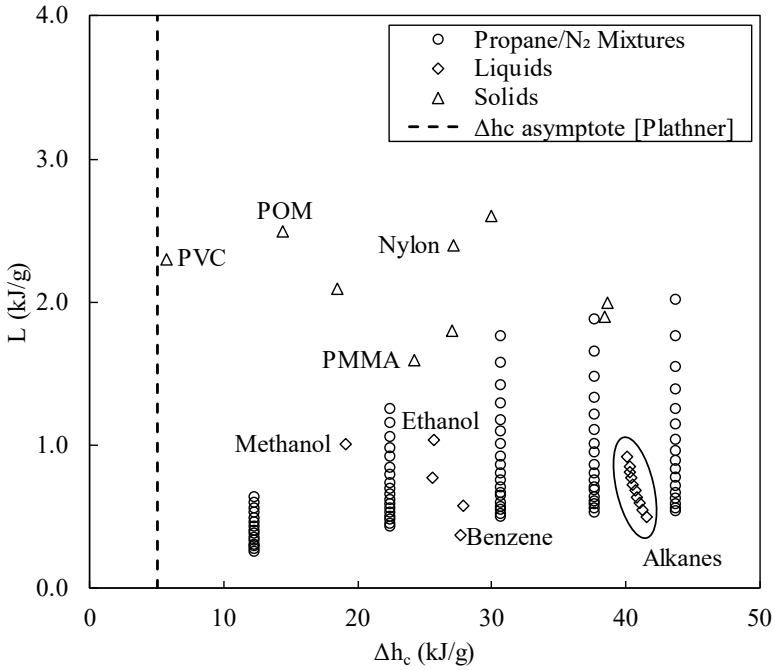

Figure 4-12. Propane pool emulations and condensed fuels.

Due to its high smoke point, propane may not be the best choice for emulating physical fuels. Other gases such as ethylene or propylene could be used in the future to obtain similar results with smoke points that exist in the flammability region of

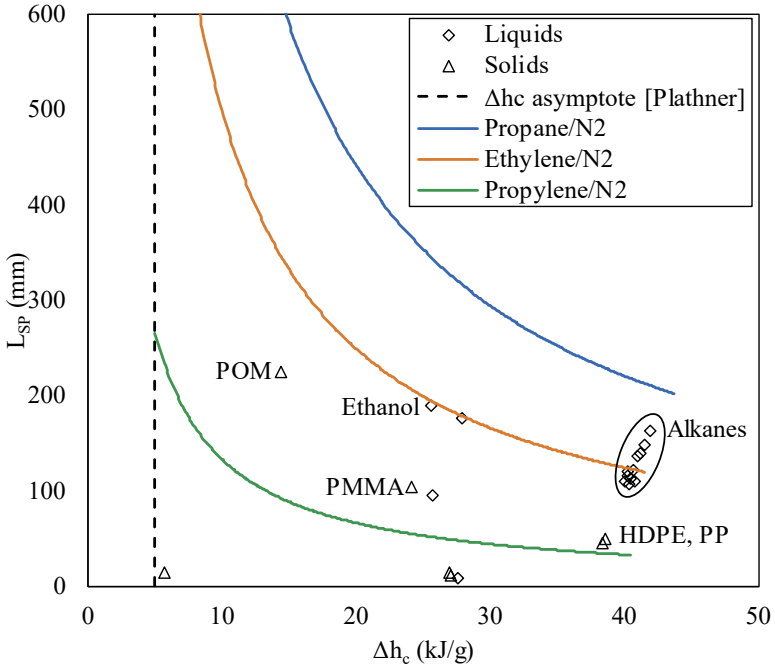

Figure 4-13. Smoke points of gaseous mixtures vs. condensed fuels.

condensed fuels. Regardless, the data further affirms that emulation of pool fires with gaseous fuels is a legitimate approach.

4.4 Preliminary Surface Heat Flux Distribution

Multiple studies in the mid-late 1900's attempted to research the radial variation of pool fire burning rates. These studies were accmoplished by using concentric vessels each fed from a different reservoir to keep the overall liquid level steady. Blinov and Khudyakov first performed this in the 1950's [27] and Akita and Yumoto did their own research in the 1960's [28]. Much later, these studies were cited by Hamins *et al.* who performed his own experiments [29]. The important takeaway from these works is that burning rate per unit area *does* vary with radial location. Due to any fuel's constant heat of gasification, this suggests that the net heat flux to the surface also varies radially (Eqn. 3.11). The current work presents a preliminary glimpse into the radial heat flux distribution for emulated propane fuels.

The values from the heat flux sensors represent the local heat flux at their respective positions (R = 0 mm for the center sensor and R = 8.25 mm for the offset sensor). A rough estimate for the heat flux at the very edge of the flame was determined using Equation 4.1. Assuming δ = 2 mm, ΔT = 1800 K, and using $k(T_{film})$ = 0.06 W/m^{2}K yields a value of 54 kW/m^2 at the burner edge, which is consistent with the heat flux to the offset sensor when the edge of a flame is directly on top of it.

$$q''_{net,\,edge} = \left(0.06 \times 10^{-3}\ \frac{kW}{mK}\right)\frac{(1800\ K)}{0.002\ m}\ = 54\ \frac{kW}{m^2}$$

The calculated edge value along with the local sensor values can be plotted against burner radius for each flame, with an example shown in Figure 4-14. An exponential

curve was then fit through the three points. This was done for each anchored flame in the first series (Δh_c = 43.7 kJ/g). An integration over the surface was then taken using the exponential fit, which yields the total heat to the surface. This value is then converted to neat heat flux over the surface by dividing by the surface area.

$$\dot{Q}_{tot} = \int_0^R \dot{q}"(r) \times (2\pi r) dr \tag{4.3}$$

$$\dot{q}"_{net} = \frac{\dot{Q}_{tot}}{A_{Cu+holes}} \tag{4.4}$$

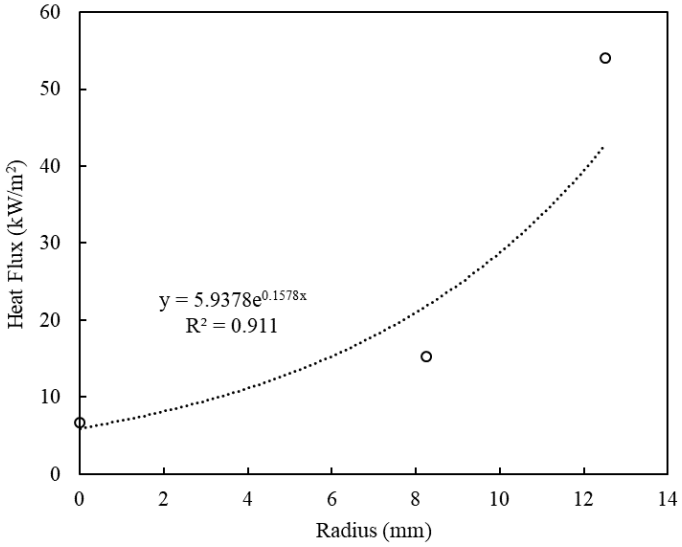

Figure 4-14. Radial heat flux distribution for C_3H_8 flame at 12.2 g/m^{2}s (Δh_c = 43.7 kJ/g).

The net heat flux values from the integration are then compared to those obtained by the calorimeter. They are presented in Table 4-2 and seem to be in good agreement, with the average error within 10%. As this is a very preliminary analysis, these values could of course be refined with a better estimate of the distance from the flame base to the burner, which varies test to test, and more accurate curve fitting.

Table 4-2. Calorimeter and integral heat flux comparison.

Flow	Data			Results			
$\dot{m}''$	$q''_{net,cal}$	$q''_{net,ctr}$	$q''_{net,o}$	$Q_{tot,int}$	$q''_{net,int}$	$q''_{net,cal} - q''_{net,int}$	Difference
g/m^{2}s	*kW/m^2*	kW/m^2	kW/m^2	kW	*kW/m^2*	kW/m^2	%
12.22	*21.5*	6.7	15.3	1.2E-02	*24.4*	-2.9	11.8%
13.44	*20.8*	6.4	12.9	1.1E-02	*22.8*	-1.9	8.5%
14.66	*20.4*	6.1	10.7	1.0E-02	*21.1*	-0.7	3.3%
15.89	*19.9*	5.8	9.9	1.0E-02	*20.4*	-0.4	2.1%
17.11	*19.5*	5.5	8.2	9.3E-03	*18.9*	0.7	3.4%
18.33	*19.0*	5.2	7.4	8.9E-03	*18.1*	1.0	5.3%
19.55	*18.7*	5.1	6.9	8.6E-03	*17.5*	1.2	7.1%
20.77	*18.5*	4.9	6.3	8.3E-03	*16.9*	1.6	9.5%
22.00	*18.3*	4.7	6.0	8.1E-03	*16.5*	1.8	10.8%
23.22	*17.9*	4.6	5.7	7.9E-03	*16.2*	1.8	10.9%
24.44	*17.5*	4.3	5.2	7.6E-03	*15.4*	2.0	13.2%
25.66	*17.0*	4.2	5.1	7.6E-03	*15.4*	1.6	10.4%
26.88	*16.8*	4.1	4.9	7.4E-03	*15.0*	1.8	11.7%
28.11	*16.6*	4.0	4.7	7.3E-03	*14.8*	1.8	12.0%
29.33	*16.5*	4.0	4.7	7.2E-03	*14.7*	1.7	11.7%
30.55	*16.5*	3.9	4.6	7.2E-03	*14.6*	1.9	12.8%

4.5 Flame Height

Flame heights have been extensively studied and correlated throughout the history of fire science. An attempt is made to relate the data from this study to theoretical and experimental curves suggested by past studies. Flame heights of propane are measured using the method explained in 3.3. Due to the oscillation displayed by the last series of propane tests (Δh_c = 12.3 kJ/g), these flame heights were unreliable and were not analyzed. Flame heights from the first four series are presented in Figure 4-15. However, flame heights are related to energy release rate, not mass flux. A simple equation for energy release rate from a flame considers the heat of combustion and mass flow.

$$\dot{Q} = \dot{m}\Delta H_c \tag{4.5}$$

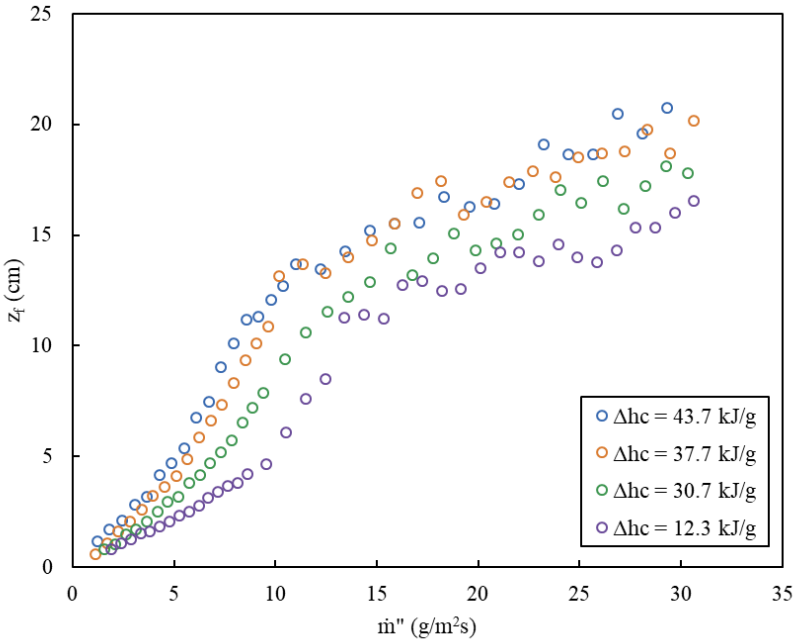

Figure 4-15. Propane flame heights.

Plotting flame height against energy release rate collapses the data, which is shown in Figure 4-16. It is possible to see three "regions" in Figure 4-16 that represent flames that are laminar (0-0.1 kW), transitioning to turbulent (0.1-0.2 kW), and turbulent (0.2+

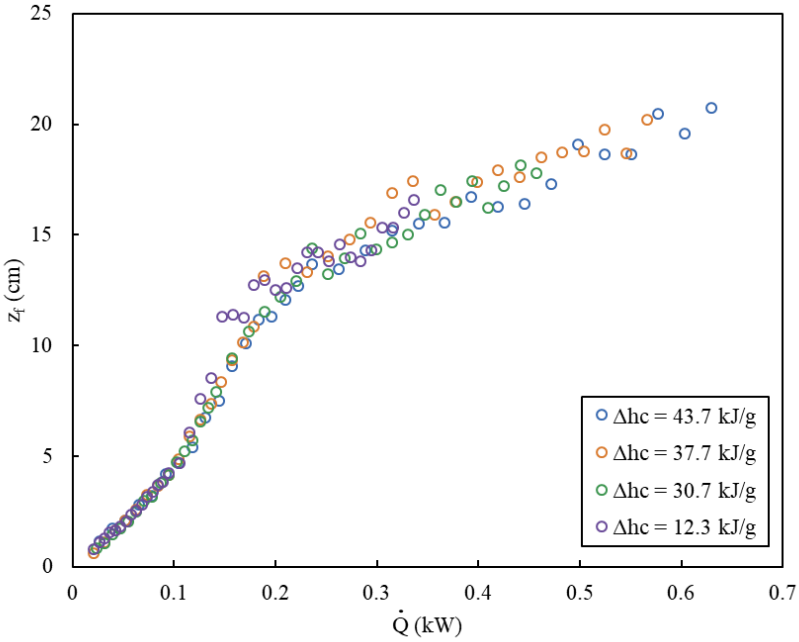

Figure 4-16. Flame heights vs. energy release rate.

kW). Images of representative flames in each region are presented in Figure 4-17. The following section correlates the data with literature which displays these three regions with more clarity.

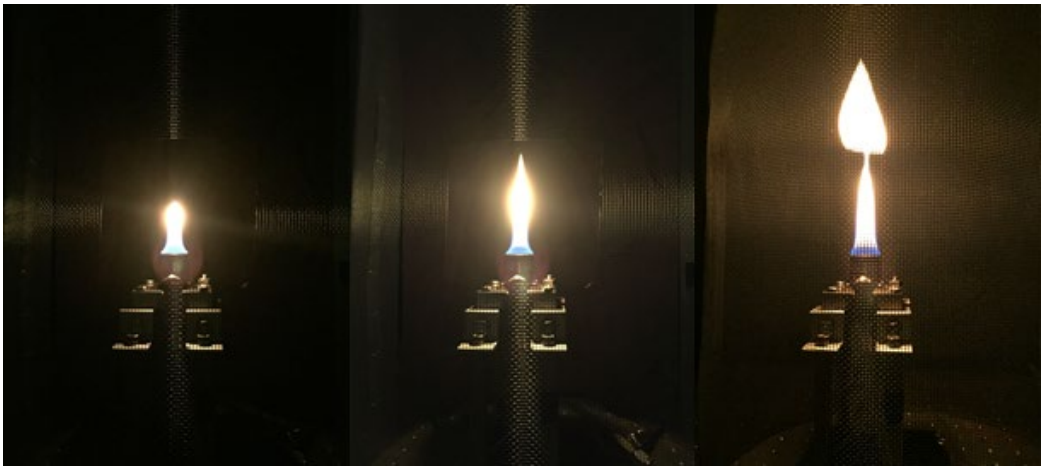

Figure 4-17. Representative flames from laminar (left), transition (middle), and turbulent (right) regions.

4.5.1 Flame Height Correlations

Different flame height correlations have been presented over time. A collection and overview of many of these was assembled by McCaffrey [30]. Most of these correlations focus on a Froude number in terms of energy release rate, also known as Q^* [30]. The Q^* values are then compared to the flame height normalized by the pool/burner diameter.

$$Q^* = \frac{Q}{\rho_\infty c_p T_\infty \sqrt{gD}D^2} \tag{4.6}$$

Equations 4.5 and 4.6 were used to determine a Q^* value for each flame considered in the flame height analysis. For the flames studied, Q^* ranged from 0.2 – 5.8. This allows different correlations to be compared to much of the data from this study. McCaffrey's

Table 4-3. Flame height correlations collected by McCaffrey [29].

TABLE 1-18.2 *Flame Height Correlations*

Symbol (See Figure 1-18.1)	Reference (Fuel, Geometry)*	Q^* Range	H/D	Comments
(Z)	Zukoski[9] (Natural gas, 10–50 cmD Burner)	$Q^* < 0.15$ $0.15 < Q^* < 1$ $1 < Q^* < 40$	$40\ Q^{*2}$ $3.3\ Q^{*2/3}$ $3.3\ Q^{*2/5}$	
(C)	Cox & Chitty[4] (Natural gas, 45, 60 cm square)	$0.13 < Q^* < 0.28$ $0.28 < Q^* < 0.55$	$15.1\ Q^{*2}$ $3.2\ Q^*$	
(T)	Thomas[10] (Wood cribs, 10–200 cm side)	$0.75 < Q^* < 8.8$	$3.4\ Q^{*0.61}$	$\Delta H = 18{,}600\ \frac{kJ}{kg}$ (wood)
(H)	Heskestad[6] (Gas, liquid, solid, literature)	$0.12 < Q^* < 1.2 \times 10^4$	$3.7\ Q^{*2/5} - 1.02$	$\frac{\Delta H}{r} = 3185\ \frac{kJ}{kg\ air}$ (C_2H_4)
(S)	Steward[5] (Literature & gas jets)	$1 < Q^* < 10^4$	$4.16\ Q^{*2/5}$	$\frac{\Delta H}{r} = 3185\ \frac{kJ}{kg\ air}$ $\omega = .0833$
(B)	Becker & Liang[7] (Literature & 0.7–4.6 mm tubes, various gases)	$Q^* < 1.7$ $1.7 < Q^* < 21$ $33 < Q^* < 10^3$ $(20 < \xi_L < 40)$ $10^3 < Q^* < 10^5$ $(1 < \xi_L < 20)$ $Q^* > 10^5$ $(\xi_L < 1)$	$1.52\ Q^{*2}$ $3.6\ Q^{*2/5}$ $\psi = 0.064\ \xi_L - 0.58$ $\psi = 0.18 + 0.022\ \xi_L$ $H/D = 11\ (\beta r)\ \sqrt{\rho_0/\rho_\infty}$	$\frac{\Delta H}{r}\frac{1}{\beta} = 1121\ \frac{kJ}{kg\ air}$ (C_2H_4)

collection of correlations is presented in tabular and graphical format in Table 4-3 and Figure 4-18.

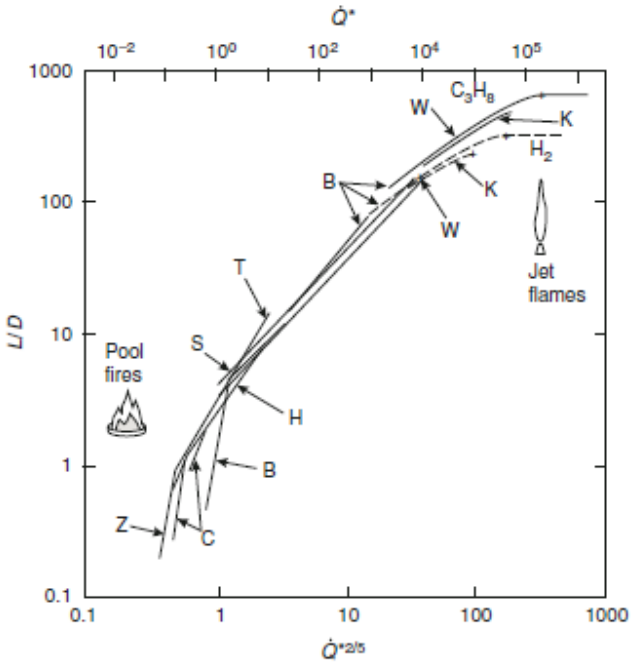

Figure 4-18. Plot of flame height correlations, McCaffrey [29].

A theoretical model was also developed and tested for laminar diffusion flames by Roper [31], [32]. Roper's model is presented differently, in terms of volumetric flow rate, but this can be converted to Q^*. Roper's model for circular port burners is

$$(H/Q) = \{4\pi D_0 \ln(1 + 1/S)\}^{-1}\left(T_0/T_f\right)^{0.67} \tag{4.7}$$

where H is diffusion flame height (also referred to as z_f), Q is volumetric flow rate, and D_0 is the diffusion coefficient (20 mm^2/s). The term S is a ratio of the volume of air to the volume of fuel gas required for complete combustion. It can be simplified to the following expression,

$$S = \frac{MW_f}{MW_{air}} \frac{r}{Y_{O2,\infty}} \tag{4.8}$$

where r is the stoichiometric air-fuel ratio (r = 3.6 for propane) and $Y_{O2,\infty}$ is the ambient oxygen mass fraction. Solving Equation 4.8 for propane yields an S value of 23.68. Inserting this value into Equation 4.7 and dividing both sides by diameter gives the Roper equation in the desired format (z_f/D),

$$z_f/D = 17.91 X_f Q \tag{4.9}$$

where Q is the volumetric flow rate of the overall mixture in LPM. This value is corrected to the flow rate of the fuel gas by X_f.

Flame height data are presented in Figure 4-19 alongside multiple correlations collected by McCaffrey (Heskestad, Becker & Liang, and Steward) and Roper's laminar theory. The data exhibit three clear slopes: $z_f/D \propto Q^*$ in the laminar region, $z_f/D \propto Q^{*2}$ in the transition region, and $z_f/D \propto Q^{*2/5}$ in the turbulent region. The data and these slopes are in good agreement with the historical correlations. Relevant Rayleigh numbers are also presented on the plot.

$$Ra_x = \frac{g\beta(T_f - T_\infty)x^3}{\nu\alpha} \tag{4.10}$$

This equation is evaluated with $T_f = 1500\ K$ using air properties at $T_{film} = 900\ K$. A diameter effect does come into play, which is proved by the Rayleigh numbers. They show that for Heskestad's line (which is based on 10-50 cm pools), the flow is turbulent based on the burner diameter for the entire Q^* range examined ($Ra_D \sim 10^{7\text{-}8}$). For the data from this study, the flow begins laminar based on the Rayleigh number when the diameter is the relevant dimension ($Ra_D \sim 10^4$). However, as the flame height increases, z_f becomes the relevant dimension (z_f > D) and the flow begins to transition to turbulence ($Ra_L \sim 10^7$). This explains the reason that Heskestad's curve has a slope of 2/5 even at low Q^*, while the data from this study reaches this slope at a higher Q^*.

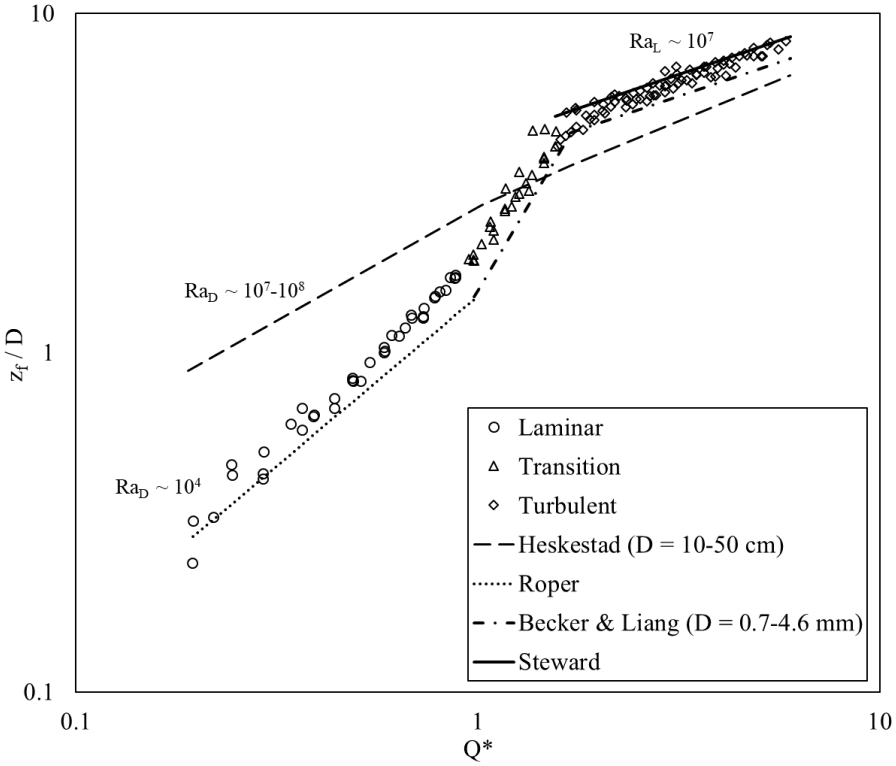

Figure 4-19. Flame height data vs. previous correlations.

4.6 Convective Heat Flux Analysis

Lastly, an initial analysis was conducted with regards to the convective heat flux for the propane flames. The objective is to discover the breakdown between convection and radiation and how it changes between tests at different flows. This analysis relies on the Spalding *B* number, which is a dimensionless representation of the ratio of energy produced by a flame to the energy required for fuel vaporization [25].

$$B = \frac{Y_{O2,\infty}\Delta h_c/r \; - \; c_p(T_{sur} \; - \; T_\infty)}{L} \tag{4.11}$$

Using the chemical heat of combustion for propane (Δh_c = 43.7 MJ/kg), the average peak surface temperature for flame tests (~90 °C), and each flame's heat of gasification, a *B* number can be determined for each flame. The *B* number is useful in investigating the convective heat flux, and from pure convective theory,

$$\dot{m}" = \frac{h_c}{c_p}\ln(1+B) \tag{4.12}$$

$$\dot{q}"_{conv} = \frac{h_c}{c_p}\ln(1+B)\,L \tag{4.13}$$

where h_c is the heat transfer coefficient to the surface. Since the term h_c/c_p is grouped together in Equations 4.12-4.13, the heat transfer coefficient is represented in this manner for much of the analysis. Multiple evaluations of the heat transfer coefficient were performed.

First, Equations 3.12 and 4.13 were combined to relate net heat flux to the heat transfer coefficient.

$$\dot{q}"_{net} = \frac{h_c}{c_p}\ln(1+B)L + \; (\dot{q}"_{rad} \; - \dot{q}"_{rr}) \tag{4.14}$$

This allows for an estimation of h_c/c_p when plotting net heat flux vs. $\ln(1+B)\,L$. The trendlines in Figure 4-20 allow us to visualize Equation 4.14 as the linear dependence of $\dot{q}"_{net}$ on $\ln(1+B)\,L$ where h_c/c_p is the slope of the line and $(\dot{q}"_{rad} - \dot{q}"_{rr})$ is the y-intercept. The slopes of the trendlines indicate h_c/c_p values ranging from 7-9.5 g/m^{2}s with an average around 7.5 g/m^{2}s.

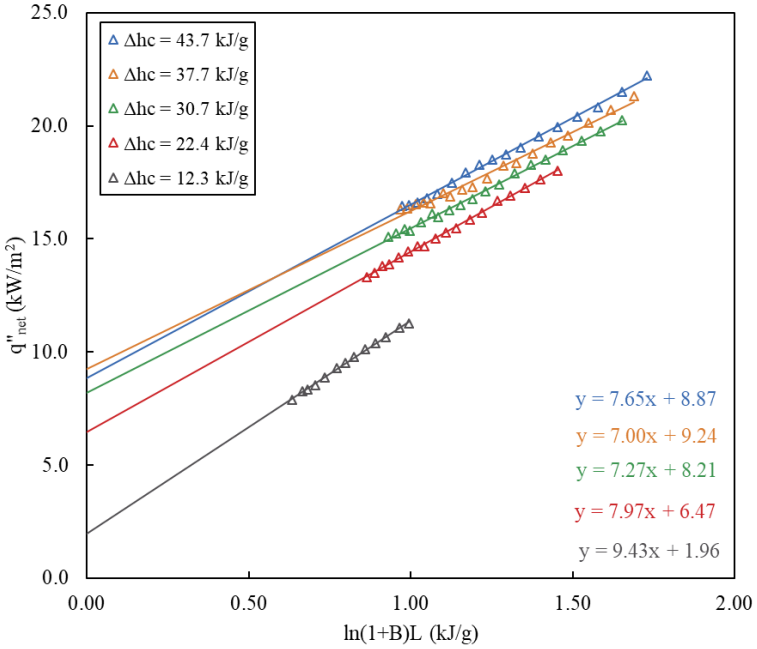

Figure 4-20. Net heat flux vs. ln(1+B)L.

The second evaluation of the convective heat transfer coefficient comes from correlations from the literature. A Nusselt number correlation for horizontal flat plates comes from Gebhart [33],

$$Nu_D = \frac{h_c D}{k} = \left(0.43 + C{Ra_D}^{1/4}\right) \tag{4.15}$$

where the value of C is 0.54-0.60 and Ra_D is evaluated as described in 4.5.1 (Equation 4.10). Solving this expression yields $h_c \approx 15.6\,kW/m^2K$ and results in an approximate h_c/c_p of 14 g/m^{2}s.

The convective heat flux suggested by both h_c/c_p values can be visualized alongside the data by utilizing the dimensionless mass flux, λ.

$$\lambda = \frac{c_p \dot{m}''}{h_c} = \ln(1 + B) \tag{4.16}$$

This emerges from a slight rearrangement of Equation 4.12. Along with Equation 4.11, it can be used to rewrite the convective heat transfer equation (Equation 4.13), with $B = e^{\lambda} - 1$.

$$\dot{q}''_{conv} = \frac{h_c}{c_p}\left(Y_{O2,\infty}\frac{\Delta h_c}{r} - c_p(T_S - T_\infty)\right)\left[\frac{\lambda}{e^{\lambda} - 1}\right] \tag{4.17}$$

In this expression the first two terms are constant (for a given h_c) and the last term, $[\lambda/e^{\lambda} - 1] = [\ln(1 + B)/B]$ drives the convective heat flux. Convective heat flux lines are drawn at h_c/c_p = 7.5 and 14 g/m^{2}s alongside the data for net heat flux in Figure

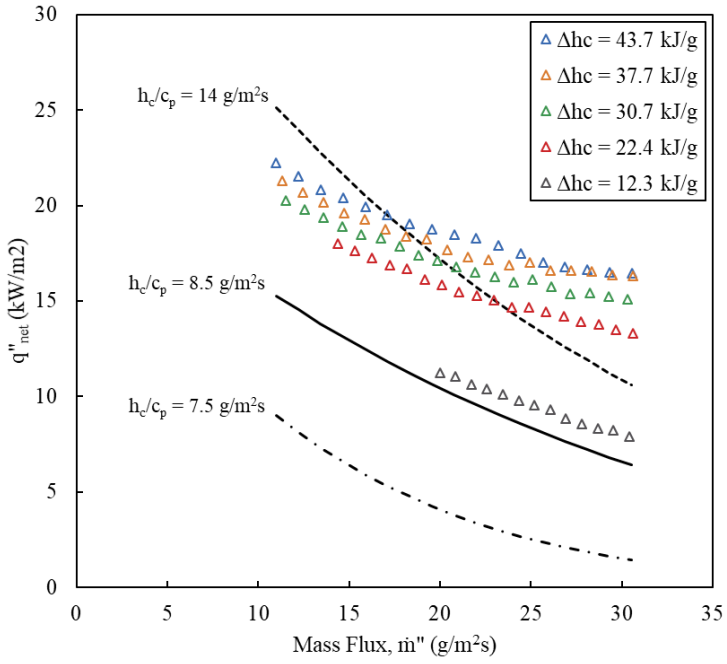

Figure 4-21. Potential convective contribution to surface net heat flux.

4-21. The relation between these two lines and the data suggests that neither of the determined values is completely correct, and that perhaps the true value is closer to 8.5 g/m^2s. This value does however lie in the range of values from the first method.

As the mass flux decreases, the convective heat flux increases and eventually the flame heat flux is pure convection. As the mass flux increases, the net heat flux and convective heat flux lines diverge as radiation plays a more significant role. At the end of the plot, net and convective heat flux become nearly parallel. This suggests that the radiation contribution of heat flux to the surface is close to becoming constant and would do so at a higher mass flux. This trend was observed for propane by Corlett [6] (Figure 4-22).

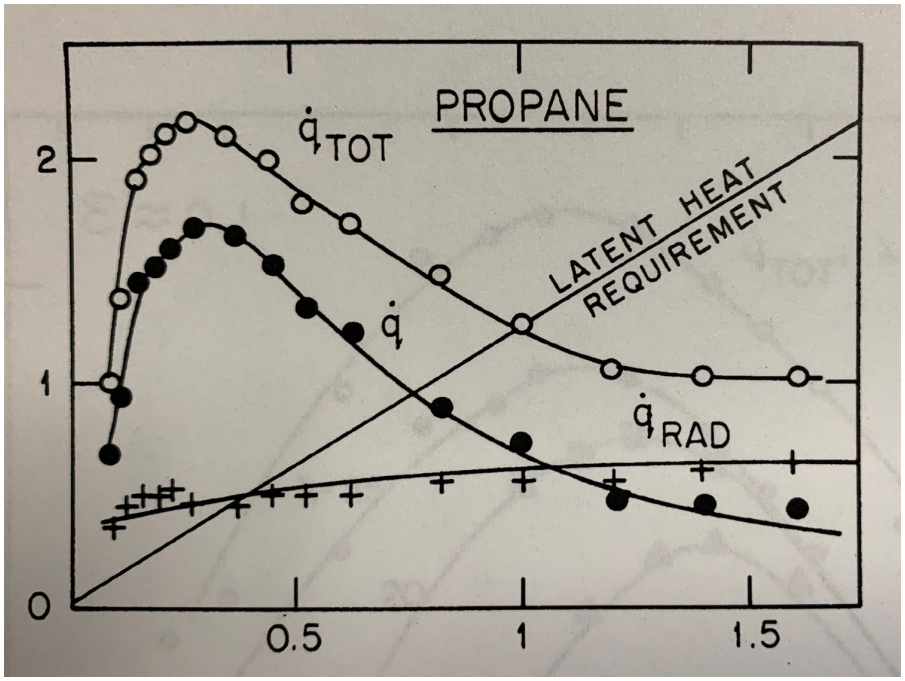

Figure 4-22. Radiative and convective components of heat transfer vs. flow velocity for propane, Corlett [6].

Chapter 5: Conclusions & Future Studies

5.1 Conclusions

The studies performed as a part of this research add to the science of burning emulation. Condensed fuels were again emulated in 1g, with the collection of fuels emulated being expanded from previous work. The results from these tests along with studies using the BRE 2 burner in microgravity [17] suggest that emulation of fuels is possible in 0g.

Emulations of specific condensed fuels using fuel properties are relatively uncomplicated and can be performed with different gaseous fuels as demonstrated by the emulation of PMMA with both ethylene and propylene mixtures.

A top plate calorimeter is the ideal tool to measure net heat flux from a flame to the burning surface. This is useful in determining the effective heat of gasification of a gaseous flame which is a key element of flame emulation. The calorimeter results are supported by local heat flux measurements at different radial locations, which gives further credibility to the calorimeter results and suggests a radial heat flux distribution over the burning surface (like pool fires).

Propane and other gaseous fuels can be used to study a wide range of flammable conditions. They yield pool-like behavior that can simulate fuels in the solid/liquid domain as well as fuels that do not exist in this domain. Controlling the flow and dilution of gaseous fuels allow for the manipulation of certain important fuel properties.

The heat flux distribution and convection analysis add to the study of convectively vs. radiatively dominated pools at different diameters. Burgess and Hertzberg [34] indicate a transition from convectively dominated to radiatively

dominated pools at around 0.1 – 0.5 m diameter. This places the BRE burners (0.025 m & 0.050 m) in the convectively dominated region. The heat flux distribution having the higher measurement at the offset sensor (R^* = 8.25 mm) supports this claim.

5.2 Recommendations for Future Studies

There are quite a few recommendations given for future study. There are plenty of refinements and improvements that can be applied to the science of burning emulation as it has not yet been perfected.

Firstly, expanded emulation matrices should be considered. This would include a larger variety of both condensed fuels and gaseous fuels with which to emulate. Any and all fuels with documented heat of combustion, heat of gasification, and smoke point values should be considered. The possibility of emulating fuels with mixtures of multiple fuels should be explored. This could help to pinpoint the smoke point for emulation purposes and lead to a better match of all fuel emulation properties. Burner diameter should be varied, which is possible using the 50 mm BRE 2 burner.

The burning of condensed fuels and measurement of their properties should be improved. A more accurate apparatus should be created to better maintain liquid level and insulate pool boundaries. Thicker samples may need to be used to ensure fuels reach steady burning.

Flammability maps/diagrams can be created that better correspond to the properties of solid and liquid fuels. This can be achieved by using gaseous fuels with smoke points in the condensed fuel domain such as ethylene and propylene. Flammability maps can be produced in a manner that displays the limits of flammability with regards to heat of combustion, heat of gasification, and smoke point.

The heat flux distribution can be refined and expanded to a range of heats of combustion. Better imaging can be used to determine the flame standoff distance, which would produce a more accurate estimate of heat flux at the edge of the burner. Matlab or another program with more robust curve-fitting than Excel can be used to determine a better integration of heat flux across the surface. Using the 50 mm burner would also be useful to examine this distribution as it would place the flames closer to the radiatively dominated region.

The radiative component of the heat flux can also be studied and attempted to relate to the theoretical convective heat flux analysis presented. A radiometer can be used to measure flame radiation and determine the radiant fraction of energy produced by the flame.

Appendix A: Calibration Supplemental Material

This appendix holds supplemental material for a more complete understanding of the calibration procedures and results. A determination of the heat transfer coefficient from the heat flux gauge rod to the calorimeter is first provided. Air at 50 °C ~ 325 K was used for properties of the medium. The average temperature difference between the heat sensor rods and the copper plate during a calibration is ~ 8 °C which was used for calculation of the Rayleigh number. The diameter of the sensor is 1/16" or 0.00159 m.

Table A-1. Properties of air at 325 K.

β	**k**	**ν**	**α**	**Pr**
(1/K)	(W/mK)	(m^2/s)	(m^2/s)	(-)
0.00308	2.82E-02	1.84E-05	2.62E-05	0.704

$$Ra_D = \frac{g\beta(T_S - T_\infty)D^3}{\alpha\nu} = 2.02 \qquad (A.1)$$

The sensor rod is assumed to be a long horizontal cylinder, for which an approximation is given from the heat transfer text [20].

$$\overline{Nu}_D = \left\{ 0.60 + \frac{0.387 Ra_L^{\frac{1}{6}}}{\left[1 + (0.559/Pr)^{\frac{9}{16}}\right]^{\frac{8}{27}}} \right\}^2 = 0.92 \qquad (A.2)$$

$$h_{conv} = \frac{\overline{Nu}_D k}{D} = 16.3\ W/m^2K \qquad (A.3)$$

A radiative component is also considered. The average sensor and copper temperatures from a calibration are used, which are 47 °C and 55 °C, respectively. The combination of radiative and convective heat yields the total heat transfer coefficient, h_{rod}.

$$q_{rad} = \epsilon(\pi DL)\sigma\left(T_{cu}{}^4 - T_s{}^4\right) = 0.0017\,W = h_{rad}A\Delta T \qquad (A.4)$$

$$h_{rad} = \frac{q_{rad}}{\pi DL \times (\Delta T)} = 6.7\ W/m^2K \qquad (A.5)$$

$$h_{rod} = h_{conv} + h_{rad} = 23.0\ W/m^2K \qquad (A.6)$$

This appendix also contains the full calibration charts used for heat flux calibration for the BRE 2 25 mm burner. They are shown in Figure A-1 and Figure A-2 for the center and offset sensor, respectively. It also contains step plots used for calorimeter calibrations. These are shown in Figure A-4 to Figure A-6 for Calibrations 1-4 using averaged burner specific parameters. Lastly, the calibration for an Omega FL-5521C rotameter used for controlling propylene flow rates is shown in Figure A-7. The gray line shows a previous calibration from 2015 by Dr. Paul Anderson. The rotameter was calibrated using soap bubbles and two graduated cylinders (10 and 100 mL) with marks for known volumes.

Calibration Date	10/10/2018	
Sensor Calibrated (2)	25 mm center	
Diameter (calibrated sensor)	0.0625	inch
α_2 (calibrated sensor)	0.91	
ε_2 (calibrated sensor)	1	
Reference used (1)	SN 180254	
Diameter (reference sensor)	1	inch
α_1 (reference sensor)	0.98	
ε_1 (reference sensor)	1	
Ref calibration constant (C_1)	11.87	kW/m^2/mV
Ref calibration type	absorbed	

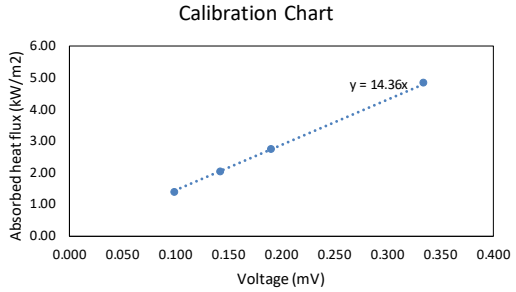

Ambient Temp T_∞ (°C)	Standard reference (1)				Calibrated sensor (2)				
	Voltage E_1 (mV)	Surface Temp $T_{s,1}$ (°C)	HT coefficient h_1 (kW/m^2-K)	Incident HF $\dot{q}_i''$ (kW/m^2)	Voltage E_2 (mV)	Surface Temp $T_{s,2}$ (°C)	Copper Temp $T_{Cu,2}$ (°C)	HT coefficient h_2 (kW/m^2-K)	Absorbed HF (kW/m^2)
23.37	0.128	19.01	0.0059	1.50	0.100	24.63	25.28	0.0195	1.37
23.56	0.190	19.20	0.0059	2.24	0.143	39.14	42.17	0.0260	2.02
23.27	0.257	19.93	0.0056	3.07	0.191	40.36	42.65	0.0261	2.75
23.75	0.453	21.21	0.0052	5.45	0.334	63.36	68.60	0.0297	4.83

Slope C_2 14.36 kW/m2/mV

Figure A-1. Calibration chart for BRE 2 25 mm center sensor.

Calibration Date	10/10/2018

Sensor Calibrated (2)	25 mm center	
Diameter (calibrated sensor)	0.0625	inch
α_2 (calibrated sensor)	0.91	
ε_2 (calibrated sensor)	1	

Reference used (1)	SN 180254	
Diameter (reference sensor)	1	inch
α_1 (reference sensor)	0.98	
ε_1 (reference sensor)	1	
Ref calibration constant (C_1)	11.87	kW/m^2/mV
Ref calibration type	absorbed	

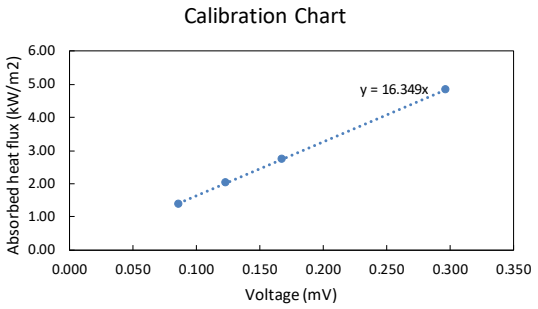

Ambient Temp T_∞ (°C)	Standard reference (1)				Calibrated sensor (2)				
	Voltage E_1 (mV)	Surface Temp $T_{s,1}$ (°C)	HT coefficient h_1 (kW/m^2-K)	Incident HF $\dot{q}''_i$ (kW/m^2)	Voltage E_2 (mV)	Surface Temp $T_{s,2}$ (°C)	Copper Temp $T_{Cu,2}$ (°C)	HT coefficient h_2 (kW/m^2-K)	Absorbed HF (kW/m^2)
23.37	0.128	19.01	0.0059	1.50	0.086	25.86	27.20	0.0211	1.38
23.56	0.190	19.20	0.0059	2.24	0.124	36.99	39.82	0.0255	2.03
23.27	0.257	19.93	0.0056	3.07	0.168	42.87	45.91	0.0267	2.75
23.75	0.453	21.21	0.0052	5.45	0.297	57.45	61.84	0.0289	4.85

Slope C_2 16.35 kW/m2/mV

Figure A-2. Calibration chart for BRE 2 25 mm offset sensor.

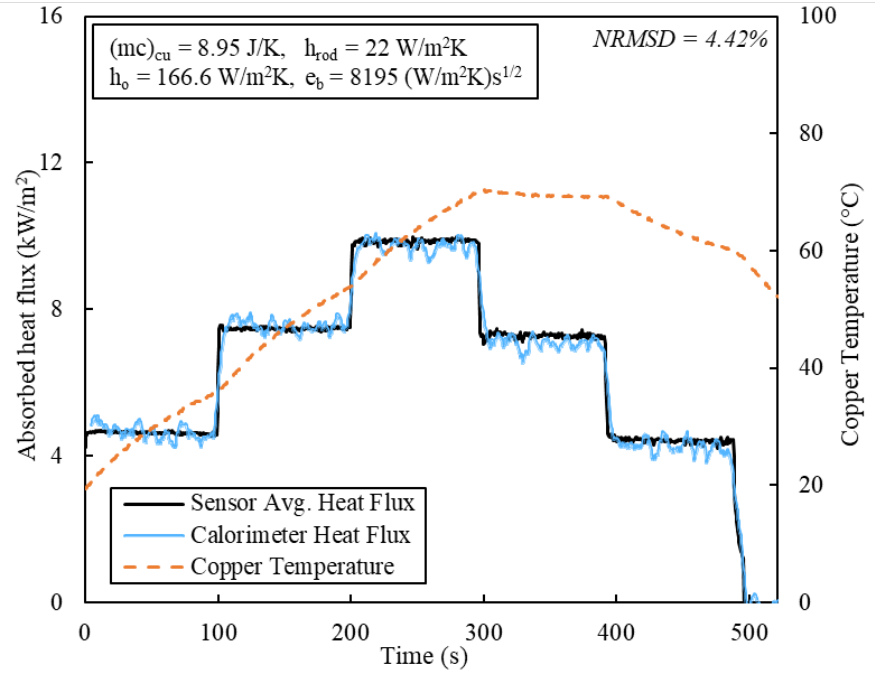

Figure A-3. Calorimeter calibration 1 using average parameters.

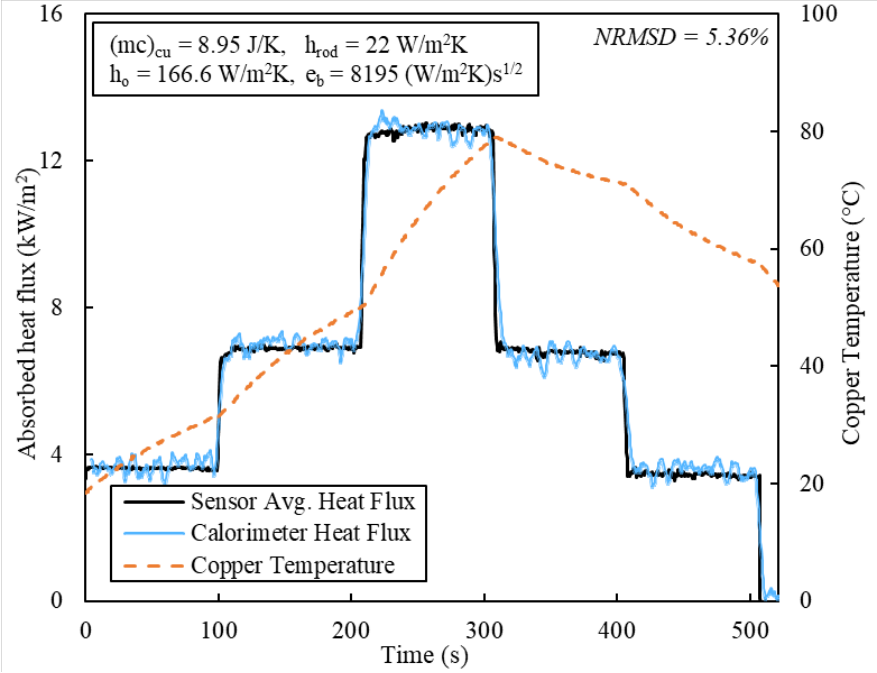

Figure A-4. Calorimeter calibration 2 using average parameters.

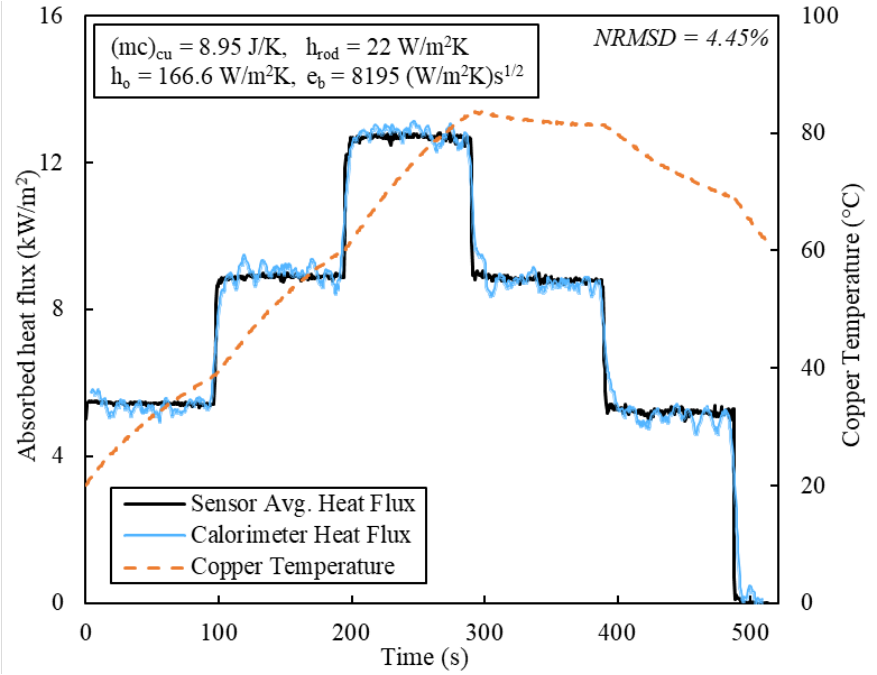

Figure A-5. Calorimeter calibration 3 using average parameters.

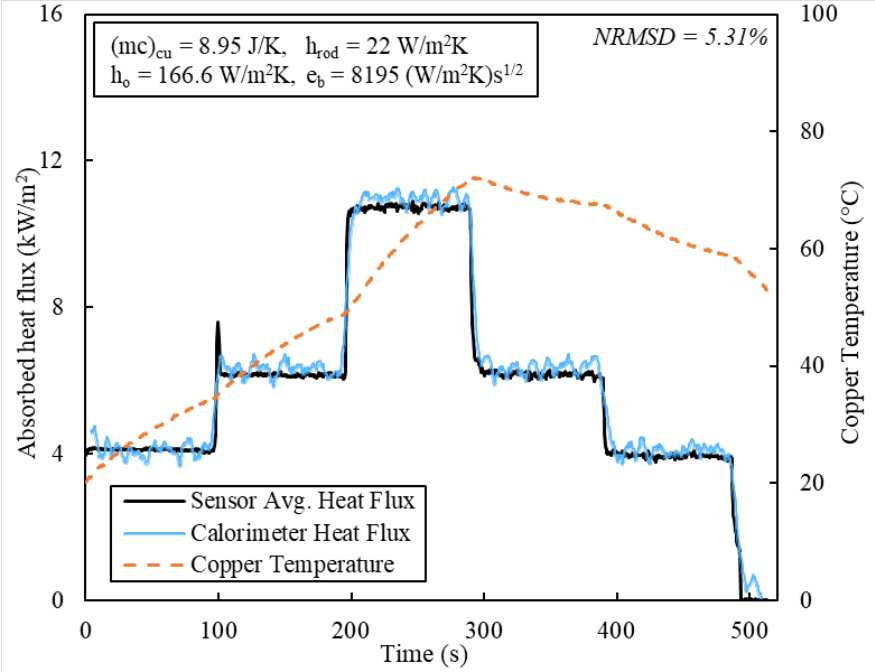

Figure A-6. Calorimeter calibration 4 using average parameters.

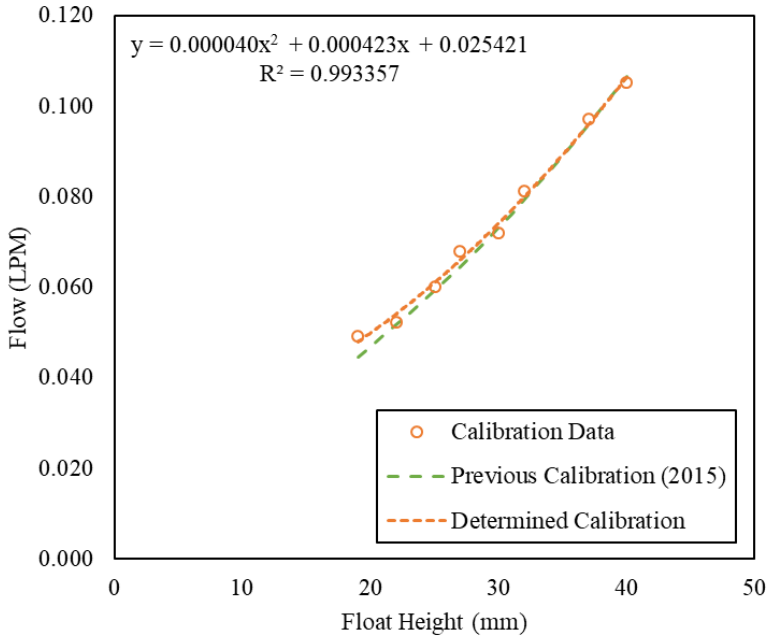

Figure A-7. Omega rotameter calibration.

Appendix B: Condensed Fuel Emulation Supplementary Material

This appendix contains supplemental material for the emulation of condensed fuels. Table B-1 to Table B-3 show the emulation matrices for methane, propylene, and propane which against the condensed fuels considered for this study. Mass loss rate plots are provided for methanol, acetone, PMMA, PP, HDPE, and PS in Figure B-1 – Figure B-3, respectively. The matlab script used to analyze flame heights via flame images is also provided in B.2.

Table B-1. Methane/N_2 emulation matrix.

Condensed Fuel Properties					**Emulation Mixture Properties**			
Common Solid and Liquid Fuels					Methane			
Formula	Name	Δh_c	L_{SP}	L	Y_{CH4}	$\Delta h_{c,\,mix}$	$L_{SP,\,mix}$	$\%L_{SP}$
		kJ/g	mm	kJ/g	-	kJ/g	mm	-
Liquids								
CH_3OH	Methanol	19.1	∞	1.005	0.385	19.1	∞	100%
C_7H_{16}	*n*-Heptane	41.2	139	0.63	0.831	41.2	∞	-
C_5H_{12}	*n*-Pentane	42.0	163		0.847	42.0	∞	-
C_6H_{14}	*n*-Hexane	41.5	149	0.50	0.837	41.5	∞	-
C_8H_{18}	*n*-Octane	41.0	137	0.98	0.827	41.0	∞	-
C_6H_6	Benzene	27.6	8.79	0.368	0.556	27.6	∞	-
C_2H_5OH	Ethanol	25.6	190	0.776	0.516	25.6	∞	-
CH_3COCH_3	Acetone	27.9	176	0.58	0.563	27.9	∞	-
CH_4O/C_7H_8	Methanol/Toluene	25.7	95	1.034	0.518	25.7	∞	-
Solids								
$C_5H_8O_2$	PMMA	24.2	105	1.6	0.488	24.2	∞	-
CH_2O	POM	14.4	225	2.5	0.290	14.4	∞	-
C_2H_4	Polyethylene (PE)	38.4	45	1.9	0.774	38.4	∞	-
C_3H_6	Polypropylene (PP)	38.6	50	2.0	0.778	38.6	∞	-
C_8H_8	Polystyrene (PS)	27.0	15	1.8	0.544	27.0	∞	-

Table B-2. Propylene/N_2 emulation matrix.

Condensed Fuel Properties					Emulation Mixture Properties			
Common Solid and Liquid Fuels					Propylene			
Formula	Name	Δh_c	L_{SP}	L	Y_{C3H6}	$\Delta h_{c,\,mix}$	$L_{SP,\,mix}$	$\%L_{SP}$
		kJ/g	mm	kJ/g	-	kJ/g	mm	-
Liquids								
CH_3OH	Methanol	19.1	∞	1.005	0.472	19.1	70	NA
C_7H_{16}	*n*-Heptane	41.2	139	0.63	1.000	40.5	33	24%
C_5H_{12}	*n*-Pentane	42.0	163		1.000	40.5	33	20%
C_6H_{14}	*n*-Hexane	41.5	149	0.50	1.000	40.5	33	22%
C_8H_{18}	*n*-Octane	41.0	137	0.98	1.000	40.5	33	24%
C_6H_6	Benzene	27.6	8.79	0.368	0.681	27.6	48	18%
C_2H_5OH	Ethanol	25.6	190	0.776	0.632	25.6	52	27%
CH_3COCH_3	Acetone	27.9	176	0.58	0.689	27.9	48	27%
CH_4O/C_7H_8	Methanol/Toluene	25.7	95	1.034	0.635	25.7	52	54%
Solids								
$C_5H_8O_2$	PMMA	24.2	105	1.6	0.598	24.2	55	52%
CH_2O	POM	14.4	225	2.5	0.356	14.4	92	41%
C_2H_4	Polyethylene (PE)	38.4	45	1.9	0.948	38.4	35	77%
C_3H_6	Polypropylene (PP)	38.6	50	2.0	0.953	38.6	34	69%
C_8H_8	Polystyrene (PS)	27.0	15	1.8	0.667	27.0	49	30%

Table B-3. Propane/N_2 emulation matrix.

Condensed Fuel Properties					Emulation Mixture Properties			
Common Solid and Liquid Fuels					Propane			
Formula	Name	Δh_c	L_{SP}	L	Y_{C3H8}	$\Delta h_{c,\,mix}$	$L_{SP,\,mix}$	$\%L_{SP}$
		kJ/g	mm	kJ/g	-	kJ/g	mm	-
Liquids								
CH_3OH	Methanol	19.1	∞	1.005	0.437	19.1	462	NA
C_7H_{16}	*n*-Heptane	41.2	139	0.63	0.943	41.2	214	65%
C_5H_{12}	*n*-Pentane	42.0	163		0.961	42.0	210	78%
C_6H_{14}	*n*-Hexane	41.5	149	0.50	0.950	41.5	213	70%
C_8H_{18}	*n*-Octane	41.0	137	0.98	0.938	41.0	215	64%
C_6H_6	Benzene	27.6	8.79	0.368	0.632	27.6	320	3%
C_2H_5OH	Ethanol	25.6	190	0.776	0.586	25.6	345	55%
CH_3COCH_3	Acetone	27.9	176	0.58	0.638	27.9	316	56%
CH_4O/C_7H_8	Methanol/Toluene	25.7	95	1.034	0.588	25.7	343	28%
Solids								
$C_5H_8O_2$	PMMA	24.2	105	1.6	0.554	24.2	365	29%
CH_2O	POM	14.4	225	2.5	0.330	14.4	613	37%
C_2H_4	Polyethylene (PE)	38.4	45	1.9	0.879	38.4	230	20%
C_3H_6	Polypropylene (PP)	38.6	50	2.0	0.883	38.6	229	22%
C_8H_8	Polystyrene (PS)	27.0	15	1.8	0.618	27.0	327	5%

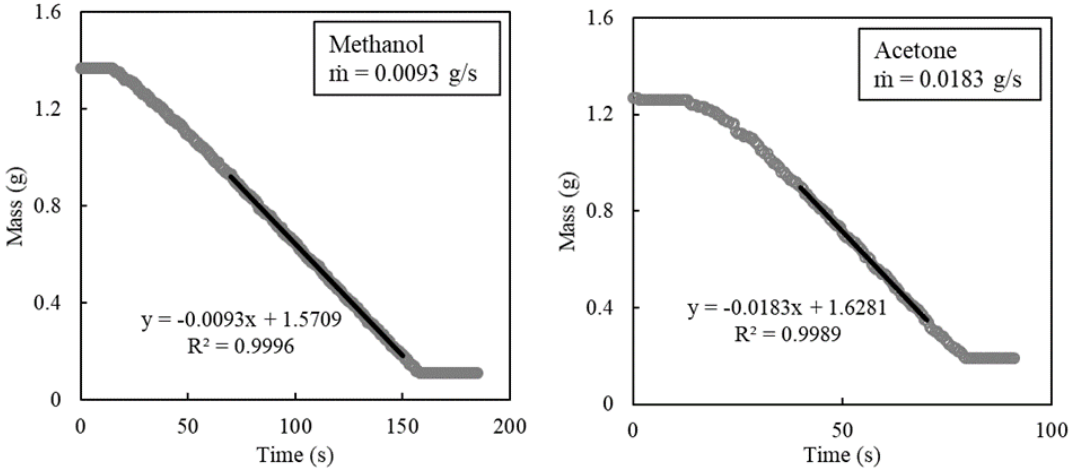

Figure B-1. Methanol (left) and acetone (right) mass loss rate curves.

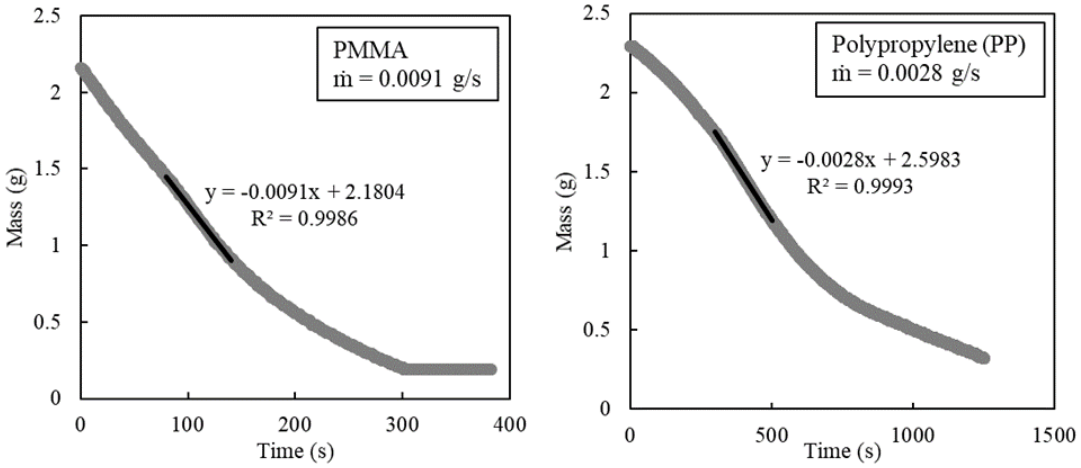

Figure B-2. PMMA (left) and PP (right) mass los rate curves.

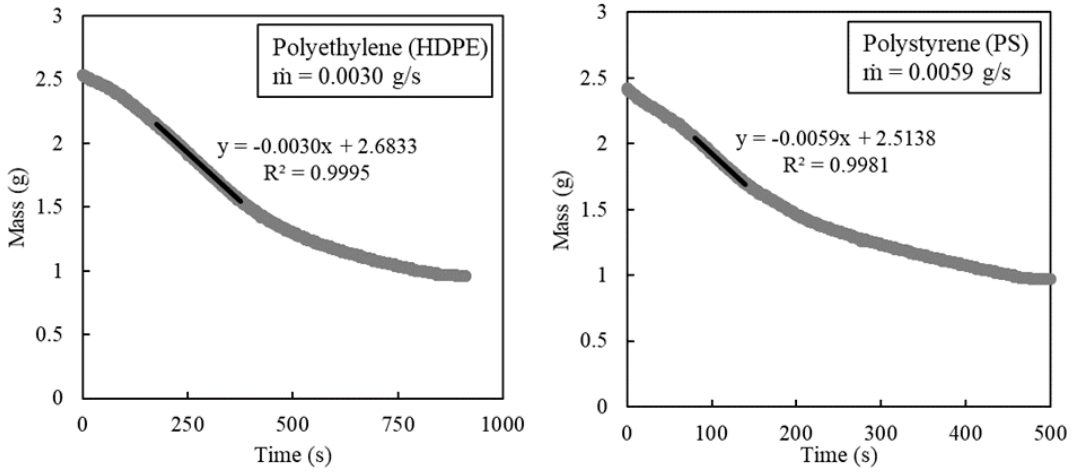

Figure B-3. HDPE (left) and PS (right) mass loss rate curves.

B.2 Matlab script for flame height (based on [26]).

```
clear;
close all;

% Code primarily from Jordan McMahan (Matlab Answers)

% Locates folder that contains images to analyze
myFolder = 'C:\Users\example\Documents\Images';

% Selects which files to analyze
filePattern = fullfile(myFolder, '.jpg');
theFiles = dir(myFolder);

pics = length(theFiles) - 2;
fHsum = 0;

yi = 1300; % Starting y
xi = 0;    % Starting x
w = 425;   % Width of desired output image
h = 2052;  % Distance from burner surface to top of image

% Analyzes each image to determine flame height
for i=3:numel(theFiles)

    baseFileName = theFiles(i).name;
    fullFileName = fullfile(myFolder, baseFileName);
    fprintf(1, 'Now reading %s\n', fullFileName);
    image = imread(fullFileName);
    imageArray = imrotate(image, 270);

    Icrop1 = imcrop(imageArray, [yi xi w h]); % [yi, xi, h, w]
    subplot(2,pics,i-2);
    imshow(Icrop1);
    drawnow;
    grayImage = rgb2gray(imageArray);
    binaryImage = grayImage>170;
% Adjust value to correctly threshold flame (120-200)

    binaryImage = bwareafilt(binaryImage, 1);
    labeledImage = logical(binaryImage);
    props = regionprops(labeledImage, 'BoundingBox');

    flameHeight = h - props.BoundingBox(2) - 0.5;
% pixels. h is y value of burner surface (pixels)
    fH = round(flameHeight*25/218/10, 1);              % cm
(204 = diameter of burner surface in pixels)
    fHsum = fHsum + fH;                                % cm

    Icrop = imcrop(labeledImage, [yi xi w h]);
```

```
    % Boundary detection
    [B,L] = bwboundaries(Icrop, 'noholes');
    subplot(2, pics, pics+i-2);
    imshow(L);
    fHtitle = strcat(num2str(fH), ' cm');
    title(fHtitle);

    hold on
    for j = 1:length(B)
        boundary = B{j};
        plot(boundary(:,2), boundary(:,1), 'r', 'LineWidth',
1)
    end

end

fHavg = round(fHsum/pics, 2);
fHastr = ['Average flame height from ', num2str(pics), '
images = ', num2str(fHavg), ' cm'];
fprintf(1, '%s\n', fHastr);
```

Appendix C: Propane Pool Study Data

This appendix shows the full matrix of considered data for the propane emulation study, presented in Table C-1 - Table C-5. One image from each flame test is chosen as a representative image. This is 1 of the 9 images taken that is closest to the 0.5 intermittency flame height (average height from 9 images) that is reported in Tables C-1 – C-5. These "representative" flame heights ($z_{f,r}$) are compared to the 0.5 intermittency flame height in Table C-6. The images are shown in Figure C-1 – C-19, and each labeled in the format (Series #.Test #), corresponding to Table C-6.

Table C-1. Propane 1st series data (Δh_c = 43.7 kJ/g).

Fuel Properties	$\mathbf{Q_{mix}}$ (SLPM)	$\mathbf{\dot{m}''_{mix}}$ (g/m^2s)	$\mathbf{q''_{cal}}$ (kW/m^2)	$\mathbf{L_{eff}}$ (kJ/g)	$\mathbf{q''_{c}}$ (kW/m^2)	$\mathbf{q''_{o}}$ (kW/m^2)	$\mathbf{T_{cu,max}}$ (°C)	$\mathbf{z_f}$ (mm)	$\mathbf{A_{fl}}$ (m^2)	$\mathbf{q''_{cal,cor}}$ (kW/m^2)
	0.02	1.22	10.69	8.75	13.75	5.18	63.2	11.7	0.000143	36.76
	0.03	1.83	14.65	7.99	10.86	24.25	76.4	17.2	0.000221	32.50
	0.04	2.44	17.13	7.01	9.62	49.68	86.9	21.0	0.000273	30.85
	0.05	3.05	19.01	6.22	8.85	57.79	95.1	28.1	0.000308	30.29
	0.06	3.67	20.20	5.51	8.31	52.18	93.1	32.0	0.000338	29.31
X_f = 1.0	0.07	4.28	21.88	5.12	8.04	43.35	105.9	41.7	0.000368	29.22
$\Delta h_{c,e}$ = 43.7 kJ/g	0.08	4.89	22.16	4.53	7.78	38.46	106.7	46.9	0.000397	27.42
L_{SP} = 202 mm	0.09	5.50	23.26	4.23	7.67	31.20	110.6	53.9	0.000424	26.93
Non-anchored	0.10	6.11	23.53	3.85	7.57	30.23	113.4	67.4	0.000446	25.88
(D_{fl} < 25 mm)	0.11	6.72	23.64	3.52	7.51	25.54	113.2	74.8	0.000462	25.12
	0.12	7.33	23.60	3.22	7.40	24.96	113.0	90.5	0.000471	24.59
	0.13	7.94	23.45	2.95	7.36	22.30	112.8	101	0.000476	24.22
	0.14	8.55	23.40	2.74	7.25	20.38	110.0	112	0.000479	23.97
	0.15	9.16	22.95	2.50	7.18	19.57	110.0	113	0.000486	23.20
	0.16	9.78	22.72	2.32	7.05	18.06	108.9	121	0.000488	22.85
	0.17	10.39	22.39	2.16	6.99	16.86	108.2	127	0.000490	22.46
	0.18	11.00	22.21	2.02	6.88	15.11	109.4	137	0.000491	22.21
	0.20	12.22	21.50	1.76	6.70	15.29	100.2	135	0.000491	21.50
	0.22	13.44	20.84	1.55	6.42	12.90	99.7	143	0.000491	20.84
	0.24	14.66	20.39	1.39	6.06	10.71	98.0	152	0.000491	20.39
	0.26	15.89	19.94	1.26	5.81	9.88	95.4	155	0.000491	19.94
	0.28	17.11	19.52	1.14	5.51	8.19	94.5	156	0.000491	19.52
X_f = 1.0	0.30	18.33	19.04	1.04	5.24	7.41	92.3	167	0.000491	19.04
$\Delta h_{c,e}$ = 43.7 kJ/g	0.32	19.55	18.75	0.96	5.06	6.87	92.6	163	0.000491	18.75
L_{SP} = 202 mm	0.34	20.77	18.50	0.89	4.87	6.32	88.3	164	0.000491	18.50
Anchored	0.36	22.00	18.29	0.83	4.66	6.03	86.1	173	0.000491	18.29
(D_{fl} = 25 mm)	0.38	23.22	17.92	0.77	4.58	5.71	85.6	191	0.000491	17.92
	0.40	24.44	17.48	0.72	4.33	5.18	84.8	186	0.000491	17.48
	0.42	25.66	16.99	0.66	4.22	5.14	91.5	186	0.000491	16.99
	0.44	26.88	16.79	0.62	4.11	4.86	86.9	205	0.000491	16.79
	0.46	28.11	16.62	0.59	4.02	4.73	86.2	196	0.000491	16.62
	0.48	29.33	16.48	0.56	4.00	4.66	86.4	207	0.000491	16.48
	0.50	30.55	16.47	0.54	3.92	4.56	86.2	-	0.000491	16.47

Table C-2. Propane 2nd series data (Δh_c = 37.7 kJ/g).

Fuel Properties	Q_{mix} (SLPM)	$\dot{m}''_{mix}$ (g/m^{2}s)	q''_{cal} (kW/m^2)	L_{eff} (kJ/g)	q''_c (kW/m^2)	q''_o (kW/m^2)	$T_{cu,max}$ (°C)	z_f (mm)	A_{fl} (m^2)	$q''_{cal,cor}$ (kW/m^2)
	0.02	1.13	8.35	7.37	15.95	3.84	56.7	6.0	0.000122	33.69
	0.03	1.70	12.18	7.16	11.89	9.57	69.6	11.0	0.000189	31.67
	0.04	2.27	14.80	6.53	10.39	36.56	81.0	16.2	0.000237	30.67
	0.05	2.83	16.70	5.89	9.46	51.97	88.9	20.7	0.000274	29.96
	0.06	3.40	18.26	5.37	8.69	56.24	92.9	25.9	0.000306	29.32
X_f = 0.8	0.07	3.97	19.23	4.85	8.23	51.64	99.2	32.3	0.000337	28.02
$\Delta h_{c,e}$ = 37.7 kJ/g	0.08	4.53	20.17	4.45	7.90	46.47	102.4	36.4	0.000367	26.97
L_{SP} = 234 mm	0.09	5.10	21.11	4.14	7.57	42.22	104.7	41.4	0.000395	26.21
Non-anchored	0.10	5.67	21.77	3.84	7.51	34.54	112.5	48.6	0.000419	25.48
(D_{fl} < 25 mm)	0.11	6.24	22.50	3.61	7.32	32.15	108.1	58.8	0.000438	25.22
	0.12	6.80	22.78	3.35	7.17	29.08	109.2	66.4	0.000451	24.79
	0.13	7.37	22.79	3.09	7.10	27.17	112.0	73.6	0.000460	24.30
	0.14	7.94	22.58	2.85	7.02	25.31	116.2	83.4	0.000468	23.68
	0.15	8.50	22.63	2.66	6.94	24.47	109.1	93.4	0.000477	23.32
	0.16	9.07	22.45	2.48	6.84	22.81	110.0	101	0.000485	22.71
	0.17	9.64	22.21	2.30	6.73	21.27	108.3	109	0.000490	22.25
	0.18	10.20	21.95	2.15	6.61	19.69	108.9	131	0.000491	21.95
	0.20	11.34	21.30	1.88	6.40	18.89	105.0	137	0.000491	21.30
	0.22	12.47	20.70	1.66	6.10	16.44	104.2	133	0.000491	20.70
	0.24	13.60	20.14	1.48	5.84	14.71	101.5	140	0.000491	20.14
	0.26	14.74	19.58	1.33	5.67	12.85	98.8	148	0.000491	19.58
	0.28	15.87	19.28	1.21	5.40	10.90	97.7	155	0.000491	19.28
	0.30	17.01	18.77	1.10	5.13	9.69	96.1	169	0.000491	18.77
X_f = 0.8	0.32	18.14	18.37	1.01	4.88	8.57	94.7	174	0.000491	18.37
$\Delta h_{c,e}$ = 37.7 kJ/g	0.34	19.27	18.25	0.95	4.79	8.02	89.3	159	0.000491	18.25
L_{SP} = 234 mm	0.36	20.41	17.67	0.87	4.55	6.97	89.4	165	0.000491	17.67
Anchored	0.38	21.54	17.31	0.80	4.39	6.47	91.1	174	0.000491	17.31
(D_{fl} = 25 mm)	0.40	22.67	17.16	0.76	4.26	5.90	88.2	179	0.000491	17.16
	0.42	23.81	16.87	0.71	4.17	5.54	87.5	176	0.000491	16.87
	0.44	24.94	17.02	0.68	4.13	5.41	82.8	185	0.000491	17.02
	0.46	26.08	16.59	0.64	4.04	5.26	82.4	187	0.000491	16.59
	0.48	27.21	16.59	0.61	4.02	5.14	83.1	188	0.000491	16.59
	0.50	28.34	16.54	0.58	3.98	4.96	81.7	198	0.000491	16.54
	0.52	29.48	16.35	0.55	3.95	4.92	81.8	187	0.000491	16.35
	0.54	30.61	16.31	0.53	3.90	4.83	81.6	202	0.000491	16.31

Table C-3. Propane 3rd series data (Δh_c = 30.7 kJ/g).

Fuel Properties	Q_{mix} (SLPM)	$\dot{m}''_{mix}$ (g/m^{2}s)	q''_{cal} (kW/m^2)	L_{eff} (kJ/g)	q''_c (kW/m^2)	q''_o (kW/m^2)	$T_{cu,max}$ (°C)	z_f (mm)	A_{fl} (m^2)	$q''_{cal,cor}$ (kW/m^2)
X_f = 0.6 $\Delta h_{c,e}$ = 30.7 kJ/g L_{SP} = 288 mm Non-anchored (D_{fl} < 25 mm)	0.03	1.57	9.54	6.08	13.86	4.55	58.7	8.2	0.000146	32.09
	0.04	2.09	11.82	5.65	11.73	9.42	66.7	10.6	0.000184	31.51
	0.05	2.61	13.92	5.33	10.25	29.23	78.2	14.8	0.000220	31.08
	0.06	3.14	15.71	5.01	9.34	41.62	81.6	17.2	0.000253	30.50
	0.07	3.66	16.37	4.47	8.67	52.89	83.3	20.6	0.000284	28.34
	0.08	4.18	17.60	4.21	8.23	54.78	89.8	25.0	0.000312	27.69
	0.09	4.70	18.51	3.93	7.85	52.98	91.7	29.7	0.000339	26.83
	0.10	5.23	18.88	3.61	7.65	51.95	94.9	31.7	0.000364	25.47
	0.11	5.75	20.11	3.50	7.31	42.85	97.7	37.9	0.000388	25.46
	0.12	6.27	20.36	3.25	7.08	40.79	96.8	41.6	0.000410	24.37
	0.13	6.80	20.96	3.08	6.92	37.17	98.9	47.1	0.000431	23.87
	0.14	7.32	21.21	2.90	6.78	36.03	103.6	52.1	0.000450	23.16
	0.15	7.84	21.01	2.68	6.57	32.44	99.8	57.2	0.000465	22.19
	0.16	8.36	21.15	2.53	6.49	28.67	102.7	65.4	0.000476	21.83
	0.17	8.89	21.07	2.37	6.35	26.84	102.7	71.9	0.000481	21.50
	0.18	9.41	20.89	2.22	6.22	25.30	101.3	78.9	0.000487	21.06
X_f = 0.6 $\Delta h_{c,e}$ = 30.7 kJ/g L_{SP} = 288 mm Anchored (D_{fl} = 25 mm)	0.20	10.45	20.56	1.97	5.98	22.77	101.6	94.1	0.000491	20.56
	0.22	11.50	20.24	1.76	5.74	20.91	100.4	106	0.000491	20.24
	0.24	12.55	19.77	1.58	5.52	18.77	99.1	115	0.000491	19.77
	0.26	13.59	19.34	1.42	5.31	16.70	99.9	122	0.000491	19.34
	0.28	14.64	18.91	1.29	5.08	15.28	94.6	129	0.000491	18.91
	0.30	15.68	18.49	1.18	4.92	14.35	93.4	144	0.000491	18.49
	0.32	16.73	18.29	1.09	4.88	13.36	84.8	132	0.000491	18.29
	0.34	17.77	17.88	1.01	4.63	11.27	83.7	139	0.000491	17.88
	0.36	18.82	17.39	0.92	4.45	10.13	86.7	151	0.000491	17.39
	0.38	19.86	17.10	0.86	4.30	9.15	86.4	143	0.000491	17.10
	0.40	20.91	16.76	0.80	4.15	8.69	85.3	146	0.000491	16.76
	0.42	21.96	16.48	0.75	4.04	7.76	83.9	150	0.000491	16.48
	0.44	23.00	16.26	0.71	3.93	7.20	82.9	159	0.000491	16.26
	0.46	24.05	15.97	0.66	3.86	6.71	82.3	170	0.000491	15.97
	0.48	25.09	16.11	0.64	3.86	6.39	78.8	165	0.000491	16.11
	0.50	26.14	15.73	0.60	3.77	6.02	78.2	174	0.000491	15.73
	0.52	27.18	15.37	0.57	3.67	5.66	79.1	162	0.000491	15.37
	0.54	28.23	15.44	0.55	3.70	5.52	77.2	172	0.000491	15.44
	0.56	29.27	15.24	0.52	3.66	5.45	76.2	181	0.000491	15.24
	0.58	30.32	15.09	0.50	3.61	5.12	75.8	178	0.000491	15.09

Table C-4. Propane 4th series data (Δh_c = 22.4 kJ/g).

Fuel Properties	Q_{mix} (SLPM)	$\dot{m}''_{mix}$ (g/m^{2}s)	q''_{cal} (kW/m^2)	L_{eff} (kJ/g)	q''_c (kW/m^2)	q''_o (kW/m^2)	$T_{cu,max}$ (°C)	z_f (mm)	A_{fl} (m^2)	$q''_{cal,cor}$ (kW/m^2)
X_f = 0.4 $\Delta h_{c,e}$ = 22.4 kJ/g L_{SP} = 395 mm Non-anchored (D_{fl} < 25 mm)	0.04	1.91	7.84	4.10	15.34	3.45	53.7	8.0	-	-
	0.05	2.39	9.69	4.05	12.61	7.71	61.8	10.9	-	-
	0.06	2.87	11.27	3.92	11.01	11.68	67.1	12.8	-	-
	0.07	3.35	12.33	3.68	10.11	25.06	71.6	15.4	-	-
	0.08	3.83	13.83	3.61	9.51	38.48	76.0	16.4	-	-
	0.09	4.31	15.01	3.48	8.86	45.43	80.4	18.3	-	-
	0.10	4.79	15.90	3.32	8.39	50.94	83.8	20.6	-	-
	0.11	5.26	16.56	3.15	7.97	51.72	88.4	23.4	-	-
	0.12	5.74	17.02	2.96	7.59	49.99	87.3	25.3	-	-
	0.13	6.22	17.61	2.83	7.25	49.59	85.1	28.0	-	-
	0.14	6.70	18.05	2.69	7.03	38.92	88.5	31.6	-	-
	0.15	7.18	18.35	2.56	6.80	38.93	95.2	33.9	-	-
	0.16	7.66	18.62	2.43	6.54	37.84	91.2	36.8	-	-
	0.17	8.14	18.86	2.32	6.43	36.66	94.5	38.2	-	-
	0.18	8.62	18.94	2.20	6.27	34.35	96.6	42.3	-	-
	0.20	9.57	19.24	2.01	5.95	30.93	95.4	46.7	-	-
	0.22	10.53	19.28	1.83	5.67	28.34	94.3	60.8	-	-
	0.24	11.49	18.94	1.65	5.40	25.93	91.7	76.0	-	-
	0.26	12.44	18.88	1.52	5.18	24.01	92.4	85.1	-	-
	0.28	13.40	18.48	1.38	4.97	22.07	92.6	113	-	-
X_f = 0.4 $\Delta h_{c,e}$ = 22.4 kJ/g L_{SP} = 395 mm Anchored (D_{fl} = 25 mm)	0.30	14.36	18.01	1.25	4.76	20.43	90.9	114	0.000491	18.01
	0.32	15.32	17.63	1.15	4.55	18.82	89.7	112	0.000491	17.63
	0.34	16.27	17.27	1.06	4.39	17.33	85.7	127	0.000491	17.27
	0.36	17.23	16.90	0.98	4.25	16.24	84.4	129	0.000491	16.90
	0.38	18.19	16.68	0.92	4.17	15.27	81.5	125	0.000491	16.68
	0.40	19.14	16.15	0.84	4.00	14.00	80.7	126	0.000491	16.15
	0.42	20.10	15.86	0.79	3.91	12.99	87.3	135	0.000491	15.86
	0.44	21.06	15.48	0.74	3.75	11.99	79.6	142	0.000491	15.48
	0.46	22.02	15.29	0.69	3.65	11.28	79.5	142	0.000491	15.29
	0.48	22.97	15.02	0.65	3.57	10.39	77.1	138	0.000491	15.02
	0.50	23.93	14.66	0.61	3.47	9.75	76.0	146	0.000491	14.66
	0.52	24.89	14.68	0.59	3.45	9.21	74.6	140	0.000491	14.68
	0.54	25.85	14.45	0.56	3.41	8.97	73.5	138	0.000491	14.45
	0.56	26.80	14.18	0.53	3.33	8.20	73.5	143	0.000491	14.18
	0.58	27.76	13.90	0.50	3.28	7.67	70.5	153	0.000491	13.90
	0.60	28.72	13.79	0.48	3.23	7.16	69.3	153	0.000491	13.79
	0.62	29.67	13.52	0.46	3.19	6.76	70.5	160	0.000491	13.52
	0.64	30.63	13.33	0.44	3.15	6.40	70.2	166	0.000491	13.33

Table C-5. Propane 5th series data (Δh_c = 12.3 kJ/g).

Fuel Properties	Q_{mix} (SLPM)	$\dot{m}''_{mix}$ (g/m^{2}s)	q''_{cal} (kW/m^2)	L_{eff} (kJ/g)	q''_c (kW/m^2)	q''_o (kW/m^2)	$T_{cu,max}$ (°C)	z_f (mm)	A_{fl} (m^2)	$q''_{cal,cor}$ (kW/m^2)
X_f = 0.2 $\Delta h_{c,e}$ = 12.3 kJ/g L_{SP} = 716 mm Non-anchored (D_{fl} < 25 mm)	0.46	19.99	11.25	0.56	3.16	20.27	61.2	-	0.000491	11.25
	0.48	20.86	11.05	0.53	3.03	19.02	61.9	-	0.000491	11.05
	0.50	21.72	10.64	0.49	2.91	17.93	61.5	-	0.000491	10.64
	0.52	22.59	10.38	0.46	2.82	16.85	60.2	-	0.000491	10.38
	0.54	23.46	10.12	0.43	2.73	15.97	59.5	-	0.000491	10.12
	0.56	24.33	9.77	0.40	2.65	15.11	56.9	-	0.000491	9.77
	0.58	25.20	9.53	0.38	2.59	14.28	56.3	-	0.000491	9.53
	0.60	26.07	9.30	0.36	2.53	13.43	56.0	-	0.000491	9.30
	0.62	26.94	8.86	0.33	2.50	12.44	51.5	-	0.000491	8.86
	0.64	27.81	8.55	0.31	2.42	12.00	51.8	-	0.000491	8.55
	0.66	28.68	8.34	0.29	2.39	11.28	52.7	-	0.000491	8.34
	0.68	29.55	8.25	0.28	2.35	10.78	51.6	-	0.000491	8.25
	0.70	30.41	7.89	0.26	2.29	10.10	50.7	-	0.000491	7.89

Table C-6. Average flame heights & representative images for the first four series.

Series	1			2			3			4		
Δh_c	43.7 kJ/g			37.7 kJ/g			30.7 kJ/g			22.4 kJ/g		
Test No.	$\dot{m}''_{mix}$	z_f	$z_{f,r}$	$\dot{m}''_{mix}$	z_f	$z_{f,r}$	$\dot{m}''_{mix}$	z_f	$z_{f,r}$	$\dot{m}''_{mix}$	z_f	$z_{f,r}$
-	(g/m^2s)	(mm)	(mm)	(g/m^2s)	(mm)	(mm)	(g/m^2s)	(mm)	(mm)	(g/m^2s)	(mm)	(mm)
1	1.22	12	12	1.13	6	6	1.57	8	8	1.91	8	8
2	1.83	17	17	1.70	11	11	2.09	11	11	2.39	11	11
3	2.44	21	21	2.27	16	16	2.61	15	15	2.87	13	13
4	3.05	28	28	2.83	21	21	3.14	17	17	3.35	15	15
5	3.67	32	32	3.40	26	26	3.66	21	21	3.83	16	16
6	4.28	42	42	3.97	32	32	4.18	25	25	4.31	18	18
7	4.89	47	47	4.53	36	36	4.70	30	30	4.79	21	21
8	5.50	54	54	5.10	41	41	5.23	32	32	5.26	23	23
9	6.11	67	68	5.67	49	48	5.75	38	38	5.74	25	25
10	6.72	75	75	6.24	59	60	6.27	42	41	6.22	28	28
11	7.33	91	91	6.80	66	67	6.80	47	48	6.70	32	32
12	7.94	101	100	7.37	74	73	7.32	52	52	7.18	34	34
13	8.55	112	112	7.94	83	84	7.84	57	57	7.66	37	47
14	9.16	113	116	8.50	93	92	8.36	65	64	8.14	38	48
15	9.78	121	121	9.07	101	101	8.89	72	72	8.62	42	42
16	10.39	127	125	9.64	109	108	9.41	79	78	9.57	47	48
17	11.00	137	136	10.20	131	132	10.45	94	94	10.53	61	61
18	12.22	135	134	11.34	137	135	11.50	106	106	11.49	76	75
19	13.44	143	144	12.47	133	129	12.55	115	116	12.44	85	85
20	14.66	152	152	13.60	140	143	13.59	122	122	13.40	113	113
21	15.89	155	156	14.74	148	150	14.64	129	128	14.36	114	114
22	17.11	156	155	15.87	155	154	15.68	144	143	15.32	112	112
23	18.33	167	169	17.01	169	167	16.73	132	132	16.27	127	129
24	19.55	163	164	18.14	174	173	17.77	139	140	17.23	129	128
25	20.77	164	166	19.27	159	160	18.82	151	150	18.19	125	125
26	22.00	173	171	20.41	165	167	19.86	143	145	19.14	126	128
27	23.22	191	191	21.54	174	173	20.91	146	144	20.10	135	136
28	24.44	186	186	22.67	179	179	21.96	150	147	21.06	142	140
29	25.66	186	187	23.81	176	176	23.00	159	157	22.02	142	141
30	26.88	205	201	24.94	185	186	24.05	170	167	22.97	138	138
31	28.11	196	198	26.08	187	188	25.09	165	167	23.93	146	146
32	29.33	207	207	27.21	188	188	26.14	174	178	24.89	140	141
33	30.55	-	-	28.34	198	197	27.18	162	163	25.85	138	136
34	-	-	-	29.48	187	188	28.23	172	171	26.80	143	145
35	-	-	-	30.61	202	200	29.27	181	181	27.76	153	155
36	-	-	-	-	-	-	30.32	178	180	28.72	153	152
37	-	-	-	-	-	-	-	-	-	29.67	160	163
38	-	-	-	-	-	-	-	-	-	30.63	166	166

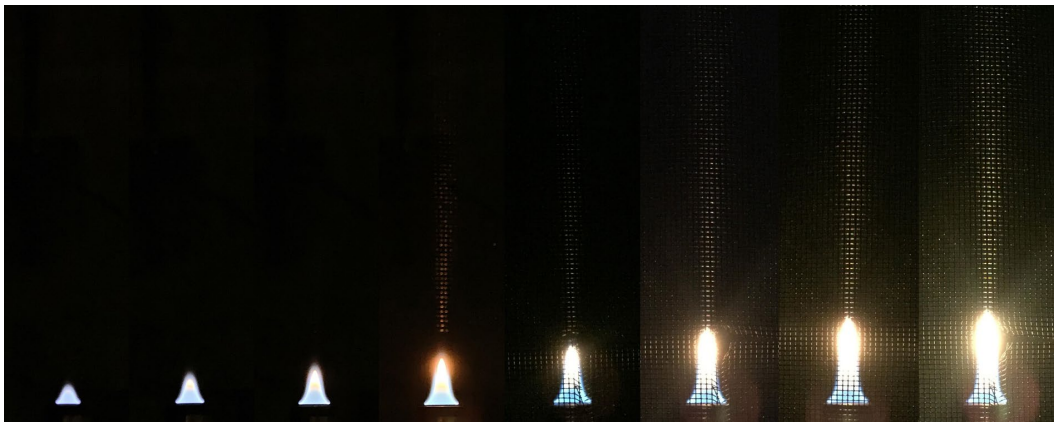

Figure C-1. Series 1 (Δh_c = 43.7 kJ/g) representative flames, tests 1.1-1.8.

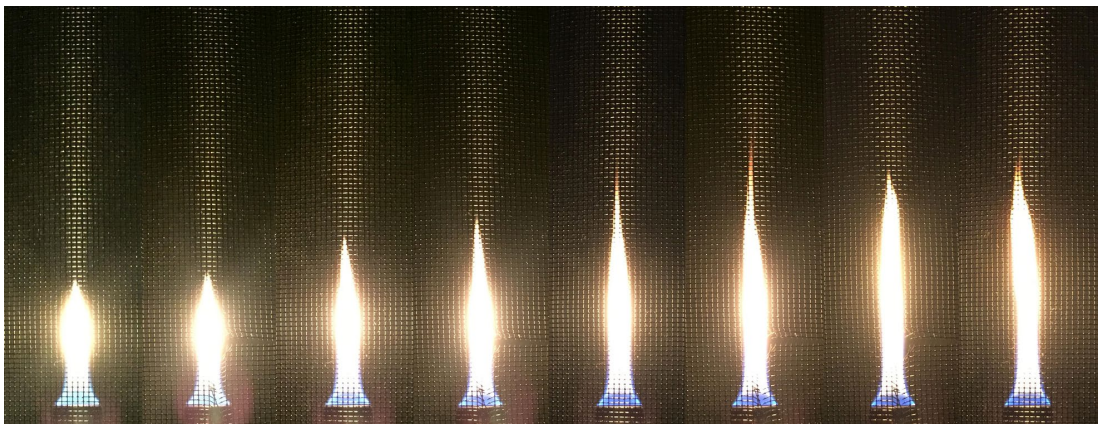

Figure C-2. Series 1 (Δh_c = 43.7 kJ/g) representative flames, tests 1.9-1.16.

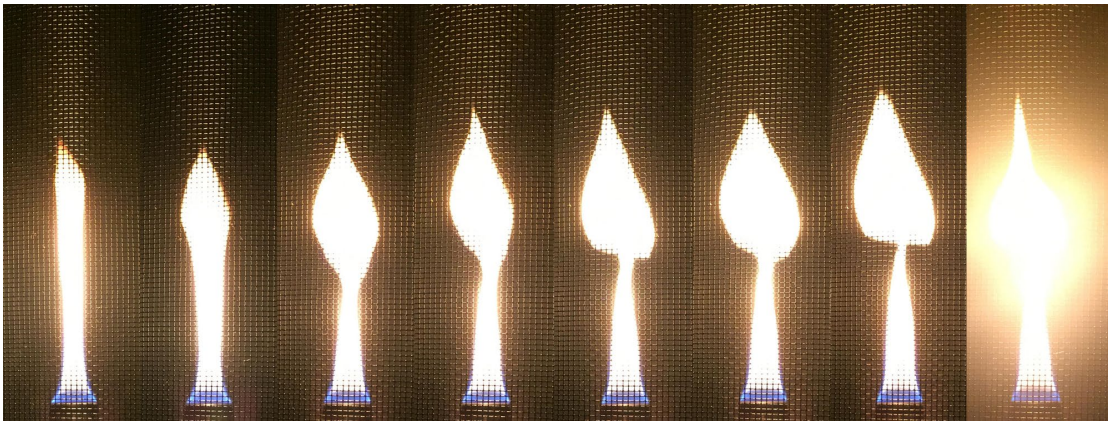

Figure C-3. Series 1 (Δh_c = 43.7 kJ/g) representative flames, tests 1.17-1.24.

Figure C-4. Series 1 (Δh_c = 43.7 kJ/g) representative flames, tests 1.25-1.32.

Figure C-5. Series 2 (Δh_c =37.7 kJ/g) representative flames, tests 2.1-2.7.

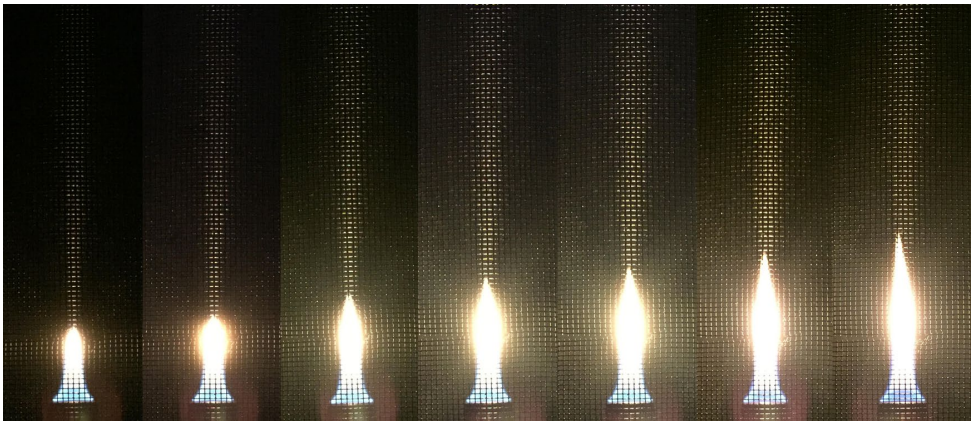

Figure C-6. Series 2 (Δh_c =37.7 kJ/g) representative flames, tests 2.8-2.14.

Figure C-7. Series 2 (Δh_c =37.7 kJ/g) representative flames, tests 2.15-2.21.

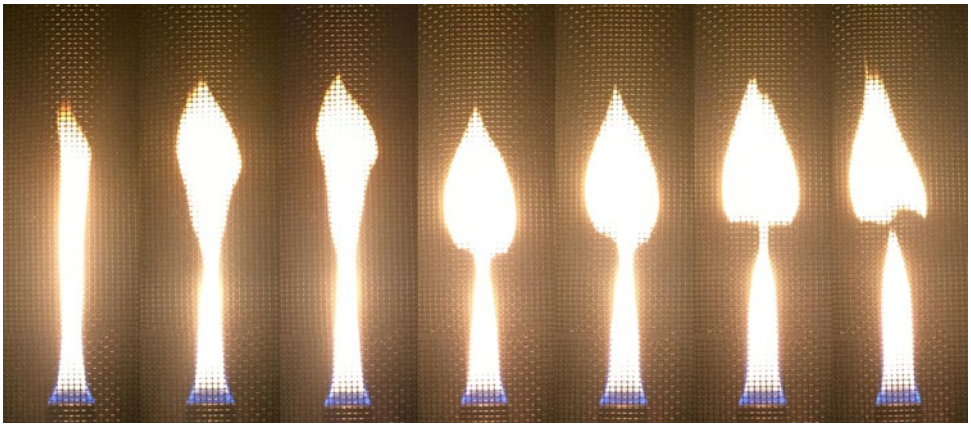

Figure C-8. Series 2 (Δh_c =37.7 kJ/g) representative flames, tests 2.22-2.28.

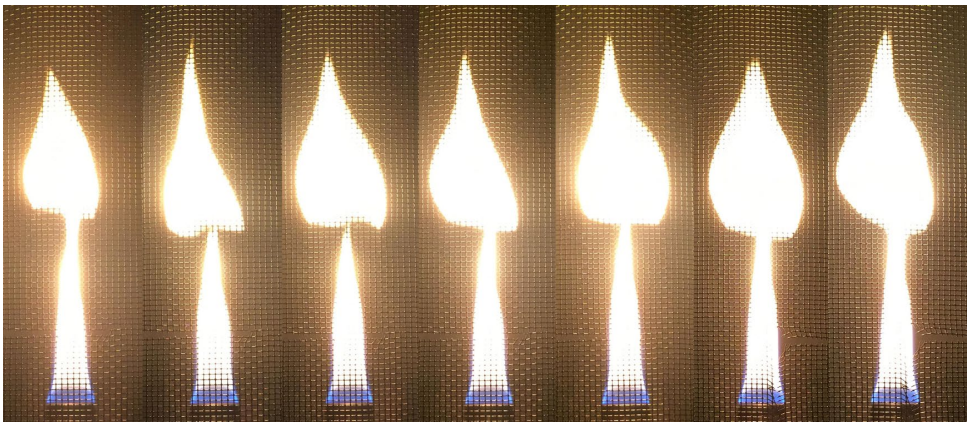

Figure C-9. Series 2 (Δh_c =37.7 kJ/g) representative flames, tests 2.29-2.35.

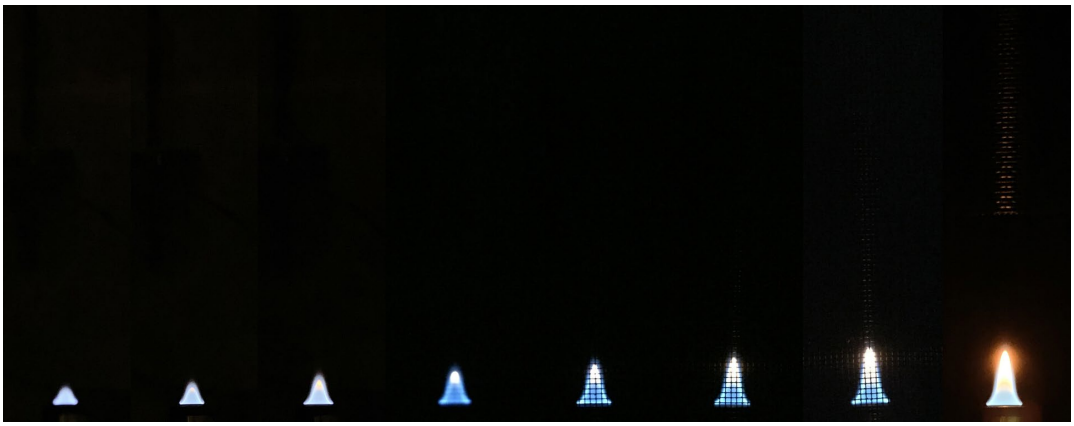

Figure C-10. Series 3 (Δh_c =30.7 kJ/g) representative flames, tests 3.1-3.8.

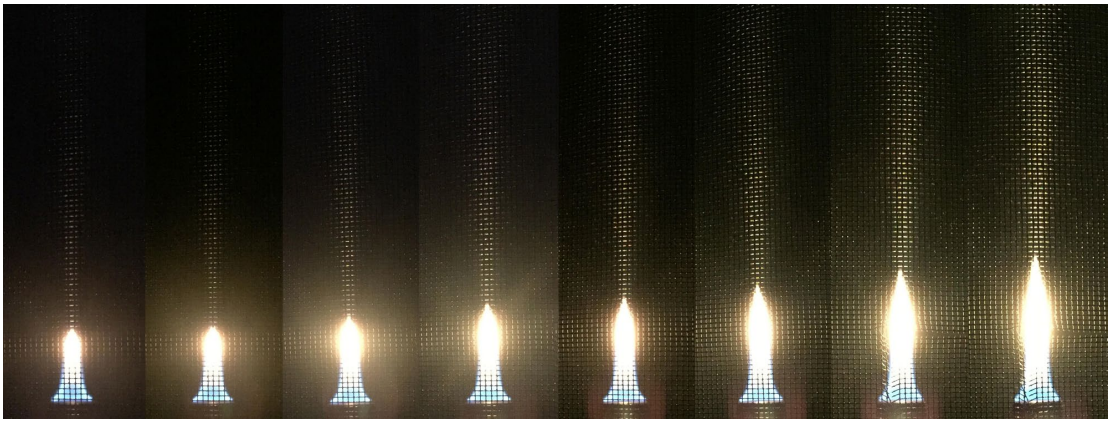

Figure C-11. Series 3 (Δh_c =30.7 kJ/g) representative flames, tests 3.9-3.16.

Figure C-12. Series 3 (Δh_c =30.7 kJ/g) representative flames, tests 3.17-3.24.

Figure C-13. Series 3 (Δh_c =30.7 kJ/g) representative flames, tests 3.25-3.32.

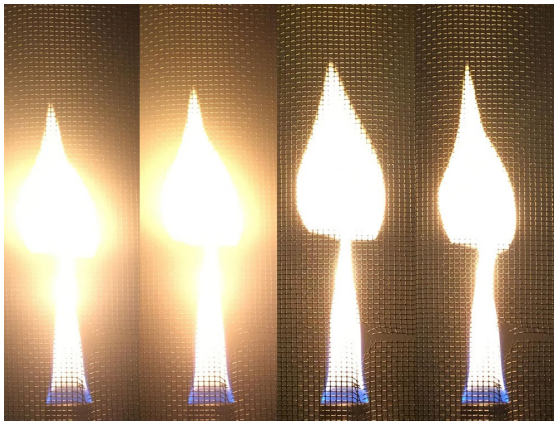

Figure C-14. Series 3 (Δh_c =30.7 kJ/g) representative flames, tests 3.33-3.36.

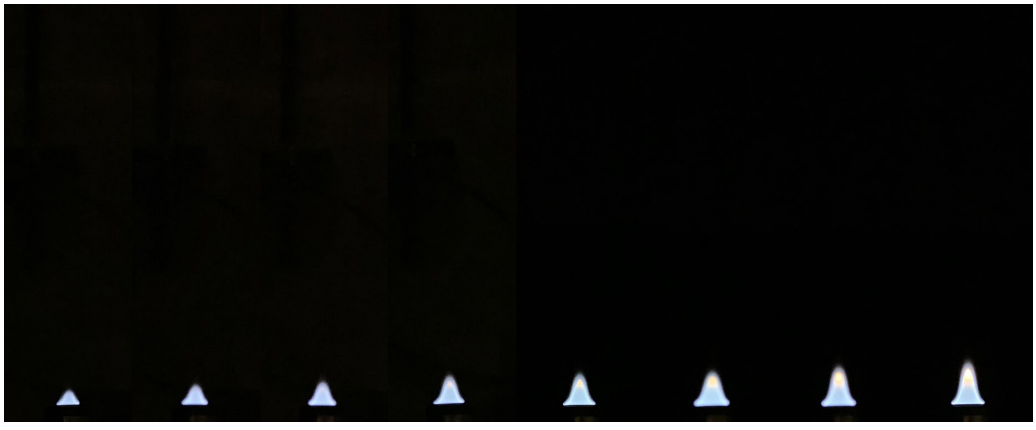

Figure C-15. Series 4 (Δh_c =22.4 kJ/g) representative flames, tests 4.1-4.8.

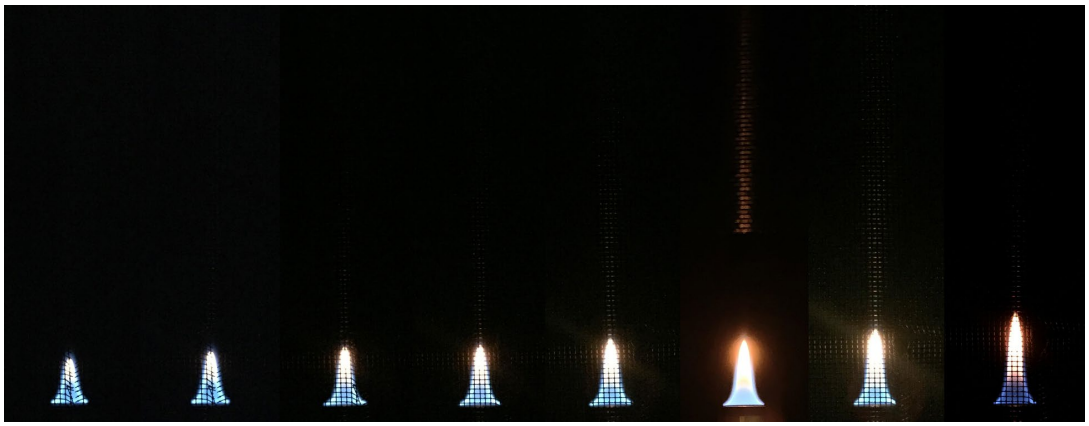

Figure C-16. Series 4 (Δh_c =22.4 kJ/g) representative flames, tests 4.9-4.16.

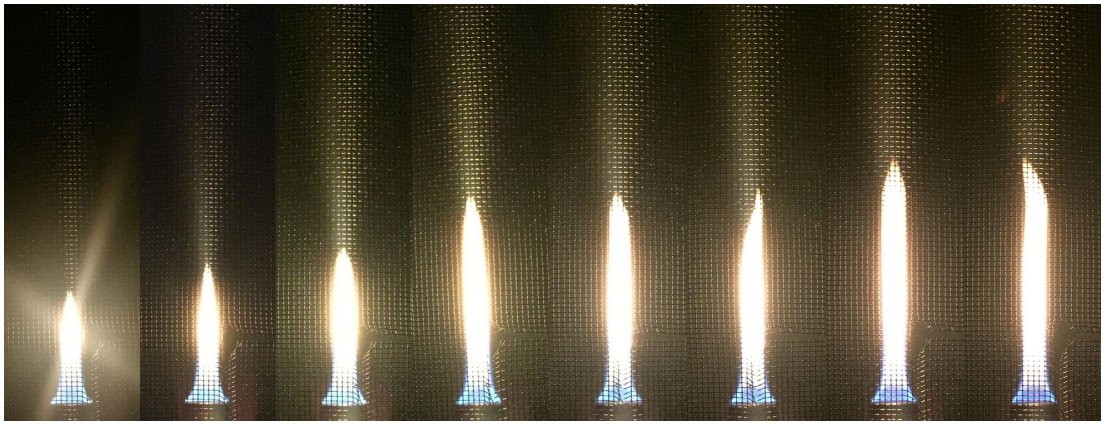

Figure C-17. Series 4 (Δh_c =22.4 kJ/g) representative flames, tests 4.17-4.24.

Figure C-18. Series 4 (Δh_c =22.4 kJ/g) representative flames, tests 4.25-4.32.

Figure C-19. Series 4 (Δh_c =22.4 kJ/g) representative flames, tests 4.33-4.38.

Bibliography

[1] B. Burrough, Dragonfly: NASA and the Crisis Aboard Mir, New York: HarperCollins, 1998.

[2] H. D. Ross, Microgravity Combustion: Fire in Free Fall, London, UK: Academic Press, 2001.

[3] NASA, "ACME-SRD-001.B Integrated Science Requirements Document (ISRD)," *Advanced combustion via microgravity experiments,* 2013.

[4] NASA, "NASA-STD-6001B, Flammability, offgassing, and compatibility requirements and test procedures," 2016.

[5] A. Markan, "Development and analysis of a burning rate emulator (BRE) for study in microgravity," 2018.

[6] R. C. Corlett, "Heat Transfer Data Summary - Pool Burning Study," *National Science Foundation,* 1965.

[7] R. C. Corlett, "Gas fires with pool-like boundary conditions," *Combustion and Flame,* vol. 12, no. 1, pp. 19-32, 1968.

[8] R. C. Corlett, "Gas fires with pool-like boundary conditions: further results and interpretation," *Combustion and Flame,* vol. 14, pp. 351-360, 1970.

[9] J. de Ris and L. Orloff, "A Dimensionless Correlation of Pool Burning Data," *Combustion and Flame,* vol. 18, pp. 381-388, 1972.

[10] J. L. de Ris and L. Orloff, "The role of buoyancy direction and radiation in turbulent diffusion flames on surfaces," *Symposium (International) on Combustion,* vol. 15, no. 1, pp. 175-182, 1975.

[11] A. Markan, P. B. Sunderland, J. G. Quintiere, J. L. de Ris and H. R. Baum, "Measuring heat flux to a porous burner in microgravity," *Proceedings of the Combustion Institute,* vol. 37, pp. 4137-4144, 2019.

[12] ASTM, "E457-08, Standard test method for measuring heat-transfer rate using a thermal capacitance (Slug) calorimeter," *Annual book of ASTM standards,* vol. 15, 2008.

[13] M. J. Bustamante, "Experimental investigation of liquid and gas fueled flames toward the development of a burning rate emulator (BRE) for microgravity applications," 2012.

[14] Y. Zhang, M. Kim, H. Guo, P. B. Sunderland, J. G. Quintiere, J. de Ris and D. P. Stocker, "Emulation of condensed fuel flames with gases in microgravity," *Combustion and Flame,* vol. 162, pp. 3449-3455, 2015.

[15] Y. Zhang, M. Kim, P. B. Sunderland, J. G. Quintiere and J. de Ris, "A burner to emulate condensed phase fuels," *Experimental Thermal and Fluid Science,* vol. 73, pp. 87-93, 2016.

[16] M. Kim, "Procedures to obtain accurate measurement from a gas fueled burner," 2014.

[17] A. Markan, P. B. Sunderland, J. G. Quintiere, J. L. de Ris, D. P. Stocker and H. R. Baum, "A burning rate emulator (BRE) for study of condensed fuel burning in microgravity," *Combustion and Flame,* vol. 192, pp. 272-282, 2018.

[18] F. V. Lundstrom, P. B. Sunderland, J. G. Quintiere, P. van Hees and J. L. de Ris, "Study of ignition and extinction of small-scale fires in experiments with an emulating gas burner," *Fire Safety Journal,* vol. 87, pp. 18-24, 2017.

[19] F. V. Plathner, J. G. Quintiere and P. van Hees, "Analysis of extinction and sustained ignition," *Fire Safety Journal,* vol. 105, pp. 51-61, 2019.

[20] T. L. Bergman and F. P. Incropera, Fundamentals of Heat and Mass Transfer, Seventh Edition, John Wiley & Sons, 2011.

[21] L. Li and P. B. Sunderland, "Smoke points for fuel-fuel and fuel-intert mixtures," *Fire Safety Journal,* vol. 61, pp. 226-231, 2013.

[22] "Appendix 3," in *SFPE Handbook of Fire Protection Engineering, 5th ed.*, Springer, 2016, pp. 3437-3475.

[23] A. Tewarson, "Generation of Heat and Gaseous, Liquid, and Solid Products in Fires," in *SFPE Handbook of Fire Protection Engineering, 4th ed.*, Quincy, MA, National Fire Protection Association, 2008, pp. 3-109-3-194.

[24] L. Li and P. B. Sunderland, "An improved method of smoke point normalization," *Combust. Sci. Technol.,* vol. 184, pp. 829-841, 2012.

[25] J. G. Quintiere, Fundamentals of Fire Phenomena, John Wiley & Sons, 2006.

[26] J. McMahan and I. Analyst, "Mathworks," Mathworks, 5 June 2017. [Online]. Available: https://www.mathworks.com/matlabcentral/answers/343435-how-can-i-identify-a-flame-in-an-image-and-execute-a-code-that-will-curve-fit-it-so-that-other-tasks.

[27] V. I. Blinov and G. N. Khudyakov, "Diffusion Burning of Liquids," *Izdatel'svo Akademii Nauk SSR, Moscow. English Translation: U.S. Army Engineering Research and Development Laboratories, Information Resources Branch, Translation Analysis Section, Fort Belvoir, VA, No. T-1490a-c,* 1961.

[28] K. Akita and T. Yumoto, "Heat Transfer in Small Pools and Rates of Burning of Liquid Methanol," in *Tenth Symposium (International) on Combustion*, Cambridge, England, The Combustion Institute, 1965, pp. 943-948.

[29] A. Hamins, S. J. Fischer, T. Kashiwagi, M. E. Klassen and J. P. Gore, "Heat Feedback to the Fuel Surface in Pool Fires," *Combustion Science and Technology,* vol. 97, pp. 37-62, 1994.

[30] B. McCaffrey, "Flame Height," in *The SFPE Handbook of Fire Protection Engineering, 1st ed.*, Quincy, MA, National Fire Protection Association, 1988, pp. 1-298-1-305.

[31] F. G. Roper, "The Prediction of Laminar Jet Diffusion Flame Sizes: Part I. Theoretical Model," *Combustion and Flame,* vol. 29, pp. 219-226, 1977.

[32] F. G. Roper, C. Smith and A. C. Cunningham, "The Prediction of Laminar Jet Diffusion Flame Sizes: Part II. Experimental Verification," *Combustion and Flame,* vol. 29, pp. 227-234, 1977.

[33] B. Gebhart, Heat Transfer, 2nd ed., New York: McGraw-Hill Book Co, 1971.

[34] D. Burgess and M. Hertzberg, "Radiation from Pool Flames," in *Heat Transfer in Flames*, New York, John Wiley & Sons, 1974.

[35] H. C. Hottel, "Certain laws governing diffusive burning of liquids," *Fire Research Abstracts Reviews,* vol. 1, pp. 41-44, 1959.